

UC San Diego

UC San Diego Electronic Theses and Dissertations

Title

Hyperbolic phonon polaritons in hexagonal boron nitride

Permalink

<https://escholarship.org/uc/item/3kk8j51p>

Author

Dai, Siyuan

Publication Date

2017

Peer reviewed|Thesis/dissertation

UNIVERSITY OF CALIFORNIA, SAN DIEGO

Hyperbolic Phonon Polaritons in hexagonal boron nitride

A dissertation submitted in partial satisfaction of the
requirements for the degree
Doctor of Philosophy

in

Physics

by

Siyuan Dai

Committee in charge:

Professor Dimitri N. Basov, Chair

Professor Leonid Butov

Professor Shaya Fainman

Professor Michael Fogler

Professor Stojan Radic

2017

Copyright

Siyuan Dai, 2017

All rights reserved.

The Dissertation of Siyuan Dai is approved, and it is acceptable in quality and form for publication on microfilm and electronically:

Chair

University of California, San Diego

2017

DEDICATION

To my parents.

TABLE OF CONTENTS

Signature Page	iii
Dedication	iv
Table of Contents	v
List of Figures	viii
Acknowledgements.....	ix
Vita.....	xii
Abstract of the Dissertation.....	xiv
Chapter 1 Introduction	1
Chapter 2 Infrared nano-imaging of phonon polaritons in hexagonal boron nitride ...	6
2.1 Abstract	6
2.2 Introduction	6
2.3 Experimental details	7
2.4 Experimental data	8
2.5 Conclusion and Outlook	12
2.6 Supplementary information	13
2.6.1 Preparation and characterization of hBN crystals	13
2.6.2 Infrared nano-imaging and nano-FTIR	14
2.6.3 Modeling of tip-launched phonon polariton waves	14
2.6.4 Near-field imaging of phonon polaritons	15
2.6.5 Optical constants and infrared reflectivity of hBN	17
2.6.6 The origin of multiple polariton branches	19
2.6.7 Nano-FTIR spectra simulation	21
2.7 Acknowledgements	23
2.8 Bibliography	32
Chapter 3 Natural hyperbolic response in hexagonal boron nitride and subdiffractional focusing	37
3.1 Abstract	37
3.2 Introduction	38

3.3	Experimental setup	41
3.4	Experimental results	42
3.4.1	Subdiffractional focusing and imaging through hBN	42
3.4.2	Real-space imaging of multiple guided polaritons in hBN	46
3.5	Discussion	49
3.6	Methods	50
3.6.1	Experimental setup	50
3.6.2	Sample fabrication	51
3.7	Supplementary information	51
3.7.1	Theoretical model for focusing by a slab of a hyperbolic material	51
3.7.2	Guided wave dispersion and its thickness dependence	62
3.8	Acknowledgements	64
3.9	Bibliography	75
Chapter 4	Tunable hyperbolic metamaterial from graphene/hBN heterostructure	83
4.1	Abstract	83
4.2	Introduction	84
4.3	Experimental results	85
4.4	Conclusion and Outlook	90
4.5	Methods	91
4.5.1	Experimental setup	92
4.5.2	Sample fabrication	92
4.6	Supplementary information	93
4.6.1	Response function and eigenmode dispersion	93
4.6.2	Tunable polaritons and Type I plasmon-phonon coupling	99
4.6.3	Higher order hyperbolic polaritons in graphene/hBN.....	101
4.7	Acknowledgements	102
4.8	Bibliography	109
Chapter 5	Emitter and emission efficiency of phonon polaritons in hBN.....	113
5.1	Abstract	113
5.2	Introduction	114
5.3	Experimental results	115
5.3.1	Various polariton emitters	115
5.3.2	Relative polariton emission efficiency	118
5.4	Conclusion and Outlook	121
5.5	Methods	121
5.5.1	Experimental setup	121
5.5.2	Sample fabrication	122

5.5.3	Simulation of edge-emitted hyperbolic phonon polaritons ..	122
5.6	Supplementary Information	124
5.6.1	Orientation-dependent nano-imaging data	124
5.5.2	Polariton fringe periods in hBN and in graphene	125
5.7	Acknowledgements	127
5.8	Bibliography	133

LIST OF FIGURES

Figure 2.1: Real-space imaging of phonon polaritons on hBN.....	24
Figure 2.2: The phonon polariton dispersion and nano-FTIR spectra.....	25
Figure 2.3: The evolution of phonon polariton with the thickness of hBN crystals.....	26
Figure 2.4: Optical microscope image and Raman spectrum of hBN.....	27
Figure 2.5: Schematics of the UCSD s-SNOM experiments.....	28
Figure 2.6: Polaritonic waves in tapered crystals.....	29
Figure 2.7: Near-field image and simulation results with different loss factors.....	30
Figure 2.8: Layered structure for the Air-SiO ₂ system of the dispersion model.....	31
Figure 3.1: Hyperbolic dispersion of hBN.....	65
Figure 3.2: Sub-diffractive focusing and imaging through an hBN crystal.....	66
Figure 3.3: The image formation.....	67
Figure 3.4: Polariton frequency (ω) – in-plane momentum (k_t) dispersion for hBN...	68
Figure 3.5: Imaging of polariton waveguide modes near the hBN edges.....	69
Figure 3.6: Theoretical model and the electric field profile it predicts.....	70
Figure 3.7: Thickness dependence of the guided wave dispersion.....	71
Figure 3.8: Nano-FTIR study of guided waves in the lower stop-band.....	72
Figure 3.9: Estimates of the loss factor.....	73
Figure 3.10: Supplementary s-SNOM images.....	74
Figure 4.1: An overview of hyperbolic response in graphene/hBN metastructure.....	103
Figure 4.2: Modification of type II HP ² s in graphene/hBN metastructure.....	104
Figure 4.3: Tuning the hybrid polariton by gating and varying the thickness.....	105
Figure 4.4: Dispersion of polaritons in graphene/h-BN with different thickness.....	106
Figure 4.5: Tunable hyperbolic and hybrid polaritons in lower frequency.....	107
Figure 4.6: Supplementary s-SNOM data for hybridized $l \neq 0$ polaritons.....	108
Figure 5.1: Polaritons emitted by the s-SNOM and hBN edges.....	128
Figure 5.2: Polariton emission efficiency.....	129
Table 5.1: Relative scattering parameters for three types of emitters.....	130
Figure 5.3: s-SNOM image of hBN crystal with impurities and protrusion.....	131
Figure 5.4: Polaritons in hBN disks.....	132

ACKNOWLEDGEMENTS

First and foremost, I would like thank my advisor Prof. Dimitri Basov, who is not only a top scientist but also an excellent educator and a great person. I owe an immense debt of gratitude to him for his advice, support, encouragement and patience in the last six years. It is my great pleasure and honor to work with Dimitri who has extremely strong expertise, broad vision and deep insights and has been always supportive and caring for both my scientific career and personal life.

I would like to thank Prof. Michael Fogler who has been collaborating with us and provided instructive advices to all my research projects.

Thank my other committee members, Prof. Leonid Butov, Prof. Shaya Fainman and Prof. Stojan Radic, for their time and effort in improving my PhD research and dissertation.

I am also grateful to all my past and current labmates in the Basov group and all the members in our weekly near-field meeting together with the Fogler group. Special thanks go to my collaborators, especially Prof. Pablo Jarillo-Herrero, Qiong Ma, Trond Andersen and Yafang Yang at MIT, for their support and help in my research projects. I would like to thank Dr. Fritz Keilmann and Prof. Mark Thiemens for their support in our nano-optic apparatus to make our experimental observations happen.

Last but not least, I would like to thank all the nice staff in the physics department, especially Sharmila Poddar, Catherine Mcconney and Hilary Ford for their all-aspect support.

Chapter 2, in full, is a reprint of the material as it appears in S. Dai, Z. Fei, Q. Ma, A. S. Rodin, M. Wagner, A. S. McLeod, M. K. Liu, W. Gannett, W. Regan, K. Watanabe, T. Taniguchi, M. Thiemens, G. Dominguez, A. H. Castro-Neto, A. Zettl, F. Keilmann, P. Jarillo-Herrero, M. M. Fogler & D. N. Basov. "Tunable Phonon Polaritons in Atomically Thin van der Waals Crystals of Boron Nitride". *Science* 343, 1125-1129 (2014). The dissertation author was the primary investigator and author of this paper.

Chapter 3, in full, is a reprint of the material as it appears in S. Dai, Q. Ma, T. Andersen, A. S. McLeod, Z. Fei, M. K. Liu, M. Wagner, K. Watanabe, T. Taniguchi, M. Thiemens, F. Keilmann, P. Jarillo-Herrero, M. M. Fogler & D. N. Basov. "Subdiffractional focusing and guiding of polaritonic rays in a natural hyperbolic material". *Nature Comm.* 6, 6963 (2015). The dissertation author was the primary investigator and author of this paper.

Chapter 4, in full, is a reprint of the material as it appears in S. Dai, Q. Ma, M. K. Liu, T. Andersen, Z. Fei, M. D. Goldflam, M. Wagner, K. Watanabe, T. Taniguchi, M. Thiemens, F. Keilmann, G. C. A. M. Janssen, S-E. Zhu, P. Jarillo-Herrero, M. M. Fogler & D. N. Basov. "Graphene on hexagonal boron nitride as a tunable hyperbolic

metamaterial”. *Nature Nanotech.* 10, 682-686 (2015). The dissertation author was the primary investigator and author of this paper.

Chapter 5, in full, is a reprint of the material as it appears in S. Dai, Q. Ma, Y. Yang, J. Rosenfeld, M. D. Goldflam, A. McLeod, Z. Sun, T. I. Andersen, Z. Fei, M. K. Liu, Y. Shao, K. Watanabe, T. Taniguchi, M. Thiemens, F. Keilmann, P. Jarillo-Herrero, M. M. Fogler & D. N. Basov. “Emission and emission efficiency of hyperbolic phonon polariton in hexagonal boron nitride”. To be submitted (2017). The dissertation author was the primary investigator and author of this paper.

VITA

2011	B.S. in Physics, University of Science and Technology of China
2011-2017	Graduate Student Researcher, University of California, San Diego
2014	M.S. in Physics, University of California, San Diego
2017	Ph.D. in Physics, University of California, San Diego

PUBLICATIONS

S. Dai, Q. Ma, Y. Yang, J. Rosenfeld, M. D. Goldflam, A. McLeod, Z. Sun, T. I. Andersen, Z. Fei, M. K. Liu, Y. Shao, K. Watanabe, T. Taniguchi, M. Thiemens, F. Keilmann, P. Jarillo-Herrero, M. M. Fogler & D. N. Basov. “Relative efficiency of polariton emission in two-dimensional materials”. *arXiv*. 1704.05618 (2017).

Y. Shao, K. W. Post, J. Wu, S. Dai, A. J. Frenzel, A. R. Richardella, J. Lee, N. Samarth, M. M. Fogler, A. V. Balatsky, D. Kharzeev, D. N. Basov. “Faraday rotation due to surface states in the topological insulator $(\text{Bi}_{1-x}\text{Sb}_x)_2\text{Te}_3$ ”. *Nano Lett.* 17(2), 980-984 (2017).

Z. Fei, J. Foley, W. Gannett, M. Liu, S. Dai, G. Ni, A. Zettl, M. M. Fogler, G. Wiederrecht, S. K. Gray, D. N. Basov. “Ultraconfined Plasmonic Hotspots Inside Graphene Nanobubbles”. *Nano Lett.* 16(12), 7842-7848 (2016).

A. J. Giles, S. Dai, O. J. Glembocki, A. V. Kretinin, Z. Sun, C. T. Ellis, J. G. Tischler, T. Taniguchi, K. Watanabe, M. M. Fogler, K. S. Novoselov, D. N. Basov & J. D. Caldwell. “Imaging of anomalous internal reflections of hyperbolic phonon-polaritons in hexagonal boron nitride”. *Nano Lett.* 16(6), 3858 (2016).

Z. Fei, M. Goldflam, J. Wu, S. Dai, M. Wagner, A. McLeod, M. K. Liu, S-E. Zhu, G. C. A. M. Janssen, M. M. Fogler & D. N. Basov. “Edge plasmons and plane plasmons in graphene nanoribbons”. *Nano Lett.* 15(12), 8271-8276 (2015).

Z. Fei, E. G. Iwinski, G-X. Ni, L. M. Zhang, W. Bao, A. S. Rodin, Y. Lee, M. Wagner, M. K. Liu, S. Dai, M. Goldflam, M. Thiemens, F. Keilmann, C. N. Lau, A. H. Castro-Neto, M. M. Fogler & D. N. Basov. “Tunneling Plasmonics in Bilayer Graphene”. *Nano Lett.* 15(8), 4973-4978, (2015).

S. Dai, Q. Ma, M. K. Liu, T. Andersen, Z. Fei, M. D. Goldflam, M. Wagner, K. Watanabe, T. Taniguchi, M. Thiemens, F. Keilmann, G. C. A. M. Janssen, S-E. Zhu, P. Jarillo-Herrero, M. M. Fogler & D. N. Basov. “Graphene on hexagonal boron nitride as a tunable hyperbolic metamaterial”. *Nature Nanotech.* 10, 682-686 (2015).

M. K. Liu, A. J. Sternbach, M. Wagner, T. V. Slusar, T. Kong, S. L. Bud'ko, S. Kittiwatanakul, M. M. Qazilbash, A. McLeod, Z. Fei, E. Abreu, J. Zhang, M. Goldflam, S. Dai, G-X. Ni, J. Lu, H. A. Bechtel, M. C. Martin, M. B. Raschke, R. D. Averitt, S. A. Wolf, H-T. Kim, P. C. Canfield & D. N. Basov. “Phase transition in bulk single crystals and thin films of VO₂ by nanoscale infrared spectroscopy and imaging”. *Phys. Rev. B* 91, 245155 (2015).

S. Dai, Q. Ma, T. Andersen, A. S. McLeod, Z. Fei, M. K. Liu, M. Wagner, K. Watanabe, T. Taniguchi, M. Thiemens, F. Keilmann, P. Jarillo-Herrero, M. M. Fogler & D. N. Basov. “Subdiffractional focusing and guiding of polaritonic rays in a natural hyperbolic material”. *Nature Comm.* 6, 6963 (2015).

M. K. Liu, M. Wagner, J. Zhang, A. S. McLeod, S. Kittiwatanakul, Z. Fei, E. Abreu, M. Goldflam, A. Sternbach, S. Dai, K. West, M. M. Fogler, J. Lu, A. Stuart, D. N. Basov, “Symmetry breaking and geometric confinement in VO₂: Results from a three-dimensional infrared nano-imaging”, *Appl. Phys. Lett.* 104, 121905 (2014).

S. Dai, Z. Fei, A. S. Rodin, W. Gannett, M. Wagner, W. Regan, A. S. McLeod, M. Liu, M. Thiemens, G. Dominguez, A. H. Castro Neto, A. Zettl, F. Keilmann, M. M. Fogler, D. N. Basov, “Tunable Phonon Polaritons in Atomically Thin van der Waals Crystals of Boron Nitride”, *Science* 343, 1125-1129 (2014).

Z. Fei, A. S. Rodin, W. Gannett, S. Dai, W. Regan, M. Wagner, M. K. Kiu, A. S. McLeod, G. Dominguez, M. Thiemens, A. H. Castro Neto, F. Keilmann, A. Zettl, R. Hillenbrand, M. M. Fogler, D. N. Basov, “Electronic and plasmonic phenomena at graphene grain boundaries”, *Nature Nanotech.* 8, 821-825 (2013).

M. K. Liu, M. Wagner, E. Abreu, S. Kittiwatanakul, A. S. McLeod, Z. Fei, M. Goldflam, S. Dai, M. Fogler, J. Lu, S. A. Wolf, R. D. Averitt, D. N. Basov, “Anisotropic electronic state via spontaneous phase separation in strained Vanadium dioxide films”, *Phys. Rev. Lett.* 111, 096602 (2013).

ABSTRACT OF THE DISSERTATION

Hyperbolic Phonon Polaritons in hexagonal boron nitride

by

Siyuan Dai

Doctor of Philosophy in Physics

University of California, San Diego, 2017

Professor Dimitri N. Basov, Chair

Uniaxial materials whose axial and tangential permittivities have opposite signs are referred to as indefinite or hyperbolic media. While hyperbolic responses are normally achieved with artificially fabricated nanostructures, hexagonal boron nitride (hBN) naturally possesses this property due to the anisotropic phonons in the mid-infrared. In this dissertation, we studied polaritonic phenomena in hBN using scattering-type scanning near-field optical microscopy (s-SNOM). We performed infrared nano-imaging of highly confined and low-loss hyperbolic phonon polaritons (HP²s) in hBN. The polariton wavelength was shown to be governed by the hBN thickness according to a linear law persisting down to few atomic layers. We have also carried out

the tunable hyperbolic response in metastructures comprised of a monolayer graphene deposited on hBN. Electrostatic gating of the top graphene layer allows for the modification of wavelength and intensity of HP²s in bulk hBN. The physics of the modification originates from the plasmon-phonon coupling in the hyperbolic medium. Furthermore, we demonstrated the “hyperlens” for subdiffractional focusing and imaging using a slab of hBN with a record high resolution due to the natural lattice structure in hBN. Finally, we have systematically studied the relative efficiency of polariton emission in two-dimensional materials in the case of HP²S in hBN. We have observed polariton waves launched by various kinds of emitters and compared their relative efficiency and analyzed the origins of the efficiency difference.

Chapter 1

Introduction

Nanophotonics and plasmonics constitute the study of nanoscale optical phenomena and the interaction between light and matter. Latest research in this field usually relates to surface plasmon polaritons (SP²s) – density waves of electrons originating from hybridization between light and collective electron oscillation – that propagate along metal surfaces like the ripples that spread across the pond surface after a stone was dropped therein. The capability of carrying optical energy in SP²s with wavelengths smaller than that of free space photons leads to useful applications including plasmonic sensing, nano-imaging and bio-medical treatment. However, current difficulties, such as relatively poor confinement, significant losses and lack of tunability, hinder applications of metal-based plasmonics. One prospective solution to these difficulties is to explore nano-plasmonics employing van der Waals (vdW) materials – layered nanostructures bonded together by weak vdW forces. Graphene, a representative vdW material possessing high electron mobility, is ideal for low-loss nano-plasmonics

with extremely high optical confinement since the SP^2 s are supported in few-atomic-layer vdW structures. Alternatively, one could utilize other insulating vdW systems such as hexagonal boron nitride (hBN) supporting phonon polaritons – hybrid electromagnetic waves between light and phonons (lattice vibrations). Phonon polaritons can play a similar role to plasmon polaritons, but suffer less from Ohmic loss due to its insulating nature.

In this dissertation, we utilize infrared (IR) nano-imaging and nano-spectroscopy to study phonon polaritons in hBN and its hybridization with SP^2 s in graphene. Specifically, the antenna-based scattering-type scanning near-field optical microscopy (s-SNOM) employed in our investigation allows launching, probing and imaging of propagating polariton waves in hBN and graphene. The real-space images of the polariton waves obtained in these s-SNOM experiments provide fruitful information to reveal the intriguing properties of nano-polaritonics.

In Chapter 2 we report the discovery of phonon polaritons in hexagonal boron nitride. By using state-of-the-art IR nano-imaging and nano-spectroscopy technique, we show for the first time that vdW crystals can support phonon polaritons. Importantly, the layered nature of hBN and other vdW crystals enable the control over polaritonic waves by varying the crystal thickness or number of stacking layers through exfoliation techniques. Similar to SP^2 s in metals or graphene, phonon polaritons offer a practical means to concentrate electromagnetic energy on lengthscales that are several orders of

magnitude shorter than the IR/optical wavelength (λ_{IR}). Unlike SP²s, such strongly confined phonon polaritons are immune to electronic losses and therefore exhibit dramatically longer propagation lengths. We directly demonstrate polariton propagation lengths as long as several micrometers through IR nano-imaging measurements. Furthermore, we present a novel technique for mapping the entire energy-momentum dispersion of these modes within a single nano-resolved measurement. Such a remarkably efficient nano-optical technique will merit broad applications to investigations of polaritonic modes in other materials.

Chapter 3 provide unambiguous experimental evidence for subdiffraction focusing via phonon polaritons in a natural hyperbolic material hBN. We demonstrated that anisotropic phonon resonances of hBN result in the hyperbolic response, the highly desirable capability most commonly discussed in the context of electromagnetic metamaterials but revealed for the first time in our experiment. The phonon polaritons in hBN are therefore referred to as hyperbolic phonon polaritons (HP²s) since our experimental discovery. Based on the tilted propagation nature of HP²s, we accomplished subdiffraction focusing and subsurface image projection using a slab of natural hBN. We achieved the subdiffraction focusing with a resolution of $\lambda_{\text{IR}}/33$, much smaller than previous records ($\sim \lambda_{\text{IR}}/10$) using metamaterial structures. This superior figure of merit originates from the high magnitude of upper momentum cutoff set by the interatomic spacing in hBN. At a specified frequency, 1 to 1 image projection from the subsurface

was also demonstrated when HP²s propagate along the optical (vertical) axis of hBN.

In Chapter 4 we complete a study of hybrid polaritons and the tunable hyperbolic properties of metastructures of graphene on hexagonal boron nitride (G-hBN). The key experimental result in this chapter is that the hybrid polaritons detected in G-hBN metastructures are neither purely SP²s of graphene nor entirely HP²s of hBN. Instead, these propagating waves possess the combined virtues of both these two nanoscale phenomena. In the experiment, we demonstrated these hybrid modes retain the high optical confinement and relatively low loss of hBN phonon polaritons, while acquiring the electrical tunability of SP²s in graphene. The G-hBN devices can be referred to as “metastructures” because the attained electromagnetic properties of these structures are not revealed by either of the two constituent elements.

Finally, Chapter 5 introduces our study of polariton emitters and emission efficiency of hyperbolic phonon polaritons in hBN. We report the first systematic nano-resolved study of polariton emission efficiency – the ability to convert optical photons into propagating polaritons – among various polariton emitters in hBN. In addition to the conventional atomic force microscope (AFM) tip emitter, we found that hyperbolic phonon polaritons in hBN can be launched by other forms of emitters, such as crystal edges, lithographic nanostructures, as well as surface impurities and defects. We compared the emission efficiency for these different polariton emitters and analyzed the origins of their comparative emission efficiency. The AFM tip emitter was proved to possess the

highest efficiency due to the metallic nature and strong coupling with the high-momentum polariton waves.

Chapter 2

Infrared nano-imaging of phonon polaritons in hexagonal boron nitride

2.1 Abstract

van der Waals heterostructures assembled from atomically thin crystalline layers of diverse two-dimensional solids are emerging as a new paradigm in the physics of materials. We use infrared nano-imaging to study the properties of phonon polaritons in a representative van der Waals crystal, hexagonal boron nitride. We launched, detected and imaged the polaritonic waves in real space and altered their wavelength by varying the number of crystal layers in our specimens. The measured dispersion of polaritonic waves was shown to be governed by the crystal thickness according to a scaling law that persists down to a few atomic layers. Our results are likely to hold true in other polar van der Waals crystals and may lead to their new functionalities.

2.2 Introduction

Layered van der Waals (vdW) crystals consist of individual atomic planes weakly coupled by vdW interaction, similar to graphene monolayers in bulk graphite [1-3]. These materials can harbor superconductivity [2] and ferromagnetism [4] with high transition temperatures, emit light [5,6] and exhibit topologically protected surface states [7], among many other effects [8]. An ambitious practical goal [9] is to exploit atomic planes of van der Waals crystals as building blocks of more complex artificially stacked structures where each such block will deliver layer-specific attributes for the purpose of their combined functionality [3]. Here we explore the behavior of phonon polaritons in hexagonal boron nitride (hBN), a representative vdW crystal. The phonon polaritons are collective modes that originate from coupling of photons with optical phonons [10] in polar crystals that have been investigated in the context of energy transfer [11,12], coherent control of the lattice [13], ultra-microscopy [14,15], “superlensing” [16] and metamaterials [17,18]. Tunable phonon polaritons that we discovered in hBN by direct infrared (IR) nano-imaging set the stage for the implementation of all these appealing concepts in vdW heterostructures. Polaritonic effects reported here are most certainly generic to other classes of polar vdW solids since these materials commonly show optical phonons. The hBN investigate here stands out in view of its light constituent elements yielding the superior strength of phonon resonances that span a broad region of technologically important IR band.

2.3 Experimental details

IR nano-imaging and Fourier transform infrared nano-spectroscopy (nano-FTIR) experiments were performed at UCSD using a scattering-type scanning near-field optical

microscope (s-SNOM) (see Supplementary Information). The physics of polariton imaging using s-SNOM is akin to nano-imaging of surface plasmons [19,20] (Fig. 1a). In short, we illuminated the metalized tip of an atomic force microscope (AFM) with an IR beam. We used quantum cascade lasers (QCLs) with tunable frequency $\omega = 1/\lambda_{\text{IR}}$, where λ_{IR} is IR beam wavelength and a broad-band difference frequency generation (DFG) laser system [21]. Our AFM tip with curvature radius $a \approx 25$ nm is polarized by the incident IR beam. The light momenta imparted by the tip extend to the typical range of momenta supporting phonon polaritons in hBN (Fig. 2e). Therefore, the strong electric field between the tip and sample provides the necessary momentum to launch polariton waves of wavelength λ_p that propagate radially outward from the tip along the hBN surface. AFM tips exploited in our nano-spectroscopy instrument are commonly referred to as “optical antennas” [22]: an analogy that is particularly relevant to describe the surface wave launching function of the tip. Upon reaching the sample edge, polaritonic waves are reflected back, forming a standing wave between the tip and hBN edge. As the tip is scanned towards the edge, the scattering signal collected from underneath the tip reveals oscillations with the period of $\lambda_p/2$.

2.4 Experimental data

Representative nano-imaging data are displayed in Fig. 2.1(b) and Fig. 2.1(d) – (f) where we plot the normalized near-field amplitude $s(\omega) = s_{\text{hBN}}(\omega)/s_{\text{Au}}(\omega)$ at several IR frequencies in the 1550 to 1580 cm^{-1} range. Here, $s_{\text{hBN}}(\omega)$ and $s_{\text{Au}}(\omega)$ are the scattering amplitudes for, respectively, the sample and the reference (Au-coated wafer)

(Supplementary Information). The amplitudes were demodulated at the third or the fourth harmonic of the tapping frequency to isolate the genuine near field signal [22]. The images in Fig. 2.1(b) – (f) were taken for a tapered hBN crystal of thickness $d = 256$ nm. They reveal a hatched pattern of periodic maxima — fringes — of $s(\omega)$ running parallel to the edges, with the “hot spots” located where the two or more fringes intersect. We observed similar fringe patterns in other hBN samples, including those that are only a few atomic layers thick (Fig. 1(g)). Such patterns are readily accounted for (Fig. 1(c)) within a phenomenological theory that considers reflections from the tapered edges (Supplementary Information).

Data in Fig. 2.1 allow one to obtain the polariton wavelength λ_p simply by doubling the fringe period and the corresponding momentum can be calculated as $q = 2\pi/\lambda_p$. We used two approaches to determine the dispersion relation $q = q(\omega)$ of the polaritons. One method [15,19,20] is to analyze the periodicity of fringes at discrete frequencies of the IR source (Fig. 1(b), (d) – (g)). We have complemented this procedure with a technique capable of capturing the entire dispersion in the course of one single scan of our nanoscope. We executed this line scan on an hBN crystal with a large surface area to ensure that the $L = 0$ boundary is the principal reflector for the tip-launched polaritons (Fig. 2.2(a)). Such a line scan (Fig. 2.2(a) - (b), (d)) is comprised of a series of broad-band nano-FTIR spectra taken at every pixel. Starting in the region of unobscured SiO_2 substrate ($L < 0$) and continuing through the hBN crystal ($L > 0$), we combined the spectra from all pixels along the line scan and thus obtained a two-dimensional map $s(L, \omega)$ shown in Fig. 2.2(b). In the plot, we observed a series of resonances that systematically vary with frequency ω and the

distance from the sample edge L . The nano-FTIR spectra from three representative positions are shown in Fig. 2.2(c). Each of the frames in Fig. 2.2(c) and each pixel in Fig. 2.2(b) unveil phonon polaritons in the frequency domain. The momentum q corresponding to each ω in this map can be found from the fringe periodicity along the $\omega = \text{constant}$ cut. Therefore, a single line scan is sufficient to extract the complete dispersion profile of any surface mode.

The two approaches for mapping the surface wave dispersion produced consistent results (triangles in Fig. 2.2(b) were obtained from monochromic imaging). The broadband line scan data (dots in Fig. 2.2(e)) allowed us to probe the dispersion in the $\omega - q$ parameter space (1430 to 1530 cm^{-1}) that cannot be investigated through the single-frequency imaging because of unavailability of proper QCLs. The experimental data for phonon polariton dispersion in Fig. 2.2(e) are in excellent agreement with the modeling results. Briefly, the surface polaritons correspond to the divergences of the reflectivity $r_p(q + i\kappa, \omega)$ of the system at complex momenta $q + i\kappa$ [10]. For $\lambda_p \ll \lambda_{\text{IR}}$, we derived the analytical formula for polariton dispersion (Supplementary Information):

$$q(\omega) + i\kappa(\omega) = -\frac{\psi}{d} \left[\arctan\left(\frac{\varepsilon_a}{\varepsilon_{\perp}\psi}\right) + \arctan\left(\frac{\varepsilon_s}{\varepsilon_{\perp}\psi}\right) + \pi l \right], \quad \psi = \frac{\sqrt{\varepsilon_{//}}}{i\sqrt{\varepsilon_{\perp}}}, \quad (2.1)$$

where $\varepsilon_a(\omega)$, $\varepsilon_{\perp}(\omega)$, $\varepsilon_{//}(\omega)$ and $\varepsilon_s(\omega)$ are the dielectric functions of air, hBN (for directions perpendicular and parallel to the c -axis), and SiO_2 substrate, respectively. The propagating modes correspond only to those integer l (if any) for which the loss factor $\gamma = \alpha\kappa/q$ is positive and less than unity. Parameter $\alpha = \pm$ is the sign of the group velocity $d\omega/dq$ (Supplementary Information). An instructive way to visualize both the dispersion and the

damping is via a false color plot of $\text{Im } r_p(q, \omega)$ [23] (Supplementary Information) at real q and ω (Fig. 2.2(e)). Our data line up with the topmost of these curves, which corresponds to the principal $l = 0$ branch (Supplementary) in Eq. 2.1.

Additional insights into the photonic and polaritonic properties of hBN were obtained by analyzing the frequency dependence of the nano-FTIR spectra. We collected the spectrum in Fig. 2.2(f) far away from the hBN edges where the surface waves are damped and the scattering amplitude signal is solely governed by the local interaction with the phonon resonances [24]. Two of these resonances centered around 770 cm^{-1} and 1370 cm^{-1} are due to the c -axis and the in-plane phonon modes of hBN, respectively [25,26]. The hump-dip feature around 1100 cm^{-1} originates from the SiO_2 substrate [27]: a consequence of a partial transparency of our specimen. The quantitative relation between this spectrum, the reflectivity $r_p(q, \omega)$, and the fundamental phonon modes can be established by numerical modeling of the tip-sample interaction (Supplementary Information). The right plot of Fig. 2.2(f) indicates that our model captures the gross features of the data. Moreover, the hBN is an example of a natural hyperbolic material [28]: a crystal possessing the in-plane and out-of-plane components of the dielectric tensor having the opposite signs so that $\text{Re } \varepsilon_{\perp} \cdot \text{Re } \varepsilon_{\parallel} < 0$. Hyperbolic regions are marked in green in Fig. 2.2(f).

The layered nature of vdW materials, including hBN, facilitates the control of both the wavelength and the amplitude of polaritonic waves by varying the thickness d of the specimens. Representative line profiles (Fig. 2.3(a)) for specimens with d in the range of $150 - 250 \text{ nm}$ were taken normal to the crystal edge at $L = 0$. The thickness was measured

simultaneously with the scattering amplitude through the AFM topography. All fringe profiles share the same line form with a prominent peak close to the edge followed by weaker peaks that are gradually suppressed away from the edge. The oscillation period, equal to $\lambda_p/2$ (arrows in Fig. 2.3(a)), systematically decreases as the samples become thinner. This scaling extends down to a few atomic layers (Fig. 2.3(b) – (c)).

The measured polariton wavelength (Fig. 2.3(e)) agrees with the theoretical predictions (Fig. 2.3(d)). For λ_p smaller than about one half of $\lambda_{\text{IR}} = 7.1 \mu\text{m}$, the polariton wavelength scales linearly with the crystal thickness d , in agreement with Eq. 2.1; at larger λ_p the linear law shows signs of saturation, also in accord with our model (inset of Fig. 2.3(e)). Experimentally, the phonon polaritons display thickness-tunability persisting down to three atomic layers (Fig. 2.3(b) – (c)). We detected polaritons in even thinner samples (bilayer and monolayer hBN). However, the quantitative analysis of these latter data is complicated because of the increasing role of the substrate in the polaritonic response that calls for further experiments on suspended membranes.

2.5 Conclusion and Outlook

Similar to surface plasmons, the phonon polaritons allow one to confine and control electromagnetic energy at the nanoscale [29]. In fact, the line form in Fig. 2.3(a) strongly resembles plasmonic standing waves in graphene [19,20]. The confinement factor $\lambda_{\text{IR}}/\lambda_p$ reaches 25 in hBN, comparable to that of plasmons in graphene [19,20]. Yet these compact polaritons in hBN are able to travel at least 5 – 10 μm compared to less than 0.5 μm for graphene plasmons. The corresponding loss factor $\gamma = \alpha\kappa/q$ is around 0.055, much smaller

than a typical γ in graphene. The low damping of polaritons in our insulating samples is consistent with the absence of the electronic losses, the dominant damping channel in plasmonics. The observed losses can likely be further suppressed by improving the crystallographic order of the crystals.

Data in Fig. 2.1 - 2.3 show that phonon polaritons of the desired wavelength and confinement can be engineered by varying the number of atomic layers in hBN by, e.g., exfoliation techniques. Thus, hBN and likely other polar layered materials can be integrated into vdW heterostructures [3] to serve not only as electrically insulating spacers but also as waveguides for weakly damped polaritons capable of traveling over considerable distances. Additionally, the hyperbolic response of few-layer hBN is appealing in the context of unique nano-photonics characteristics of this class of solids [28].

2.6 Supplementary information

2.6.1 Preparation and characterization of hBN crystals

Microcrystals of hBN were exfoliated from bulk samples and then transferred to Si wafers capped with 300 nm-thick SiO₂ layer. We explored bulk hBN samples from two different sources including commercially available samples (www.momentive.com) and also specimens synthesized by means of high pressure techniques as described in Ref. [30]. We observed reproducible polaritonic effects irrespective of the origin of our microcrystals. Raman spectroscopy was applied to characterize the hBN crystals. (Fig. 2.4(b)). These Raman spectra were in accord with the literature data for high-quality hBN specimens [31]. We note that one can easily distinguish hBN crystals of different thickness by their color

under the optical microscope (Fig. 2.4(a)) [32].

2.6.2 Infrared nano-imaging and nano-FTIR

The nano-imaging and Fourier transform infrared nano-spectroscopy (nano-FTIR) data were obtained using a commercial scattering-type scanning near-field optical microscope (s-SNOM) (www.neaspec.com) based on a tapping-mode atomic force microscope (AFM). The tapping frequency and amplitude of the AFM are about 250 kHz and 70 nm, respectively. In Fig. 2.5, we show schematics of our infrared (IR) sources and of the s-SNOM system. These IR sources include tunable quantum cascade lasers (QCLs) (www.daylightsolutions.com) and a broad-band source based on a difference frequency generation (DFG) system (www.lasnix.com). In combination, these sources cover a broad frequency range from 700 to 2300 cm^{-1} (Fig. 2.5). By focusing the IR beam onto the metalized AFM tip, we were able to probe the polaritonic effects of hBN. The back-scattered signal by the tip is registered by pseudoheterodyne interferometric detection and then demodulated at the n -th harmonics of the tapping frequency yielding background free images. In this work, we chose $n = 3$ or 4.

2.6.3 Modeling of tip-launched phonon polariton waves

We start with describing a model that captures the essence of the observed real-space patterns in Figs. 2.1 - 2.3 on purely phenomenological grounds. This model assumes that the near-field contrast detected by the s-SNOM is in the linear response regime and is purely local. In other words, the deviation of the s-SNOM signal from the area average is

given by some linear functional $E(\mathbf{r})$ of the electric potential $\phi(\mathbf{r})$ directly underneath the tip. The qualitative aspects of the results do not depend on the precise relation between $\phi(\mathbf{r})$ and $E(\mathbf{r})$ as long as this relation is linear. For definiteness, one can think that $E(\mathbf{r})$ represents the deviation of the z -component of the local electric field from its average value, so we use the term “field” to refer to it from now on. We further assume that tip-launched polaritons are characterized by the radially symmetric field distribution ($r = |\mathbf{r}|$)

$$E(r) = E_0 e^{iqr} \times \begin{cases} e^{-r^2/4r_0^2}, & r < r_0, \\ e^{-1/4}(r_0/r)^{1/2}, & r \geq r_0, \end{cases} \quad (2.2)$$

where we take $r_0 = \lambda_p/4$ (the diffraction limit), λ_p is the phonon polariton wavelength. Eq. 2.2 is designed to have the property that $E(r)$ goes to a constant underneath the tip ($r \rightarrow 0$) and behaves as an outgoing cylindrical wave at large distances. The momentum of this wave is a complex number

$$q_p = q + i\kappa = q(1 + i\gamma) = \frac{2\pi}{\lambda_p}(1 + i\gamma), \quad (2.3)$$

where $\gamma = \kappa/q$ is the loss factor defined above.

2.6.4 Near-field imaging of phonon polaritons

The observed polariton interference fringes (Figs. 2.1 - 2.3) originate from the superposition of tip-launched polariton waves with those reflected back from the edges of the hBN crystals. The edge-reflected waves can be approximately calculated using the method of images. For a single edge (Fig. 2.6(a)), the total field under the tip (solid red arrow) is given by $E_{\text{tot}} = E(0) + E(2L)r_{sp}$, where L is the tip-edge distance, r_{sp} is the complex coefficient of reflection off the edge, and function $E(r)$ is given by Eq. 2.2.

For the tapered hBN crystal (Fig. 2.1), the polariton waves launched by the tip may experience multiple reflections. Therefore, we introduce the index $m = 1, 2, \dots$ to label the waves that are reflected m times by the edges before arriving back to the tip; we refer to them as the m -th order waves. The locations of the corresponding image sources are obtained by m consecutive mirror reflections of the tip across the alternate edges. We refer to them as the m -th order images. In Fig. 2.6(b) we show these multiple tip images (hollow dots) for one representative tip position (solid green dot). We use the double index “ m,n ” to label the n -th ($n = 1$ or 2) possible position of the m -th order images. Let $d_{m,n}$ be the distance between the n -th position of the m -th order images and the tip. The total polaritonic field underneath the tip can be expressed as:

$$E_{\text{tot}} = \sum_m \sum_n E(d_{m,n}) r_{sp}^m. \quad (2.4)$$

Using this formula, we computed E_{tot} for every position within a triangular area representing the tapered hBN crystal in Fig. 2.1. For this particular sample geometry only $m \leq 3$ images contribute to the formation of the interference patterns in the field of view.

Our simulation results are shown in Fig. 2.1(c). We find a good qualitative agreement with the actual data (Fig. 2.1(b)) using the parameters $\gamma = 0.055$ and $r_{sp} = -0.2 + 0.3i$, which are in accord with the phonon polariton line profiles (Fig. 2.3(a)). Simulation images for the different choices of γ value along with the experimental data are shown in Fig. 2.7. The fact that the absolute value of r_{sp} is smaller than unity suggests that either the reflection has a strong diffuse component or a significant amount of energy is dissipated into degrees of freedom other than the principal polariton branch ($l = 0$ in the main text).

Among the dominant factors reducing the reflectivity of polaritons are the roughness as well as canted nature of the edges.

Besides analyzing the two-dimensional interference patterns, we also examined the line profiles (Fig. 2.3(a)). Noticing a marked resemblance between the observed phonon polariton fringes and the plasmonic interference fringes in graphene [19,20], we attempted to roughly estimate the former using the simulation developed previously for the latter. In this way, we again arrived at the estimated range $\gamma \approx 0.04 - 0.07$.

2.6.5 Optical constants and infrared reflectivity of hBN

The infrared reflectivity of boron nitride (BN) has been investigated by several groups [25,33-35]. A consensus is that both the in-plane and the out-of-plane dielectric function can each be described by a single Lorentzian:

$$\varepsilon_{\mu} = \varepsilon_{\infty\mu} + \varepsilon_{\infty\mu} \frac{(\omega_{LO,\mu})^2 - (\omega_{TO,\mu})^2}{(\omega_{TO,\mu})^2 - \omega^2 - i\omega\Gamma_{\mu}}, \quad \mu = \perp, //, \quad (2.5)$$

with nearly the same values of the optical phonon frequencies $\omega_{TO,\mu}$ and $\omega_{LO,\mu}$ reported by all the groups. These values are also in a good agreement with the results of *ab initio* calculations [36,37]. However, we met some difficulty finding reliable experimental data in the literature for limiting high-frequency values $\varepsilon_{\infty\mu}$ and especially the optical phonon broadening Γ_{μ} . The aforementioned experiments studied boron nitride samples obtained by pyrolysis [25], chemical-vapor-deposition (CVD) [33], and magnetron sputtering [34,35]. All of these materials were composed of misoriented (angle spread $\theta \sim \pm 30^\circ$) grains of sub-10 nm size. For such small grain sizes, the linewidth broadening of the

phonons can be considerably larger than what is expected in single-crystals, as was shown by Raman studies [38,39]. On the other hand, Γ_{μ} as small as a few cm^{-1} was estimated for the CVD-grown rhombohedral boron nitride. This material has the same in-plane layer structure and nearly the same phonon frequencies as CVD hBN but a much higher degree of crystallographic order [33]. For all of the above reasons, in our calculations we used the parameters of Cai *et al.* [36] with the broadening $\Gamma_{\parallel} = 4 \text{ cm}^{-1}$ and $\Gamma_{\perp} = 5 \text{ cm}^{-1}$ in order to reproduce the observed loss factor $\gamma \approx 0.055$ at 1550 cm^{-1} (see Fig. 2.3(f)).

The dielectric function of Eq. 2.5 serves as input into the calculation of the complex reflectivity $r_p(q, \omega)$ and therefore of the phonon polariton dispersion. Although our system consisted of three layers: hBN, SiO_2 , and Si, at large q relevant for our experiments, the electric field of the polaritons is mostly confined in the first two layers. Therefore, it is legitimate to approximate $r_p(q, \omega)$ by the reflectivity of a simpler hBN/ SiO_2 structure. The $r_p(q, \omega)$ can be derived from the Fresnel equations for a three-layer structure shown in Fig. 2.8:

$$r_p = \frac{r_a + r_s e^{i2k_e^z d}}{1 + r_a r_s e^{i2k_e^z d}}, \quad (2.6)$$

$$r_a = \frac{\varepsilon_{\perp} k_a^z - \varepsilon_a k_e^z}{\varepsilon_{\perp} k_a^z + \varepsilon_a k_e^z}, \quad (2.7)$$

$$r_s = \frac{\varepsilon_s k_e^z - \varepsilon_{\perp} k_s^z}{\varepsilon_s k_e^z + \varepsilon_{\perp} k_s^z},$$

where the subscripts “ a ”, “ \perp ” and “ s ” refer to air, hBN (the component normal to the c -axis), and SiO_2 , respectively. Functions r_a and r_s have the meaning of the reflectivity of the air/hBN and hBN/ SiO_2 interfaces, d is the thickness of the hBN crystal and k_i^z represents

the z -axis momentum of the photon in layer i . For $i = a$ and s , it is given by

$$k_i^z = \sqrt{\varepsilon_i \frac{\omega^2}{c^2} - q^2} \quad \text{with } \varepsilon_i \text{ being the dielectric function. The subscript “}e\text{” stands for}$$

“extraordinary ray” of hBN, which has uniaxial anisotropy. The corresponding momentum

$$\text{is } k_e^z = \sqrt{\varepsilon_{\perp} (\omega/c)^2 - \frac{\varepsilon_{\perp}}{\varepsilon_{\parallel}} q^2} \quad [40].$$

2.6.6 The origin of the multiple polariton branches

At large q we can make the approximation $k_a^z \approx k_s^z \approx iq$ and

$$k_e^z = iq \frac{\sqrt{\varepsilon_{\perp}}}{\sqrt{\varepsilon_{\parallel}}} = \frac{q}{\psi}, \quad (2.8)$$

in the preceding formulas, which enables us to further simplify the expression for r_p . Using straightforward algebraic manipulations, one is led to the analytic solution for the poles of r_p , Eq. 2.1 above. Alternatively, a more physical derivation can be offered as follows. If dissipation is neglected, so that both ε_{\perp} and ε_{\parallel} are real, the admissible value of momentum k_e^z obey the Fabry-Perot quantization condition

$$2k_e^z d + 2\phi_a + 2\phi_s = 2\pi m, \quad (2.9)$$

where $2\phi_a$ and $2\phi_s$ are the phases of the reflection coefficients r_a and $-r_s$, i.e., the phase shifts for (inner) reflection of the extraordinary ray at the hBN-air and hBN-substrate interfaces. From Eq. 2.6 and Eq. 2.7 we find

$$\phi_j = \arctan\left(\frac{\varepsilon_j}{\varepsilon_{\perp}\psi}\right), \quad j = a, s. \quad (2.10)$$

Combining Eq. 2.8 – 2.10 we arrive at

$$q = -\frac{\psi}{d}(-\pi m + \phi_a + \phi_s). \quad (2.11)$$

It is convenient to define $l = -m = 0, 1, \dots$ to ensure that $\text{Re } q > 0$. If the losses are now included, the in-plane momentum would acquire an imaginary part $q \rightarrow q + i\kappa$. After these substitutions, Eq. 2.11 becomes the same as the desired result, Eq. 2.1.

According to Eq. 2.1, the $0 < \gamma < 1$ condition can be satisfied within the Reststrahlen bands of hBN confined within the transverse ω_{TO} and longitudinal ω_{LO} phonon frequencies (Fig. 2.3(d)). Our imaging data probe mainly the band due to the upper Reststrahlen band, from $\omega_{\text{TO},\perp} = 1367 \text{ cm}^{-1}$ to $\omega_{\text{LO},\perp} = 1610 \text{ cm}^{-1}$ [25] where ε_{\perp} is real and negative, whereas ε_{\parallel} is almost real and positive. The polariton branches all start at $\omega_{\text{TO},\perp}$ at low q and disperse with the positive slope ($\alpha = +$) towards the limiting value of $\omega_{\text{LO},\perp} = 1610 \text{ cm}^{-1}$ at large q .

Instead of looking for the poles of r_p in the complex plane, one can determine the polariton dispersion from the maxima of $\text{Im } r_p$ at real momenta. This numerical method gives results that closely agree with our analytical Eq. 2.1 at large q where the latter equation is valid, see Fig. 2.2(e). The positions of high-intensity lines in this plot give q , while their apparent widths characterize the dissipation κ [10].

Let us now briefly discuss the multiple branches of the polariton dispersion. As explained above, the $l > 0$ branches have a simple interpretation as the Fabry-Perot resonances confined between the two interfaces of the hBN crystal. The same phenomenon occurs in planar waveguides, so these modes can be termed “waveguide modes” [28]. In

our case the polariton branches are separated from one another by equal increments $\frac{\pi\psi}{d}$ in the momentum space. It is unusual however that this number is real while q itself is much larger than the photon momentum. In other words, it is unusual to have propagating modes far outside the light-cone. This fact can be traced to parameter ψ (defined in Eq. 2.1 or Eq. 2.8) being real, which is unique to hyperbolic materials such as hBN. Unfortunately, none of the $l > 0$ modes has shown evident features in the experiments so far. Observation of these “waveguide” modes may have been inhibited by imperfections of the sample edges and the current signal/noise ratio limitation.

Finally, it may be worth commenting on applicability of our continuum-medium approach to hBN crystals with just a few atomic layers N . Experimentally, our Eq. 2.1 is seen to be in quantitative agreement with the measurements even in the thinnest samples reported here, $N = 3$. On the theory side, the answer can be gleaned from the theoretical calculations of Michel and Verberck [41]. They suggest that a qualitatively new effect caused by decrease in the number of layers is the character of yet unobserved high-order polariton branches. These authors find that the total number of all branches is finite and equal to N in each Reststrahlen band. Thus, in monolayer hBN there should be only one and in bilayer only two polariton branches in each band. Since we do not see high-order branches even in thick crystals, this distinction cannot yet be verified.

2.6.7 Nano-FTIR spectra simulation

The near-field scattering amplitude $s(\omega)$ shown in Fig. 2.2(f) (right) was computed using the expression for the reflectivity, which accounted for all possible layers (hBN, SiO₂, and Si). It has the same form as Eq. 2.5 except r_s is replaced by r_{sq} :

$$\begin{aligned}
 r_{sq} &= \frac{r_s + r_q e^{i2k_s^z d_s}}{1 + r_s r_q e^{i2k_s^z d_s}} \\
 r_q &= \frac{\varepsilon_q k_s^z - \varepsilon_s k_q^z}{\varepsilon_q k_s^z + \varepsilon_s k_q^z} , \\
 k_q^z &= \sqrt{\varepsilon_q \left(\frac{\omega}{c}\right)^2 - q^2}
 \end{aligned} \tag{2.12}$$

where $d_s = 300$ nm is the SiO₂ thickness and $\varepsilon_q = 11.7$ is the IR dielectric constant of Si. The tip-sample interaction was treated within the quasi-static approximation in which the AFM tip was modeled as a perfectly conducting prolate spheroid of total length 600 nm and the curvature radius 30 nm, as described in our previous work [27]. Figure 2.2(f) indicates that the modeling captures all the main features of the observed spectrum. Two features arise due to two effects. One is the behavior of the ordinary reflectivity r_p at nearly zero momentum, i.e., the photonic response of our hBN/SiO₂/Si system. The other ingredient is the ω – dependence of r_p at very large momenta $q \sim 10^5$ cm⁻¹ set by the curvature radius of the tip and its typical distance from the sample, i.e., the polaritonic effect. The photonic response causes the deep minima at 820 cm⁻¹ and 1625 cm⁻¹. These minima occur near the longitudinal optical (LO) phonon frequencies of hBN, $\omega_{LO,\parallel}$ and $\omega_{LO,\perp}$ at which the far-field reflectivity r_p is close to -1 , see Eq. 2.12), so that the electric field at the surface, proportional to $1 + r_p$, vanishes. (Note that the far-field reflectivity is a very sharp function of frequency near $\omega_{LO,\perp}$. It rapidly changes from -1 to 0 as frequency

increases, giving the well-known reflectivity minimum.) The far-field reflectivity is also responsible for the hump-dip structure near 1100 cm^{-1} , which comes from the optical phonon of the SiO_2 substrate. On the other hand, the resonances centered around 760 cm^{-1} and 1370 cm^{-1} are to a large extent due to the high *near-field* reflectivity, the *raison d'être* of the polaritons. The combination of the far- and near-field response functions anchors these peaks at the transverse optical (TO) frequencies.

2.7 Acknowledgements

This work is supported by DOE-BES, AFOSR, NSF, MURI, NASA and NRF-CRP award.

Chapter 2, in full, is a reprint of the material as it appears in S. Dai, Z. Fei, Q. Ma, A. S. Rodin, M. Wagner, A. S. McLeod, M. K. Liu, W. Gannett, W. Regan, K. Watanabe, T. Taniguchi, M. Thiemens, G. Dominguez, A. H. Castro-Neto, A. Zettl, F. Keilmann, P. Jarillo-Herrero, M. M. Fogler & D. N. Basov. "Tunable Phonon Polaritons in Atomically Thin van der Waals Crystals of Boron Nitride". *Science* 343, 1125-1129 (2014). The dissertation author was the primary investigator and author of this paper.

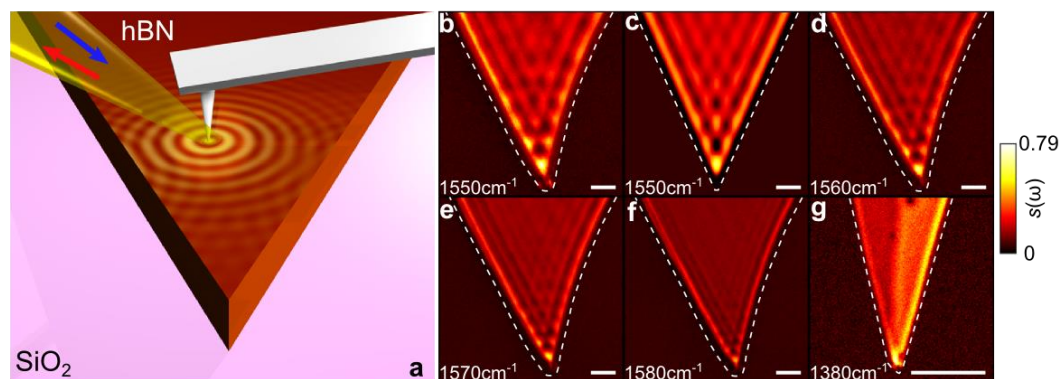


Figure 2.1: Real-space imaging of phonon polaritons on hBN. (a) Schematics. Arrows denote the incident and back-scattered IR light. Concentric yellow circles illustrate the phonon polariton waves launched by the AFM tip and reflected by the two edges of a tapered hBN crystal. (b and d-f) Infrared near-field images of the normalized amplitude $s(\omega)$ defined in the text and taken at different IR frequencies (hBN thickness in (b) – (f) $d = 256$ nm). (c) Simulation of the phonon polariton interference pattern (see Supplementary Information). (g) Phonon polaritons probed in a 3 layer (left) and 4 layer (right) hBN crystals. White dashed line tracks the hBN edges according to the AFM topography. Scale bars: 800 nm.

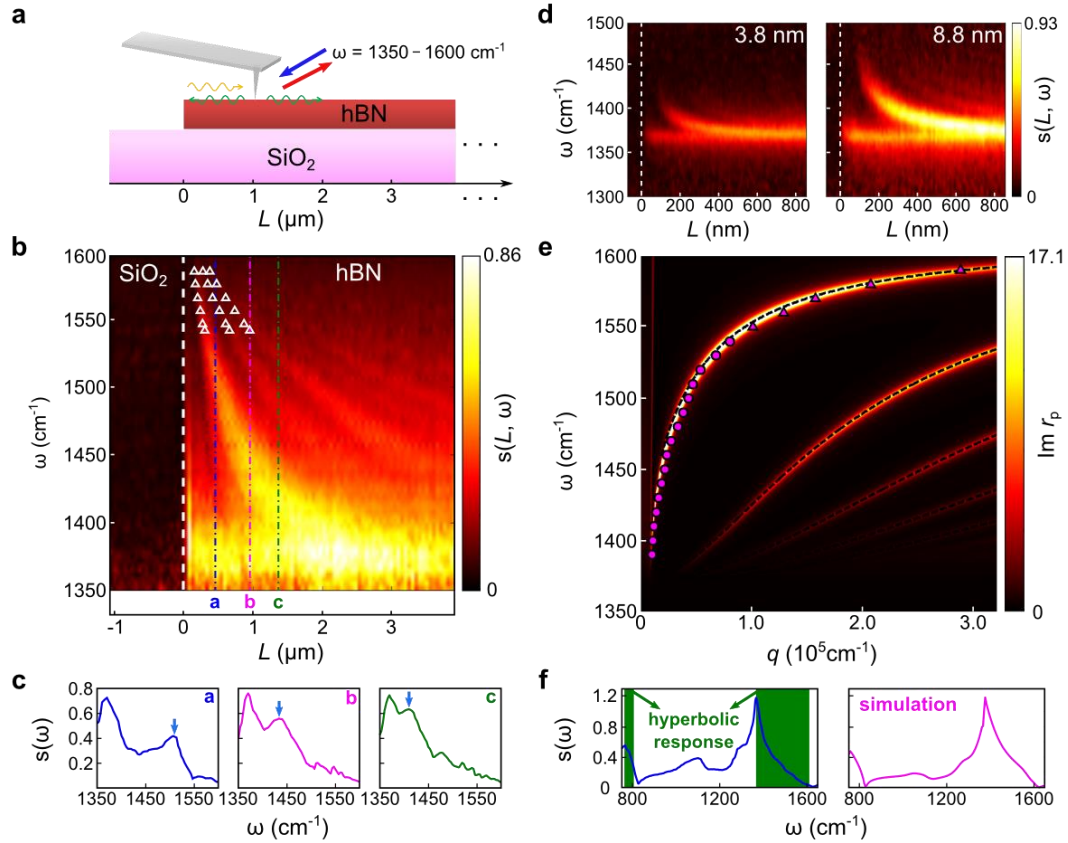


Figure 2.2: The phonon polariton dispersion and nano-FTIR spectra. (a) Schematics of a nano-FTIR line scan across the hBN crystal. Arrows denote the incident and back-scattered IR beam spanning $1350 - 1600 \text{ cm}^{-1}$. Polaritonic waves are launched (green) by AFM tip and then reflected (orange) by hBN edge at $L = 0$. (b) Polaritonic features detected in a single line scan in (a). The normalized scattering amplitude spectra $s(\omega)$ is plotted in the false color scale. White dashed line at $L = 0$ marks the edge of the hBN crystal (thickness $d = 134 \text{ nm}$). Triangles: fringe maxima extracted from monochromatic imaging similar to Fig. 1. (c) Nano-FTIR spectra at three representative locations along the line scan marked in (b). The peaks marked by the arrows correspond to the dominant polariton interference fringe. (d) Phonon polariton features as probed via line scans for ultra-thin hBN crystals with $d = 3.8 \text{ nm}$ (left) and $d = 8.8 \text{ nm}$ (right). (e) The dispersion relation of phonon polaritons in hBN. Triangles: data from monochromatic imaging in Fig. 2.1; dots: the nano-FTIR results from (b). The data are superimposed on a false color plot of calculated $\text{Im } r_p$ (see Supplementary Information) the black dashed lines are from Eq. 2.1. The straight line on the left represents the light line. (f) Nano-FTIR spectrum $s(\omega)$ for the hBN crystal (Fig. 1 (a) – (f)) taken away from the sample edges. The filled (green) part of the data corresponds to hBN’s hyperbolic region where $\text{Re } \epsilon_{\perp} \cdot \epsilon_{\parallel} < 0$.

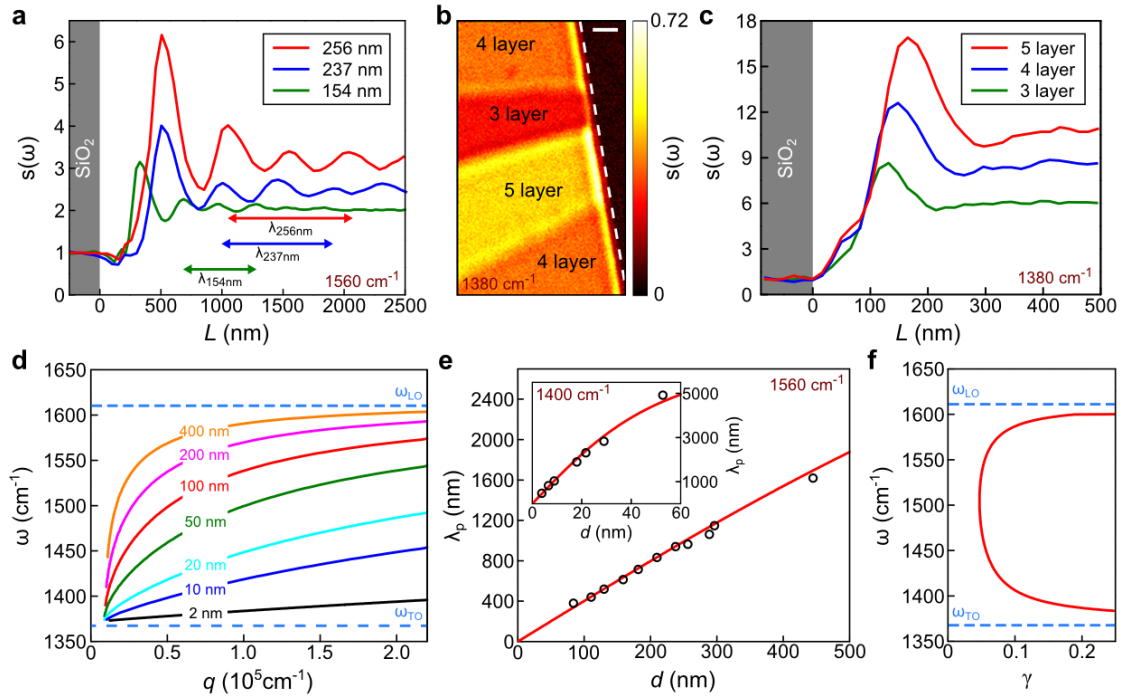


Figure 2.3: The evolution of the phonon polariton wavelength and amplitude with the thickness of hBN crystals. (a) Line profiles of the scattering amplitude $s(\omega)$ at 1560 cm^{-1} for hBN crystals with $d = 154, 237$ and 256 nm . Arrows indicate the polariton wavelength. (b) Near-field image and (c) phonon polariton line profiles for few-layer hBN crystals. White dashed line in (b) tracks the sample boundary. (d) Calculated dispersion relation of the $l = 0$ branch of the phonon polaritons in hBN for various crystal thicknesses. TO and LO frequencies are marked with blue dashed lines. (e) Dots: the wavelength of phonon polaritons probed at 1560 cm^{-1} for crystals with different thickness. Red line: calculated thickness-dependence relation. Inset: thickness-dependence relation probed at 1400 cm^{-1} for ultra-thin hBN crystals. See Supplementary Information for details. (f) Calculated loss factor for phonon polaritons. Scale bar in (b): 400 nm .

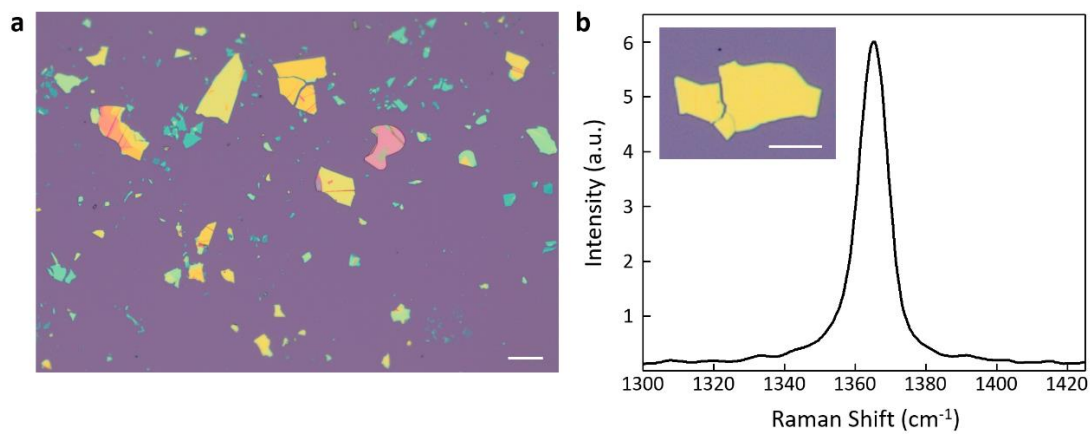


Figure 2.4: Optical microscope image and Raman spectrum of hBN. (a) hBN crystals of different thicknesses under the optical microscope. (b) Raman spectrum of the hBN crystal displayed in the inset. Scale bar: 30 μ m.

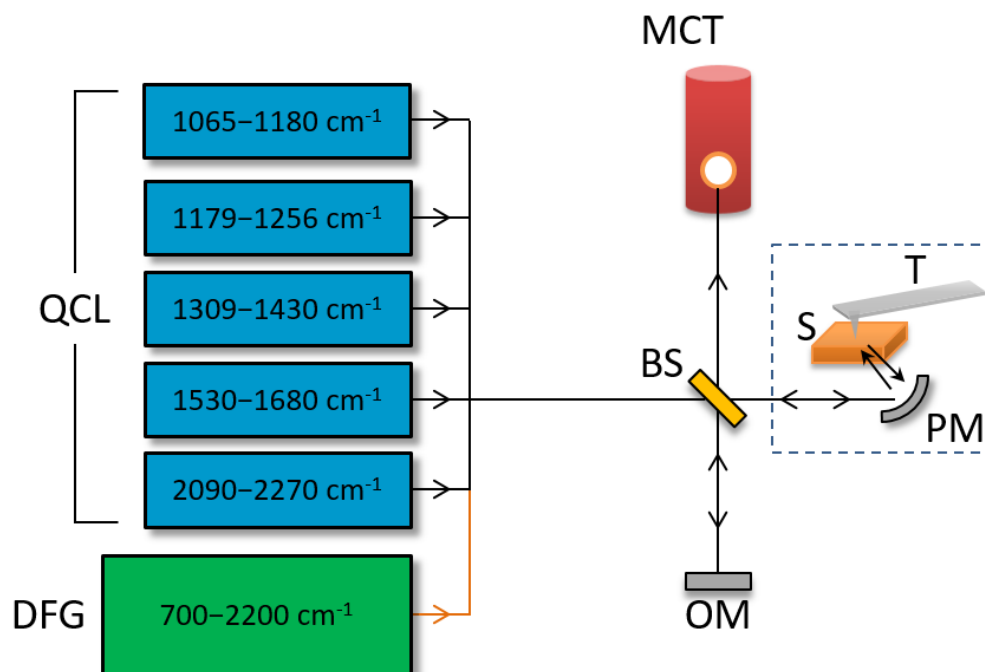


Figure 2.5: Schematics of the UCSD s-SNOM for broad-band nano-imaging and nano-FTIR experiments. Single frequency IR light (black arrows) is generated by 5 QCLs with tunable frequency indicated, in cm^{-1} . A broad-band beam (orange arrow) is generated by the DFG system with frequency range indicated. The IR beam enters an asymmetric interferometer composed of the elements: BS = ZnSe Beam Splitter, OM = Oscillating Mirror, MCT = Mercury Cadmium Telluride detector, PM = Parabolic Mirror, T = metallized Tip, S = Sample. Dashed box marks the s-SNOM part.

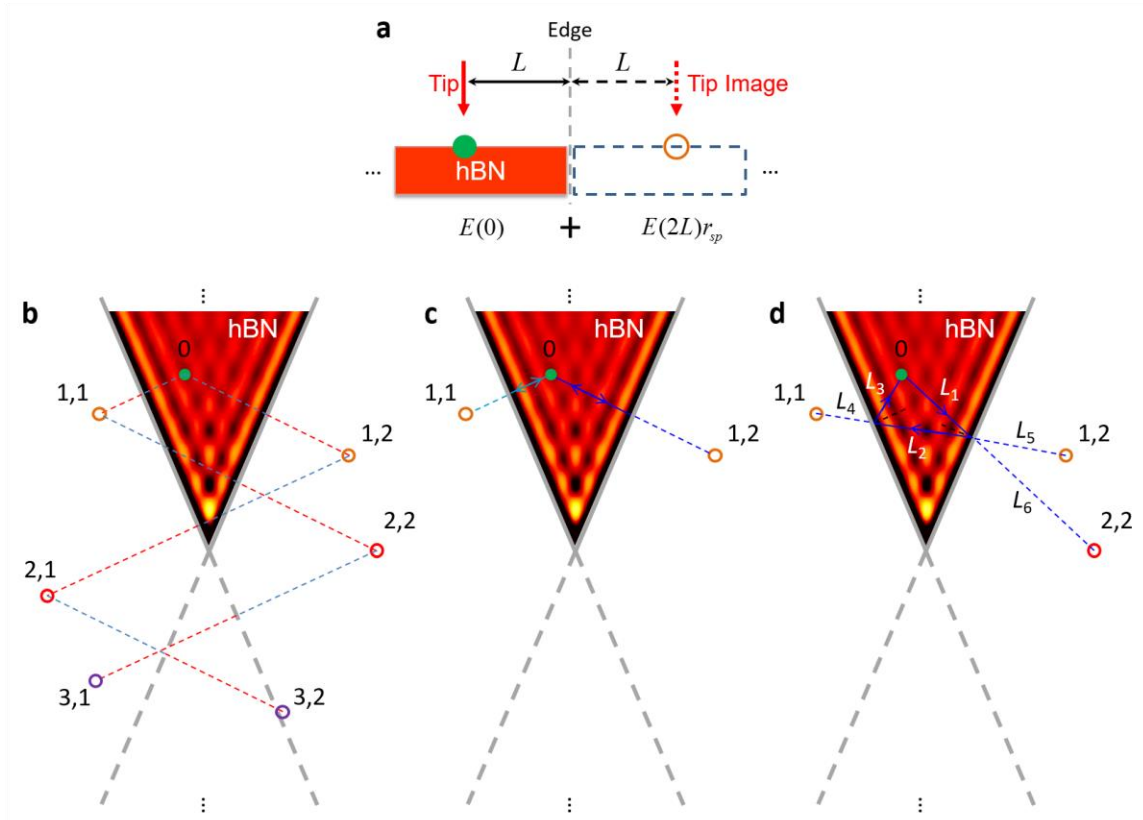


Figure 2.6: Polaritonic waves in tapered crystals. (a) Tip (solid red arrow) and its mirror image (dashed red arrow) according to the single hBN edge (grey dashed line). (b) A representative tip position (solid green dot, noted as “0”) and its images (hollow dots, labeled as “ m,n ”) for the simulation in Fig. 2.1(c). Orange, red and purple dots mark the 1-st, 2-nd and 3-rd order images of the tip, respectively. Solid grey lines track the hBN crystal’s edges; their extensions are shown with dashed lines. Red and blue dashed lines symmetrically connect the tip images with respect to the hBN edges. (c) The beam path (solid lines with arrow) of the 1-st order polariton waves. (d) The beam path (solid lines with arrow) of one representative 2-nd order polariton wave. L_1 to L_6 represent the length of each part in the solid (or dashed) blue line. Color map of (b) – (d): simulation results from Fig. 2.1(c).

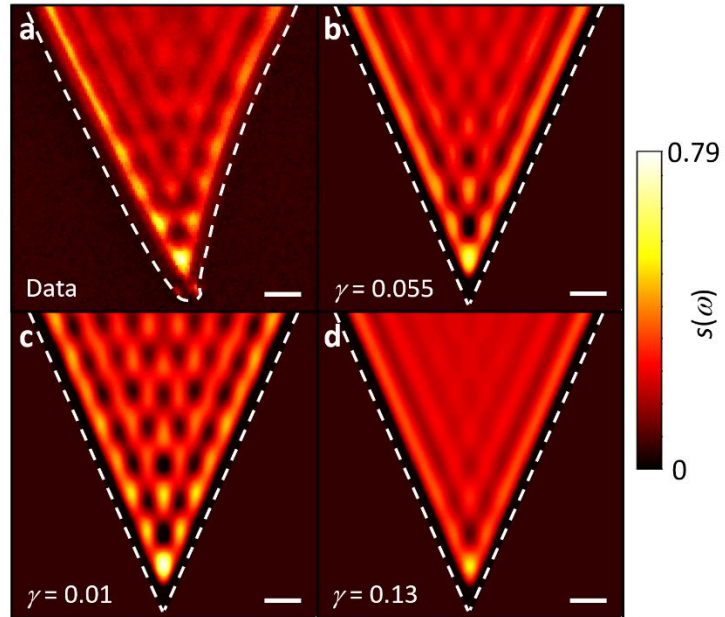


Figure 2.7: Near-field image and simulation results with different loss factors. (a) Near-field image of phonon polaritons from Fig. 2.1(b) of the main text. (b) Simulation image with the loss factor $\gamma = 0.055$ (Fig. 2.1(c)). (c) Simulation image with the loss factor $\gamma = 0.01$. (d) Simulation image with the loss factor $\gamma = 0.13$. Scale bar: 800 nm in all panels.

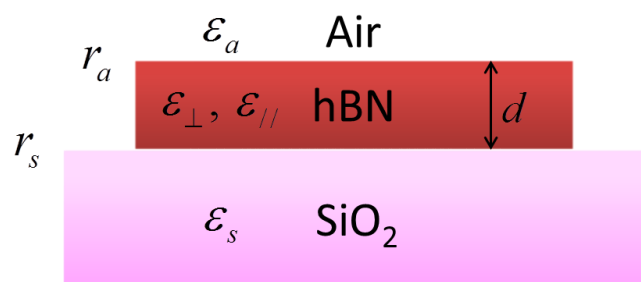


Figure 2.8: Layered structure for the Air-hBN-SiO₂ system of the dispersion model.

2.8 Bibliography

1. Dean, C.R. et al. Boron nitride substrates for high-quality graphene electronics. *Nat Nano* **5**, 722-726 (2010).
2. Novoselov, K.S. et al. Two-dimensional atomic crystals. *Proceedings of the National Academy of Sciences of the United States of America* **102**, 10451-10453 (2005).
3. Geim, A.K. & Grigorieva, I.V. Van der Waals heterostructures. *Nature* **499**, 419-425 (2013).
4. Kimura, T. & Tokura, Y. Layered Magnetic Manganites. *Annu. Rev. Mater. Sci.* **30**, 451-474 (2000).
5. Mak, K.F., Lee, C., Hone, J., Shan, J. & Heinz, T.F. Atomically Thin MoS_2 : A New Direct-Gap Semiconductor. *Physical Review Letters* **105**, 136805 (2010).
6. Splendiani, A. et al. Emerging Photoluminescence in Monolayer MoS₂. *Nano Letters* **10**, 1271-1275 (2010).
7. Qi, X.-L. & Zhang, S.-C. Topological insulators and superconductors. *Reviews of Modern Physics* **83**, 1057-1110 (2011).
8. Britnell, L. et al. Strong Light-Matter Interactions in Heterostructures of Atomically Thin Films. *Science* **340**, 1311-1314 (2013).
9. Butler, S.Z. et al. Progress, Challenges, and Opportunities in Two-Dimensional Materials Beyond Graphene. *ACS Nano* **7**, 2898-2926 (2013).
10. Novotny, L. & Hecht, B. Principles of Nano-Optics. (Cambridge University Press, Cambridge; 2006).
11. Renger, J., Grafström, S., Eng, L.M. & Hillenbrand, R. Resonant light scattering by near-field-induced phonon polaritons. *Physical Review B* **71**, 075410 (2005).
12. Shen, S., Narayanaswamy, A. & Chen, G. Surface Phonon Polaritons Mediated Energy Transfer between Nanoscale Gaps. *Nano Letters* **9**, 2909-2913 (2009).
13. Feurer, T., Vaughan, J.C. & Nelson, K.A. Spatiotemporal Coherent Control of Lattice Vibrational Waves. *Science* **299**, 374-377 (2003).
14. De Wilde, Y. et al. Thermal radiation scanning tunnelling microscopy. *Nature* **444**, 740-743 (2006).

15. Huber, A., Ocelic, N., Kazantsev, D. & Hillenbrand, R. Near-field imaging of mid-infrared surface phonon polariton propagation. *Applied Physics Letters* **87**, 081103 (2005).
16. Taubner, T., Korobkin, D., Urzhumov, Y., Shvets, G. & Hillenbrand, R. Near-Field Microscopy Through a SiC Superlens. *Science* **313**, 1595-1595 (2006).
17. Shvets, G. Photonic approach to making a material with a negative index of refraction. *Physical Review B* **67**, 035109 (2003).
18. Schuller, J.A., Zia, R., Taubner, T. & Brongersma, M.L. Dielectric Metamaterials Based on Electric and Magnetic Resonances of Silicon Carbide Particles. *Physical Review Letters* **99**, 107401 (2007).
19. Chen, J. et al. Optical nano-imaging of gate-tunable graphene plasmons. *Nature* **487**, 77-81 (2012).
20. Fei, Z. et al. Gate-tuning of graphene plasmons revealed by infrared nano-imaging. *Nature* **487**, 82-85 (2012).
21. Keilmann, F. & Amarie, S. Mid-infrared Frequency Comb Spanning an Octave Based on an Er Fiber Laser and Difference-Frequency Generation. *Journal of Infrared, Millimeter, and Terahertz Waves* **33**, 479-484 (2012).
22. Atkin, J.M., Berweger, S., Jones, A.C. & Raschke, M.B. Nano-optical imaging and spectroscopy of order, phases, and domains in complex solids. *Advances in Physics* **61**, 745-842 (2012).
23. Fei, Z. et al. Infrared Nanoscopy of Dirac Plasmons at the Graphene–SiO₂ Interface. *Nano Letters* **11**, 4701-4705 (2011).
24. Hillenbrand, R., Taubner, T. & Keilmann, F. Phonon-enhanced light-matter interaction at the nanometre scale. *Nature* **418**, 159-162 (2002).
25. Geick, R., Perry, C.H. & Rupprecht, G. Normal Modes in Hexagonal Boron Nitride. *Physical Review* **146**, 543-547 (1966).
26. Xu, X.G., Tanur, A.E. & Walker, G.C. Phase Controlled Homodyne Infrared Near-Field Microscopy and Spectroscopy Reveal Inhomogeneity within and among Individual Boron Nitride Nanotubes. *The Journal of Physical Chemistry A* **117**, 3348-3354 (2013).
27. Zhang, L.M. et al. Near-field spectroscopy of silicon dioxide thin films. *Physical Review B* **85**, 075419 (2012).

28. Poddubny, A., Iorsh, I., Belov, P. & Kivshar, Y. Hyperbolic metamaterials. *Nat Photon* **7**, 948-957 (2013).
29. Stanley, R. Plasmonics in the mid-infrared. *Nat Photon* **6**, 409-411 (2012).
30. Watanabe, K., Taniguchi, T. & Kanda, H. Direct-bandgap properties and evidence for ultraviolet lasing of hexagonal boron nitride single crystal. *Nat Mater* **3**, 404-409 (2004).
31. Gorbachev, R.V. et al. Hunting for Monolayer Boron Nitride: Optical and Raman Signatures. *Small* **7**, 465-468 (2011).
32. Golla, D. et al. Optical thickness determination of hexagonal boron nitride flakes. *Applied Physics Letters* **102**, 161906 (2013).
33. Ordin, S.V., Sharupin, B.N. & Fedorov, M.I. Normal lattice vibrations and the crystal structure of anisotropic modifications of boron nitride. *Semiconductors* **32**, 924-932 (1998).
34. Franke, E. et al. Phase and microstructure investigations of boron nitride thin films by spectroscopic ellipsometry in the visible and infrared spectral range. *Journal of Applied Physics* **82**, 2906-2911 (1997).
35. Franke, E. et al. In situ infrared and visible-light ellipsometric investigations of boron nitride thin films at elevated temperatures. *Journal of Applied Physics* **84**, 526-532 (1998).
36. Cai, Y., Zhang, L., Zeng, Q., Cheng, L. & Xu, Y. Infrared reflectance spectrum of BN calculated from first principles. *Solid State Communications* **141**, 262-266 (2007).
37. Ohba, N., Miwa, K., Nagasako, N. & Fukumoto, A. First-principles study on structural, dielectric, and dynamical properties for three BN polytypes. *Physical Review B* **63**, 115207 (2001).
38. Kuzuba, T., Era, K., Ishii, T. & Sato, T. A low frequency Raman-active vibration of hexagonal boron nitride. *Solid State Communications* **25**, 863-865 (1978).
39. Nemanich, R.J., Solin, S.A. & Martin, R.M. Light scattering study of boron nitride microcrystals. *Physical Review B* **23**, 6348-6356 (1981).
40. Lekner, J. Reflection ellipsometry of uniaxial crystals. *J. Opt. Soc. Am. A* **14**, 1359-1362 (1997).

41. Michel, K.H. & Verberck, B. Theoretical phonon dispersions in monolayers and multilayers of hexagonal boron-nitride. *physica status solidi (b)* **246**, 2802-2805 (2009).

Chapter 3

Natural hyperbolic response in hexagonal boron nitride and subdiffractive focusing

3.1 Abstract

Uniaxial materials whose axial and tangential permittivities have opposite signs are referred to as indefinite or hyperbolic media. In such materials light propagation is unusual, leading to novel and often non-intuitive optical phenomena. Here we report infrared nano-imaging experiments demonstrating that crystals of hexagonal boron nitride (hBN), a natural mid-infrared hyperbolic material, can act as a “hyper-focusing lens” and as a multi-mode waveguide. The lensing is manifested by subdiffractive focusing of phonon-polaritons launched by metallic disks underneath the hBN crystal. The waveguiding is revealed through the modal analysis of the periodic patterns observed around such

launchers and near the sample edges. Our work opens new opportunities for anisotropic layered insulators in infrared nanophotonics complementing and potentially surpassing concurrent artificial hyperbolic materials with lower losses and higher optical localization.

3.2 Introduction

One of the primary goals of nanophotonics is concentration of light on scales shorter than the free-space wavelength λ . According to the general principles of Fourier optics, this is only possible provided electromagnetic modes of large tangential momenta $k_t > \omega/(2\pi)$, normally evanescent, are nonetheless able to reach the focal plane (the x - y plane). Here $\omega = \lambda^{-1}$ is the measure of frequency common in spectroscopy and $k_t = \sqrt{k_x^2 + k_y^2}$. In devices known as superlenses [1-6], this requirement is realized via resonant tunneling between the opposite sides of the structure. However, the tunneling is very sensitive to damping, e.g., the magnitude of the imaginary part of the permittivity ϵ of the superlens material [7]. The largest characteristic momentum that can pass through a superlens of thickness d can be found from the relation $\text{Im } \epsilon \sim e^{-k_t d}$. In this regard, hyperbolic media (HM) [8, 9] promise a significant advantage as they support large- k extraordinary rays (LakERs) that remain propagating rather than evanescent, so that the condition on damping is much softer (see below). The unusual properties of LakERs in HM [8-20] stem from the dispersion of these modes that is described by the equation of a hyperboloid:

$$\varepsilon_t^{-1}k_z^2 + \varepsilon_z^{-1}(k_x^2 + k_y^2) = (2\pi\omega)^2, \quad (3.1)$$

where ε_z and $\varepsilon_t \equiv \varepsilon_x = \varepsilon_y$ are the axial and tangential permittivities, respectively. The hyperboloid is single-sheeted if $\varepsilon_z > 0$, $\varepsilon_t < 0$ (Type II) and two-sheeted if $\varepsilon_z < 0$, $\varepsilon_t > 0$ (Type I), see Figs. 3.1(a) and 3.1(b), respectively. In both cases the slope of the propagation (group velocity) direction, which is orthogonal to the dispersion surface, asymptotically approaches

$$\tan \theta(\omega) = i \frac{\sqrt{\varepsilon_t(\omega)}}{\sqrt{\varepsilon_z(\omega)}}. \quad (3.2)$$

The condition for achieving super-resolution is $\text{Im } k_z d = (k_t d) \text{Im } \tan \theta \sim 1$. Hence, admissible $\text{Im } \varepsilon_z, \text{Im } \varepsilon_t$ scale algebraically rather than exponentially with the resolution k_t^{-1} .

Directional propagation of LakERs along “resonance cones” of apex angle θ has been observed in a magnetized plasma [21, 22], which behaves as a natural HM in the microwave domain. A major resurgence of interest to HM was prompted by their discussion in the context of artificial materials (metamaterials) [23, 24]. Examples of such hyperbolic metamaterials include microstrip arrays, where directional propagation and focusing of LakERs have been experimentally observed [25, 26]. Directional optical beams have been studied in planar [25-28] and curved [12, 29] metamaterials made of alternating layers of metals and semiconductors. The work on non-planar structures [12, 29] was motivated by theoretical proposals of a Hyperlens [30-32], a device in which directional

beams outgoing from a subdiffractive source enable optical magnification. However, improvement over the diffraction limit has so far been severely impeded by losses in constituent metals and imperfections of nanofabrication.

Recent work [33, 34] identified hBN as a low-loss natural HM in the mid infrared (IR) domain. This layered insulator has emerged as a premier substrate or a spacer for van der Waals heterostructures [35, 36]. Light atomic masses, strong anisotropy, and the polar bond between B and N yield prominent optical phonon modes that create two widely separated stop-bands – spectral intervals where one of the principal values of the dielectric tensor is negative [33, 34, 37]. The upper band comprises $\omega = 1370 - 1610 \text{ cm}^{-1}$ where the real part of ϵ_t (the in-plane permittivity) is negative while that of ϵ_z is positive. In the lower band spanning $\omega = 746 - 819 \text{ cm}^{-1}$, the signs of the permittivity components are reversed. Thus, the out-of-plane crystal vibrations enable the Type I hyperbolic response, whereas the in-plane ones account for the Type II behavior. The momentum-frequency dispersion surface for the LakERs of the upper band resembles a “butterfly” (Fig. 3.1(c)) composed of individual hyperbolas sketched in Fig. 3.1(a). It can be contrasted with the flat dispersion surfaces of longitudinal phonons typical for isotropic materials. Effectively, in hBN the longitudinal phonons are hybridized with the transverse ones by quasi-static Coulomb interaction mediated by large- k photons. The phonon-polariton modes that result from this coupling are precisely the LakERs, so in the following the terms polaritons and LakERs are used synonymously.

3.3 Experimental setup

In our experiments, efficient excitation and detection of LakERs in hBN are accomplished with the help of optical antenna structures [38, 39]. The antennas concentrate electric field and bridge the large momentum mismatch between the free-space photons and the LakERs. In our previous work [33], we used for this purpose a sharp tip of an atomic force microscope (AFM) incorporated in our scattering-type scanning near-field optical microscopy (s-SNOM) apparatus (Methods). Here we additionally demonstrate the antenna and polariton-launching capabilities of Au disks patterned on a SiO₂ substrate. The AFM topography image in Fig. 3.2(a) depicts Au disks of diameters (top to bottom) 1000, 500 and 200 nm and thickness of about 50 nm. After the subsequent deposition of hBN crystals of thickness $d = 100 - 1060$ nm and lateral sizes up to 10 μ m, these Au disks become encapsulated between hBN and SiO₂. The hBN crystal remains essentially flat, as verified by AFM. Below we present experimental results demonstrating that interaction of these disks with an incident IR beam excites polaritons that travel across hBN and produce specific contrast patterns at the other surface. We show that the observed dependence of the near-field images on the frequency and hBN thickness is the result of directional propagation of the polaritons along conical surfaces with frequency-tunable apex angle given by equation (3.2). Thus, hBN may emerge as a new standard bearer for mid-IR

nanophotonics by enabling devices for deeply subdiffractive propagation, focusing, and imaging with tunable characteristics.

3.4 Experimental results

3.4.1 Subdiffractive focusing and imaging through hBN

Representative s-SNOM imaging data are shown in Fig. 3.2. Figure 3.2(b) depicts an s-SNOM scan taken at the top surface of hBN of thickness $d = 395$ nm at frequency $\omega = 1515$ cm⁻¹ ($\lambda = 6.6$ μ m). Here we plot the third harmonics of the scattering amplitude $s(\omega)$ (Methods). In this image, each Au disk is surrounded by a series of concentric “hot rings” of strongly enhanced nano-IR contrast. The diameters of all the disks are much smaller than λ (see also Fig. 3.2(a)), the smallest one being 200 nm = $\lambda/33$. The diameters of the hot rings can be larger, smaller, or equal to those of the disks. The spacing between adjacent hot rings in the same sample increases with the IR frequency but decreases with the sample thickness. We stress that images displayed in Fig. 3.2(b) could only be detected if the IR wavelength falls inside the hyperbolic spectral regions. Outside of the hBN stop bands, no hot rings can be identified by the s-SNOM. In fact, the entire image is homogeneous, comprised of nothing but random noise, as illustrated by Fig. 3.2(d) for $\omega = 1740$ cm⁻¹ ($\lambda = 5.7$ μ m).

We now elaborate on the formation of images in Fig. 3.2 recorded with our s-SNOM apparatus with the help of a model of LakERS propagation through a slab of hBN

(Figs. 3.3(a), (c) and (d)). Consider a perfectly thin metallic disk sandwiched between a slab of a HM of thickness d and an isotropic dielectric substrate. The system is subject to a uniform electric field of frequency ω and amplitude E_0 in the x -direction. An approximate solution for the total field in this system can be found analytically (Supplementary Information). The corresponding distributions of the z -component of the field $E_z(x, y, z)$ in the two cross-sections, $y = 0$ (the vertical symmetry plane) and $z = d - 0$ (just below the top surface of the hBN slab), are illustrated in Fig. 3.3(c). These plots are computed for three representative radii of the disk using permittivity values at $\omega = 1515 \text{ cm}^{-1}$. The plots demonstrate a series of concentric high-intensity rings on the top surface, very similar to the data in Fig. 3.2(b). The interpretation (Figs. 3.3(a), (c)) is straightforward: the external field polarizes the disk, which perturbs the adjacent HM (hBN in our case) and launches polaritons. The LakERs emission occurs predominantly at disk edges due to the high concentration of electric field therein. Polaritonic rays propagate across the slab, maintaining a fixed angle θ with respect to the z -axis: the “resonance cone” direction [18,21,22,25-28]. Upon reaching the other slab surface, they undergo a total internal reflection with the reflected cone extending toward the bottom surface. The process repeats until eventually the field vanishes because of radial spreading and/or damping. The role of the s-SNOM tip in imaging experiments in Fig. 3.2 is to out-couple LakERs fields at the top surface (Fig. 3.3(a)). The observed s-SNOM signal is roughly proportional to the amplitude of the electric field immediately above the slab $E_z(z = d + 0)$. (Note that it is

related to the field just inside the slab by a constant factor, $E_z(z = d + 0) = \varepsilon_z(\omega)E_z(z = d - 0)$.)

The above model of image formations via polaritonic LakERs yields a number of quantitative predictions that are in accord with our observations. The scenario of oblique propagation implies that upon each roundtrip across the slab, the excitation front returns to the same surface displaced radially by the distance

$$\delta = 2 \tan \theta(\omega) d . \quad (3.3)$$

Accordingly, the radii of the “hot rings” at the top surface of the slab are given by

$$r_n = \left| a + \left(n - \frac{1}{2} \right) |\delta| \right|, \quad n = 0, \pm 1, \pm 2, \dots \quad (3.4)$$

where a is the disk radius. The intensity of the rings is expected to decrease with $|n|$. Consistent with this formula, the smallest rings in Fig. 3c have the radius $r_0 = |a - |\delta|/2|$. Particularly interesting is the case where the innermost ring shrinks to a single bright spot, $r_0 = 0$. Experimentally, we observed spots of diameter 200 nm (the full width at half maximum, see Supplementary Information), which corresponds to $\lambda/33$ for Fig. 3.2(b) (top). Focal spots of similar size 185 – 210 nm were observed in all other hBN crystals, with the thickness up to 1050 nm (Supplementary Information).

A proposal for focusing of electromagnetic radiation via resonance-cone propagation in hyperbolic media was theoretically discussed in the context of magneto-plasmas [21]. Experimental confirmation of this idea in an artificial hyperbolic multi-layer

was reported where $\lambda/6$ focusing was deduced from examining the pattern of a polymerized photoresist behind a two-slit polaritonic launcher [26]. Here, using a natural hyperbolic slab (hBN crystal), we demonstrated the $\lambda/33$ focusing in both spatial directions via out-coupling of polaritons with the IR nano-probe. We stress that a distinction should be made between ‘focusing’ and ‘imaging.’ Focusing devices can be of both imaging and non-imaging type [40] and both are important in applications. Our hBN device (Fig. 3.3(a)) is an example of the latter.

Continuing with the verifiable predictions of our model, we note that equations (3.3) and (3.4) indicate that the slope $\tan \theta$ of the resonance cone is uniquely related to the radii of the hot rings (Fig. 3.3(a)). To test this prediction we analyzed images collected from samples of different hBN thicknesses and different Au disk diameters. For each of these, we determined the radius r_1 of the 1st-order ring and computed $|\tan \theta| = (r_1 - a)/d$ as a function of the IR frequency (Fig. 3.3(a)). As shown in Fig. 3.3(b), all the data collapse toward a single smooth curve computed from equation (2) using optical constants of hBN from ref. [33]. Yet another prediction of the model: the polaritonic rays travel along the z -axis provided that $\varepsilon_t(\omega)$ and therefore $\theta(\omega)$ are vanishingly small. This condition is satisfied at $\omega = 1610 \text{ cm}^{-1}$ (Fig. 3.2(c)) where we observe almost 1:1 images of Au disks. Similar behavior was observed when instead of the disks more complicated metallic shapes were imaged (Supplementary Information). Thus, the totality of our data establishes the

notion of directional propagation of LakERs in hBN over macroscopic distances with a frequency-tunable slope (Fig. 3.3(b)).

3.4.2 Real-space imaging of multiple guided polaritons in hBN

The outlined real-space picture has a counterpart in its conjugate momentum space. Mathematically, the resonance cones in the real space are coherent superpositions of an infinite number of polariton modes of a slab. Such modes are characterized by quantized momenta, $k_{z,l} = (\pi/d)(l + \alpha)$, labeled by integer index l [33]. Here $\alpha \sim 1$ (in general, ω -dependent) quantifies the phase shift acquired at the total internal reflection from the slab surfaces. Per equation (3.1), the tangential momenta of these modes are also quantized,

$$k_{t,l}(\omega) \simeq \cot \theta(\omega) k_{z,l}(\omega) = \frac{2\pi}{\delta(\omega)} [l + \alpha(\omega)]. \quad (3.5)$$

In the last step, we have applied equation (3.3). For illustration, the dispersion curves of such guided modes in the upper stop-band of hBN of thickness 105 nm are shown in Fig. 3.1(c), where they are overlaid on the dispersion surface of bulk hBN. The same curves are replotted as ω vs. k_t in Fig. 3.4(a). In Fig. 3.4(b) the dispersion curves of the guided modes of lower stop-band are shown. An intriguing aspect of these curves is that their slope $\partial\omega/\partial k_t$ is positive (negative) in the upper (lower) band. This sign difference is a consequence of the opposite direction of the group velocity vector for the Type I and Type II cases, cf. Fig. 3.1(a) and 3.1(b). Central to the connection between the resonance

cones in the real space and the quantized momenta in the k -space is that these momenta form an equidistant sequence of period $\Delta k_t = k_{t,l+1} - k_{t,l} = 2\pi/\delta$. Therefore, if several guided modes are excited simultaneously by a source, their superposition would produce beats with period $2\pi/\Delta k_t$ in real space. This is precisely the spacing δ between periodic revivals of the “hot rings” (equation (3.3) and Fig. 3.2). Thus, the multi-ring images and the existence of higher-order guided modes are complementary manifestations of the same fundamental physics. In our previous work [33] we reported nano-imaging and nano-spectroscopic study of the lowest-momentum guided mode $l = 0$ in hBN crystals. Below we present new results documenting the first observation of the higher-order (up to three) guided modes in such materials by direct nano-IR imaging.

In order to map the dispersion of HP^2 we utilized hBN crystals on SiO_2 substrate without any intervening metallic disks (Methods). Here the sharp tip of the s-SNOM serves as both the emitter and the detector of the polariton waves on the open surface of the hBN. As the tip is scanned toward the sample edge, distinct variations in the detected scattering amplitude $s(\omega)$ are observed. Such variations are caused by passing over minima and maxima of the standing waves created by interference of the polaritons launched by the tip and their reflections off the sample edges (Fig. 3.5(a)). Representative data for the upper stop-band (the Type II hyperbolic region) are shown in Figs. 3.5(b)-(f), where we plot $s(\omega)$ at various IR frequencies. Specifically, the image presented in Fig. 3.5(b) exhibits oscillations with the period $\sim 1\mu\text{m}$ extending parallel to the edge of a 31-nm-thick hBN

crystal. While these oscillations are similar to those reported previously [33], a high-resolution scan performed very close to the edge (the olive square) reveals additional oscillations occurring on a considerably shorter scale: down to hundreds of nm (Figs. 3.5(c)-(e)). Similar results have been obtained using many other samples. For example, Fig. 3.5(f) also shows short-scale oscillations near the edges co-existing with longer-range oscillations further away from the edge in the data collected for a thicker hBN crystal ($d = 105$ nm).

To analyze the harmonic content of the measured $s(\omega)$ quantitatively we employed the spatial Fourier transform (FT). An example shown in Fig. 3.5(h) is the FT of the line trace α from Fig. 3.5(g). The three dominant peaks in the FT are marked with β' (blue), γ' (magenta) and ζ' (olive). These peaks have been deemed statistically significant and their positions k_β , k_γ and k_ζ have been recorded for each of the traces studied. We reasoned that including additional weaker peaks into consideration may be unwarranted at this stage. Indeed, the gross features in the real-space trace α exceeding the noise level of ~ 1 a.u. are accounted for by oscillations in the three partial traces β , γ and ζ , which are obtained by the inverse FT of the shaded regions in Fig. 3.5(h).

The remaining step in the analysis is to establish the connection of thus determined momenta k_β , k_γ and k_ζ and the momenta $k_{t,l}$ of the guided modes, equation (3.5). This requires more care than in prior studies of single-mode waves in 2D materials [33,42-44]. The interference patterns near the edge can be created by various combinations of the tip-

launched waves (labeled by l) and edge-reflected waves (labeled by r). The total momentum of a particular combination is $k_{t,l} + k_{t,r}$. If the mode index is conserved, $l = r$, the set of possible periods narrows down to $2k_{t,l}$. This is consistent with our data obtained for several IR frequencies (Fig. 3.4(a)), where the symbols indicate k_β , k_γ and k_ζ . These data are in a quantitative agreement with the calculated dispersion curves for the $l = 0, 1$ and 2 polariton guided waves in the upper stop-band. The analysis of polariton propagation length [33] shows that the loss factor is as low as $\gamma \sim 0.03$ (Fig. 3.9). Dispersion mapping in the lower band ($746 - 819 \text{ cm}^{-1}$) where no monochromatic lasers are available is discussed in Figure 3.8. Broad-band lasers used in an independent study by Li et al. have allowed to demonstrate focusing behavior of hBN in this challenging frequency region [45].

3.5 Discussion

Data presented in Figs. 3.2-3.5 demonstrate launching, long-distance waveguiding transport, and focusing of electromagnetic energy in thin crystals of hBN. These phenomena are enabled by directional propagation of large-momentum polariton beams in this natural hyperbolic material. The sharpness of the attained focusing, $\lambda/33$ at distances up to $\lambda/6$ (Fig. 3.5), in units of the free-space wavelength, surpasses all prior realizations of superlenses and hyperlenses. Remarkably, a simple addition of a circular metallic launcher transforms an hBN crystal into a powerful focusing [19] device! The analysis presented in Supplementary Information (Equation 15) indicates that the size of the focal

spot in our system is limited by the finite thickness ~ 50 nm of Au disks. By using thinner disks, say 20 nm thick, one should be able to achieve focal spots as small as $\sim \lambda/10^2$, comparable to the spatial resolution of our nano-IR apparatus. A fundamental advantage of using natural rather than artificial hyperbolic materials is the magnitude of the upper momentum cutoff. In a natural material such as hBN this cutoff is ultimately set by interatomic spacing thus immensely enhancing the spatial resolution. Additionally, we have shown that hBN can serve as a multi-mode waveguide for polaritons with excellent figure of merit: loss factor as small as $\gamma \sim 0.03$. These characteristics exceed the benchmarks [46-48] of current metal-based plasmonics and metamaterials. The physics behind this fundamental advantage of phonon polaritons over plasmons in conducting media is in the absence of electronic losses in insulators. Applications of hBN for non-imaging focusing devices [41], subdiffractional waveguides, and nanoresonators [34] readily suggest themselves [45]. Combining such elements together may lead to development of sophisticated nanopolaritonic circuits.

3.6 Methods

3.6.1 Experimental setup

The nano-imaging and nano-FTIR experiments described in the main text were performed at UCSD using a commercial s-SNOM (www.neaspec.com). The s-SNOM is based on a tapping-mode AFM illuminated by monochromatic quantum cascade lasers

(QCLs) (www.daylightsolutions.com) and a broad-band laser source utilizing the difference frequency generation (DFG) (www.lasnix.com) [49]. Together, these lasers cover a frequency range of 700 – 2300 cm^{-1} in the mid-IR. The nanoscale near-field images were registered by pseudo-heterodyne interferometric detection module with AFM tapping frequency and amplitude around 250 kHz and 60 nm, respectively. To obtain the background-free images, the s-SNOM output signal used in this work is the scattering amplitude $s(\omega)$ demodulated at the n^{th} harmonics of the tapping frequency. We chose $n = 3$ in this work.

3.6.2 Sample fabrication

Silicon wafers with 300-nm-thick SiO_2 top layer were used as substrates for all samples. The Au patterns of various lateral shapes and 50-nm thickness were fabricated on these wafers by electron beam lithography. The hBN microcrystals of various thicknesses were exfoliated from bulk samples synthesized under high pressure [50]. Such microcrystals were subsequently mechanically transferred onto either patterned or unpatterned parts of the substrates.

3.7 Supplementary information

3.7.1 Theoretical model for focusing by a slab of a hyperbolic material

The problem we want to solve is computing the distribution of the electric field \vec{E} inside a hyperbolic medium (HM) slab when a metallic disk is positioned next to its surface and the entire system is subject to a uniform in-plane field \vec{E}_0 . The schematics of the model are shown in Fig. 3.6(a).

We assume that the slab with the axial permittivity $\text{Re } \varepsilon_z > 0$ and the tangential permittivity $\text{Re } \varepsilon_t < 0$ occupies the region $0 < z < d$ and refer to it as medium 1. The media above and below the slab have isotropic permittivities ε_0 and ε_2 , respectively. To simplify the analysis, we assume that the metallic disk is infinitely thin. Of course, disks used in the actual experiments are of a finite thickness. To approximately account for the finite thickness, we choose the position of the disk in the model to be some distance h away from the bottom surface of the slab, i.e., in the $z = -h$ plane, which is inside medium 2. We choose the center of the disk to reside on the z -axis. The external field \vec{E}_0 is taken to be in the x -direction.

If the disk radius a is much smaller than the free-space photon wavelength, it is sufficient to use the quasi-static approximation for the electric field,

$$\vec{E} = -\nabla\Phi_j, \quad (6)$$

where the scalar potentials Φ_j obey the following conditions. Potentials Φ_0 and Φ_2 satisfy the Laplace equation in media 0 and 2 while potential Φ_1 satisfies the equation

$$[\varepsilon_z \partial_z^2 + \varepsilon_t (\partial_x^2 + \partial_y^2)] \Phi_1 = 0 \quad (7)$$

inside the slab. The boundary conditions are: $\Phi_2 = 0$ on the disk, $\Phi_j \simeq -E_0 x$ at infinity for all j , and

$$\varepsilon_z \partial_z \Phi_1 = \varepsilon_j \partial_z \Phi_j \quad (8)$$

at the two interfaces. Although the exact analytical solution of this problem does not seem to be possible (cf. ref. [1]), an approximate one can be derived based on the solution for a metallic disk inside an *infinite* isotropic medium:

$$\phi(x, y, z) = -\frac{2}{\pi} E_0 x \left(\frac{\sinh \eta}{\cosh^2 \eta} + \arctan \sinh \eta \right), \quad (9)$$

$$\cosh \eta = \frac{1}{2a} \sqrt{(\sqrt{x^2 + y^2} + a)^2 + z^2} + \frac{1}{2a} \sqrt{(\sqrt{x^2 + y^2} - a)^2 + z^2}. \quad (10)$$

(Here the center of the disk is at the origin of the coordinate frame.) To verify that ϕ is indeed the solution, one can check that ϕ satisfies the Laplace equation, vanishes on the disk, and behaves as

$$\phi(x, y, z) \simeq -E_0 x + \frac{p_x x}{(x^2 + y^2 + z^2)^{\frac{3}{2}}}, \quad p_x = \frac{4}{3\pi} E_0 a^3 \quad (11)$$

at large distances. Quantity p_x can be recognized as the dipole moment acquired by the disk. At the disk edge potential ϕ has a square-root singularity; hence, the electric field has an inverse square-root divergence. These properties are familiar from classical electrostatics.

In order to make use of Equations (9)-(10) our first step is to generalize them for the case of an anisotropic uniaxial medium. As obvious from Equation (7), this can be achieved by rescaling of the axial coordinate: $z \rightarrow (-i \tan \theta) z$, where

$$\tan \theta = i \frac{\sqrt{\varepsilon_t}}{\sqrt{\varepsilon_z}} = \frac{\delta}{2d}, \quad \delta = 2d \tan \theta \quad (12)$$

(cf. equations (2) and (3)). If the imaginary parts of the permittivities are negligibly small, the rescaling factor is pure imaginary. This changes the nature of the solution qualitatively. It becomes possible for the arguments of the square roots to vanish not only at the edge but also at a set of points in space whose coordinates satisfy the equation

$$\sqrt{x^2 + y^2} = \pm a \pm z \tan \theta . \quad (13)$$

This set of points is a union of two cones of the opening angle $|\theta|$ coaxial with the disk and passing through its edge. The apices of the cones are located at $z = \pm a \cot \theta$. The electric field has the inverse square-root divergence on these cones, which is consistent with the physical picture of hyperbolic phonon polaritons (HP²) launched predominantly at the disk edge. Similar high field intensity cones have been previously studied in plasma physics and dubbed “resonance cones” [2]. The apices of the cones act as focal points where the rays launched at the edge intersect. At these points the singularity of the electric field is even stronger. From Equations (9)-(10) we deduce that the z -component of the electric field in the “focal plane” behaves as

$$\frac{E_z}{E_0} \propto \frac{ix}{x^2 + y^2} \quad (14)$$

if the damping is absent and there is no gap between the disk the slab, $h = 0$. This inverse-distance divergence does not have an intrinsic scale. However, one can show that if the imaginary parts of the permittivities are not neglected and/or h is nonzero, then the z -

component of the field vanishes rather than diverges at $x = y = 0$ and that it attains its maximum at positions $(\pm x_m, 0)$, where

$$x_m = \sqrt{\frac{1 + \sqrt{5}}{8}} (2h + \text{Im } \delta) , \quad (15)$$

see Fig. 6(b). Parameter x_m is one possible measure of the focal spot size. We will discuss numerical estimates of this parameter for hexagonal boron nitride (hBN) and compare them with our experimental results shortly below.

Our next step is to use Equation (9) valid for an unbounded medium as a building block for constructing a solution for the case of a finite-thickness slab. We follow the procedure standard in the method of images and consider an approximate solution as follows:

$$\begin{aligned} \Phi_1 = & - \sum_{n=1}^{\infty} r_0^n r_2^{n-1} \phi \left(x, y, -h - \frac{i\delta}{2d} z + in\delta \right) \\ & + \sum_{n=0}^{\infty} r_0^n r_2^n \phi \left(x, y, h - \frac{i\delta}{2d} z - in\delta \right) , \end{aligned} \quad (16)$$

where

$$r_j = \frac{\varepsilon_j - \sqrt{\varepsilon_z} \sqrt{\varepsilon_t}}{\varepsilon_j + \sqrt{\varepsilon_z} \sqrt{\varepsilon_t}} \quad (17)$$

is the reflection coefficient at interface of the slab and medium $j = 0, 2$. In the absence of damping in the system, these coefficients are complex numbers of unit modulus, i.e., they are phase factors. The relation of these phases to the parameter α used in Equation (10) is

$$r_0 r_2 = e^{-2\pi i \alpha}. \quad (18)$$

The top line in Equation (16) represents the scalar potential created by an infinite series of fictitious images above the slab. The sum on the bottom line contains the potential of the disk and of another infinite series of images below it. Although the complex amplitudes of the consecutive image terms, e.g., $r_0^n r_2^n$ do not decay by the absolute value, images with higher n are more distant from the slab. As a result, they produce progressively weaker potential inside the slab, which ensures convergence of the series. By construction, the potential given by Equation (16) meets the boundary conditions at the slab surfaces. The image terms modify the asymptotical value of the electric field. However, if we add the normalization factor $N = (1 - r_0 r_2)/(1 - r_0)$, we bring it back to E_0 . This way, the boundary condition at infinity will also be satisfied. Unfortunately, the potential given by Equation (16) violates the equipotential boundary condition on the disk and there is no simple way to remedy that. Similar difficulty appears in the classic electrostatic problem of a circular parallel-plate capacitor of finite radius [1]. The potential distribution in such a capacitor is not equal to the sum of the potentials created by each charged plate in isolation. However, it does look qualitatively similar. In particular, the square-root singularity at the edge is the universal feature, which must also be exhibited by the exact solution. We surmise that in our problem the main inaccuracy of Equation (16) is the strength of the square-root edge singularity. Otherwise, our approximate solution for Φ_1 should capture the qualitative aspects of the radiation cones emanating from the edges

correctly. Note that the influence of the s-SNOM tip is not considered in our theory since its effect is expected to be only quantitative, and not qualitative. As is well established in literature, the qualitative features of the near-field contrast are adequately described assuming that the near-field signal registered by the tip is proportional to the electric field just above the surface of the sample [3-6].

To get the desired electric field component E_z , we take the derivative of Φ_1 with respect to z , which we can easily do analytically. The results are plotted in the false color in Fig. 3c of the main text for different sizes of the disk. These plots depict the case $h = 0$, i.e., no gap between the disk and the slab. The optical constants used in the calculation are $\varepsilon_0 = 1$, $\varepsilon_t = -3.50 + 0.15i$, $\varepsilon_z = 2.80 + 0.0005i$, and $\varepsilon_2 = 1.39 + 0.015i$, which is appropriate for hBN slab and SiO₂ substrate at frequency $\omega = 1515 \text{ cm}^{-1}$. Using Equations (12), (17), and (18), we find $\tan \theta \approx -1.12$ and $\alpha \approx -0.23$ (both are nearly pure negative). As one can see from Fig. 3.3(c), the method of images accounts for the multiple reflections of HP^2 inside the slab that produce the concentric rings of high intensity electric field on the top surface. The rings' radii are given by Equation (4),

$$r_n = \left| a + \left(n - \frac{1}{2} \right) |\delta| \right|, \quad n = 0, \pm 1, \pm 2, \dots \quad (19)$$

(The absolute value of δ is taken in this formulas because δ can and indeed is negative in the cited example.) It is clear from the derivation that the described model has a scaling property: if a and δ are both multiplied by the same factor, the electric field as a function of dimensionless coordinates: x/a and $z/|\delta|$ does not change. Accordingly, the

qualitative aspects of the electric field distribution are controlled by the dimensionless ratio $a/|\delta|$. For example, the n -index of the smallest ring is the integer closest to $1/2 - a/|\delta|$. The evolution of the strength and relative arrangement of the hot rings is illustrated in Fig. 3b of the main text for several $a/|\delta|$ ratios and also in Fig. 3d of the main text for several θ . In all these examples the smallest ring has the radius $r_0 = \left|a - \frac{1}{2}|\delta|\right|$.

Particularly interesting is the first case where this ring shrinks to a point, $r_0 = 0$. In the other examples, sharp focal points are found inside the crystal, at the intersections of the launched and reflected resonance cones. For the quoted above values of the permittivities and the slab thickness $d = 395$ nm we get $\delta = 2 \times 395 \text{ nm} \times i\sqrt{-3.50 + 0.15i} / \sqrt{2.80} = (-880 + 19i)$ nm. Assuming also that the effective disk-slab separation is $h = 25$ nm, one half of the disk physical thickness, we get $x_m \approx 70$ nm from Equation (15). Hence, the distance between the maxima of $\text{Im } E_z$ occurring on the opposite sides of the focal spot is $2x_m \approx 140$ nm (Fig. 3.6(b)). When comparing this estimate with the focal spot size in the experimental images, such as Fig. 3.2(b), one has to keep in mind that the measured quantity is not $\text{Im } E_z$ but the demodulated scattering amplitude $s(\omega)$, which is a certain functional of E_z . Also, in the experiment the incident light has a mixture of different polarizations whereas linear polarization is assumed in the model. These are likely reasons for minor differences between the experimental images and the $\text{Im } E_z$ curves in Fig. 6(b). For example, the calculated $\text{Im } E_z$ vanishes along the line $x = 0$ but the scattering amplitude measured

in the experiment does not exactly vanish along any direction. In practice, our procedure to extract the focal spot size from the images was to take a linear cut along the direction where the signal looked like a simple peak and then take the full width at half-maximum (FWHM) of this peak (Fig. 10(b)). The above number $2x_m \approx 140$ nm gives a rough theoretical estimate of the focal spot size obtained by this procedure. It is in fact in agreement with the FWHM of 185 ~ 210 nm determined for the s-SNOM images (Figs. 3.2(b) and 3.5(b)).

To make connection with the second part of the article we use the fact that the real-space distribution of the scalar potential can be alternatively represented by a two-dimensional (2D) Fourier integral. After some lengthy but straightforward calculation, it is possible to show that Equation (16) implies that the electric field just above the top surface of the slab can be written as

$$E_z(x, y, d + 0) = 8E_0 a^3 \int \frac{dk_x}{2\pi} \int \frac{dk_y}{2\pi} e^{ik_x x + ik_y y} t(k_t) ik_x \left[\frac{\sin k_t a}{(k_t a)^3} - \frac{\cos k_t a}{(k_t a)^2} \right], \quad (20)$$

$$t(k_t) = \frac{\sin \pi \alpha}{\sin \left(\pi \alpha - \frac{1}{2} k_t \delta \right)} e^{-k_t h}, \quad k_t = \sqrt{k_x^2 + k_y^2}. \quad (21)$$

The product of the last two terms in the integrand of Equation (20) represents the amplitude of the Fourier harmonics with momentum (k_x, k_y) . The absolute values of these amplitudes exhibit slow power-law decay $\sim k_t^{-1}$. Accordingly, the Fourier spectrum of the electric field induced in our system is very broad. The inverse square-root divergence of the field at the ‘‘hot rings’’ arises from the constructive interference among the harmonics

of this broad spectrum. The dominant contribution comes from the harmonics with momenta near the discrete set of values

$$k_{t,l} = \frac{2\pi}{\delta} (l + \alpha) , \quad (22)$$

(same as Equation (5)) at which function $t(k_t)$ exhibits pole singularities. These are the momenta of the guided modes of the slab. This is why we made a statement in the main text that the image formed on the top surface of the slab can be viewed as a coherent superposition of multiple guided waves launched by the disk.

It is worth pointing out that function $t(k_t)$ has the meaning of the transmission coefficient of HP² between the metallic disk and the top surface of the slab. (More precisely, $t(k_t)$ a transmission coefficient multiplied by the momentum-independent factor N , mentioned above, that enforces the normalization $t(0) = 1$.) This transmission coefficient includes the factor $e^{-k_t h}$ due to evanescent decay across the vacuum gap and the Fabry-Pérot-like resonant transmission factor due to the free propagation of HP² inside the HM slab. If a slab were made from a non-HM, parameters δ , α , and so the guided wave momenta $k_{t,l}$ defined by Equation (22) would be predominantly imaginary. As a result, instead of the resonant transmission HP² going through the slab would suffer yet another exponential decay.

Finally, let us now discuss another interesting effect, which may perhaps be verified by future experiments. The finite thickness of real metallic disks is crudely accounted for in our model by choosing a nonzero disk-slab distance h . This parameter enters the last

exponential factor in Equation (21) thereby imposing a soft momentum cutoff $k_t \sim h^{-1}$ in the integral of Equation (20). Accordingly, the characteristic number of the guided modes that can effectively contribute to the image formation on the opposite surface of the slab becomes limited to

$$|l_{\max}| \sim \frac{|\delta|}{2\pi h}. \quad (23)$$

Therefore, as h increases, the high- l guided waves are progressively eliminated. Eventually, at $h \gg |\delta|$, the amplitude of even the lowest-momentum $l = 0$ mode becomes exponentially small. However, since the higher-order modes are suppressed even more, this mode dominates the spatial oscillations of the field. The corresponding period $2\pi/|k_{t,0}| = |\delta/\alpha|$ is in general incommensurate with and several times larger than $|\delta|$, the repeat distance of the “hot rings” at $h = 0$.

In Fig. 3.6(b) we illustrate these trends by numerical simulations of the electric field profile in the “surface-focusing” case $|a/\delta| = 0.5$ for several different h , with other parameters kept the same as in Fig. 3.3(c). We choose to plot the imaginary part of the electric field, i.e., the field component that is $\pi/2$ -out of phase with respect to the external field E_0 . (The real part, i.e., the in-phase component, shows a similar behavior.) Two facts that agree with the analytical picture are readily apparent from Fig. 3.6(b). First, at nonzero disk-slab separation the magnitude of the field can be much smaller than for disk right next to the slab. Actually, to show $h > 0$ curves clearly, we have to scale them by the factor of ten in Fig. 3.6(b). Second, as h grows, the sharply peaked extrema of the electric field

producing the equidistant series of “hot rings” separated by $|\delta|$ gradually transform into smooth sinusoidal oscillations of a larger period. This period is approximately four times $|\delta|$, in agreement with the expected result $|\delta/\alpha|$. (Recall that $\alpha \approx -0.23$ in this example.)

3.7.2 Guided wave dispersion and its thickness dependence

The thickness dependence of the $l = 0$ guided waves in hBN has been studied in our previous work [5]. Here we first summarize the procedure and then apply it to analyze the newly discovered $l \neq 0$ guided wave modes.

The momenta $k_{t,l}$ of the guided waves given by Equation (22) have been defined above as the poles of the transmission coefficient $t(k_t)$. These momenta are complex, which simply means that the guided waves exhibit finite damping. As usual, the real part of each $k_{t,l}$ determines the wavelength $\lambda_{p,l} = 2\pi / \text{Re}k_{t,l}$, while the ratio of the imaginary and real parts specifies the loss factor $\gamma = \text{Im} k_{t,l} / \text{Re} k_{t,l}$. Instead of the transmission coefficient $t(k_t)$, one can examine the surface reflectivity

$$r_p(k_t) = \frac{-r_0 + r_2 e^{i\delta k_t}}{1 - r_0 r_2 e^{i\delta k_t}} \quad (24)$$

because the poles of the two functions coincide, see Equations (18), (21), and (24).

However, the reflectivity becomes more useful for the second method of determining the mode dispersions. Namely, the imaginary part of the reflectivity as a function of real

momentum is always positive and if the loss factor is small enough, it has sharp maxima at $\text{Re } k_{t,l}$. Finding such maxima is easy to implement numerically. For the case $l = 0$, this method [7] becomes advantageous at low momenta where the quasi-static approximation becomes inaccurate and Equation (24) has to be replaced by a more complicated expression based on the full Fresnel formulas. However, higher-order modes studied here possess rather high momenta, so either method can be used.

Let us now discuss how this procedure applies specifically to the thickness dependence of the guided wave spectra in hBN. The false color plot of $\text{Im } r_p$ at a representative IR frequency $\omega = 1400 \text{ cm}^{-1}$ is shown in Fig. 3.7. It has been calculated using the permittivity functions of hBN and SiO_2 from ref. [55] and [58] as input parameters. The bright lines in this plot give $\lambda_{p,l}$. Whereas Equation (22) predicts a strictly linear dependence of $\lambda_{p,l}$ on crystal thickness d , the bright lines in Fig. 3.7 exhibit a slight curvature at small momenta. Actually, at experimentally relevant momenta the difference between the two methods of determining $\lambda_{p,l}$ is negligible. These experimental results are shown by dots and triangles in Fig. 3.7(a). They have been found using the Fourier-transform method described in the main text. The measurements were done on several different hBN specimens. The thickness d for each of the specimen was measured via the AFM topography simultaneously with the IR images. Matching the symbols with the nearby lines makes it possible to identify the modes as $l = 1$ for the dots and $l = 2$ for the triangles. Within the shown range of d , the measured wavelengths of these modes scale

linearly with the hBN thickness, in accord with the theory. Figure 7(b) shows another set of results for the frequency $\omega = 790 \text{ cm}^{-1}$, which belongs to the lower stop-band (Type I region). Here the polaritons have a negative group velocity but they obey the same linear scaling with d as in the upper band, which is again in agreement with the theory.

3.8 Acknowledgements

This work is supported by DOE-BES, AFOSR, NASA, Gordon and Betty Moore Foundation and University of California Office of the President.

Chapter 3, in full, is a reprint of the material as it appears in S. Dai, Q. Ma, T. Andersen, A. S. McLeod, Z. Fei, M. K. Liu, M. Wagner, K. Watanabe, T. Taniguchi, M. Thiemens, F. Keilmann, P. Jarillo-Herrero, M. M. Fogler & D. N. Basov. “Subdiffractional focusing and guiding of polaritonic rays in a natural hyperbolic material”. *Nature Comm.* 6, 6963 (2015). The dissertation author was the primary investigator and author of this paper.

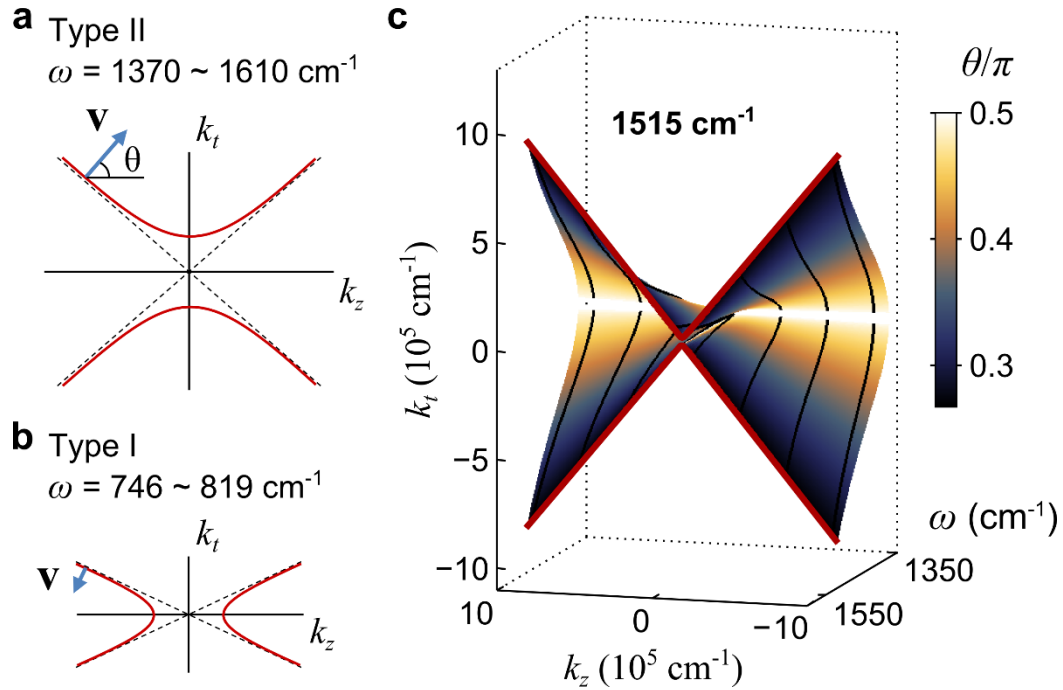


Figure 3.1: Hyperbolic dispersion of hBN. (a), A sketch of the isofrequency curves for a Type II HM, which is realized in the upper stop-band of hBN. The arrow indicates the polariton group velocity. (b), A similar sketch for the Type I case, which is realized in the hBN lower stop-band. (c), The calculated dispersion surface of hBN polaritons. The axes are the tangential momentum (k_t), the axial momentum (k_z), and the frequency (ω , ranging from 1370 to 1515 cm^{-1}). The color represents the propagation angle θ . The constant-frequency cut $\omega = 1515 \text{ cm}^{-1}$ is shown by the red line, to emphasize similarity with (a). The dispersion of polaritons in a finite-thickness crystal ($d = 105 \text{ nm}$) is shown by the black lines, to clarify their relation to (d). (d), The dispersion curves from the previous panel replotted as in-plane momenta (k_t) vs. frequency (ω). The symbols are derived from the polariton reflection images near the sample edges (Fig. 3.4). (e), Same as (d) for the lower hBN stop-band (Fig. 3.7).

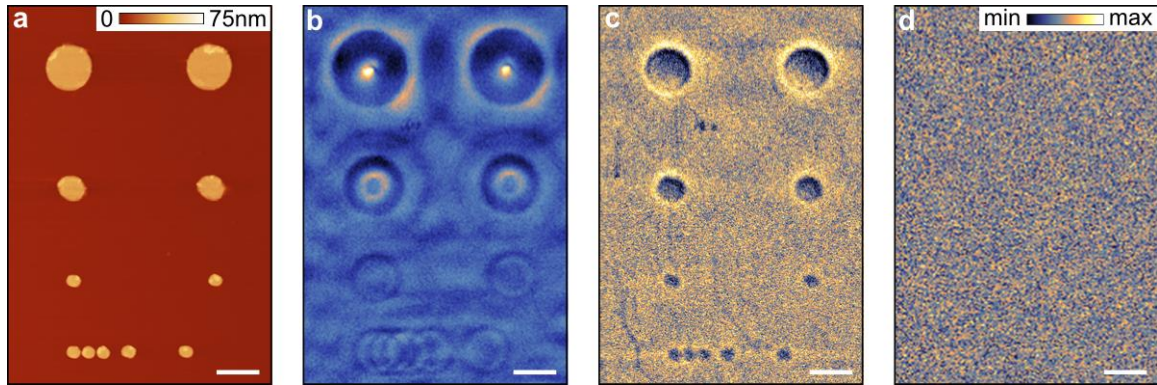


Figure 3.2: Sub-diffractive focusing and imaging through an hBN crystal. (a), An AFM image of Au disks defined lithographically on SiO₂/Si substrate before hBN transfer. (b), Near-field amplitude image of the top surface of a 395-nm-thick hBN at IR laser frequency $\omega = 1515 \text{ cm}^{-1}$ ($\lambda = 6.6 \text{ }\mu\text{m}$). The observed “hot rings” are concentric with the Au discs. (c), Near-field image of the same sample as in panel (b) at $\omega = 1610 \text{ cm}^{-1}$ ($\lambda = 6.2 \text{ }\mu\text{m}$) where polaritons propagate almost vertically. (d), Near-field image of the same sample at $\omega = 1740 \text{ cm}^{-1}$ ($\lambda = 5.7 \text{ }\mu\text{m}$) showing complete homogeneity and lack of any distinct features. The color scales for (b) – (d) are indicated in (d). The scale bars in all panels are 1 μm long.

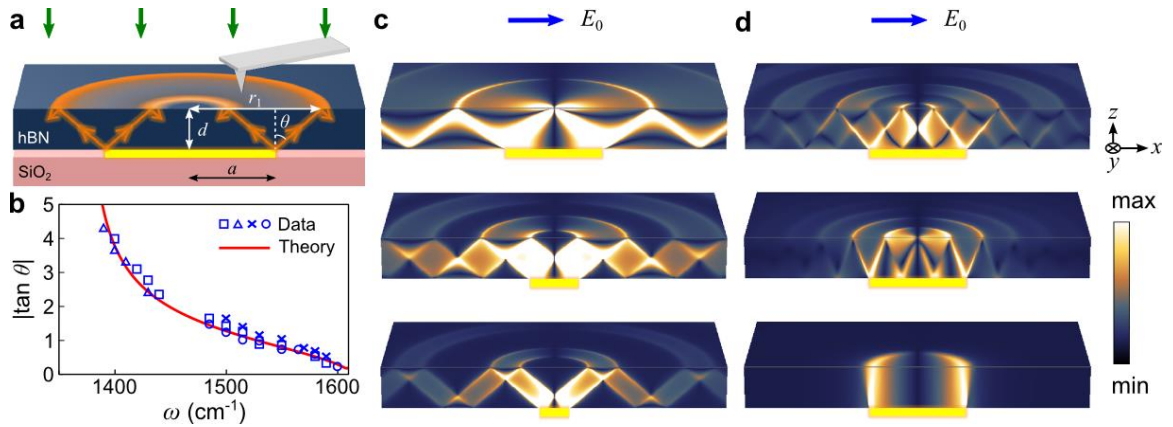


Figure 3.3: The image formation. (a), Imaging schematics. Under IR illumination (green arrow), the polaritons were launched by the Au disk edges and propagate towards the hBN top surface where the near-field images were recorded via the back-scattered IR beam (green arrow). The propagation angle θ can be inferred from the hot ring radius r_1 , hBN thickness d , and disk radius a . (b), The tangent of the propagation angle θ derived from imaging data for different hBN samples (symbols) and from equation (3.2) (solid line). “□”, “Δ”, “×” and “○” indicate data from hBN samples with thickness $d = 395, 984, 270$ and 1060 nm, respectively. (c), The distribution of the z -component of the electric field in the analytical model (see text). The hot rings on the surfaces appear as a result of multiple reflections of polaritons launched at the disk edges. The ratio $a/|\delta| = 0.5, 0.25, 0.15$ decreases from top to bottom. In the top picture the smallest ring shrinks to a focal point. The blue arrow indicates the direction of electric field E_0 in simulation. (d), Similar to panel (b) for $a/d = 1.12$ and (top to bottom) $|\tan \theta| = 0.75, 0.375$ and 0.01 .

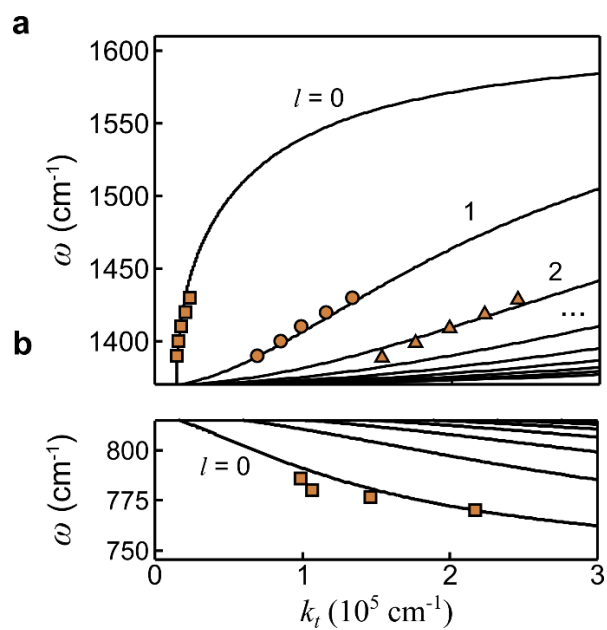


Figure 3.4: Polariton frequency (ω) – in-plane momentum (k_t) dispersion relation for hBN. (a), The dispersion curves from Fig. 3.1(c) replotted as frequency (ω) vs. in-plane momenta (k_t). The experimental data (squares) are obtained from the s-SNOM images near the sample edges (Fig. 3.5). (b), Same as (a) for the lower hBN stop-band (Supplementary Figure 3.3). Thickness of hBN: 105 nm.

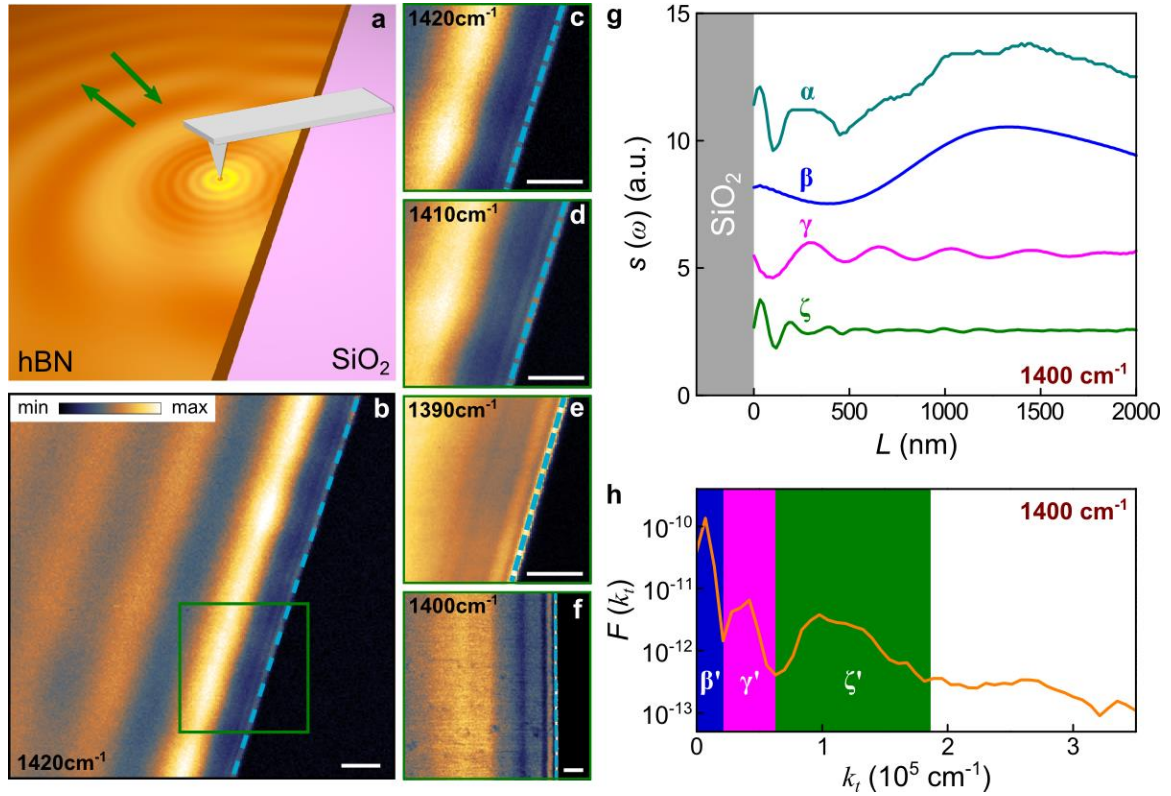


Figure 3.5: Imaging of polariton waveguide modes near the hBN edges. (a), Experimental schematic is similar to Fig. 3.3(a) except imaging here is performed near the edge of an unpatterned sample. (b), Near-field amplitude image measured at 1420 cm^{-1} . The olive square indicates the area whose expanded view is shown in (c)-(e). (c)-(e), Near-field image of the area marked in (b) at several frequencies. hBN thickness in (b)-(e): 31 nm . (f), Near-field image of 105-nm -thick hBN at 1400 cm^{-1} . The cyan dashed lines in (b)-(f) indicate the hBN edges. Scale bar in (b)-(f): 300 nm . (g), Line traces perpendicular to the hBN edge. Trace α was extracted from the image in panel (f). Traces β , γ and ζ were obtained from the Fourier analysis of the trace α as described in the text. (h): The Fourier transform of trace α in panel (g).

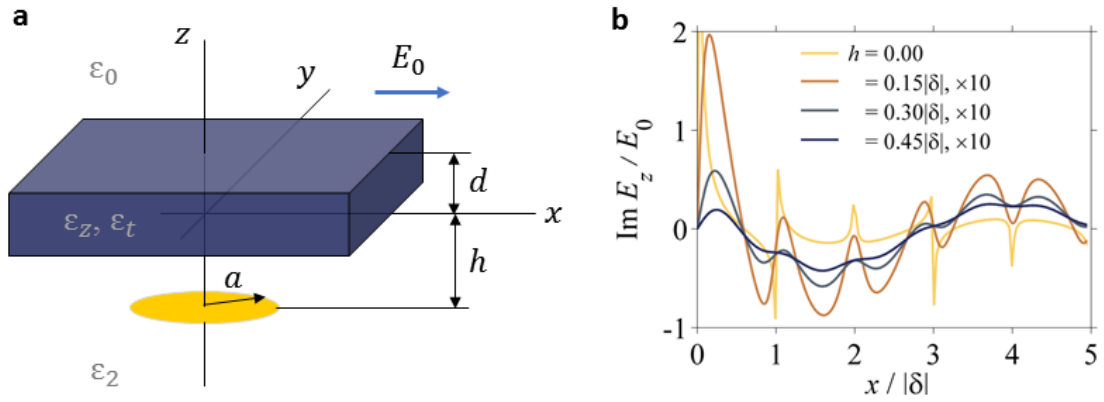


Figure 3.6: Theoretical model and the electric field profile it predicts. (a), The schematics of the model. (b), The imaginary part of the z -component of the electric field just below the top surface of the slab along the $x > 0$ semi-axis for fixed $a = d = 0.5\delta$ and different h/δ (higher h corresponds to smoother curves; the vertical scale of last three is magnified tenfold.)

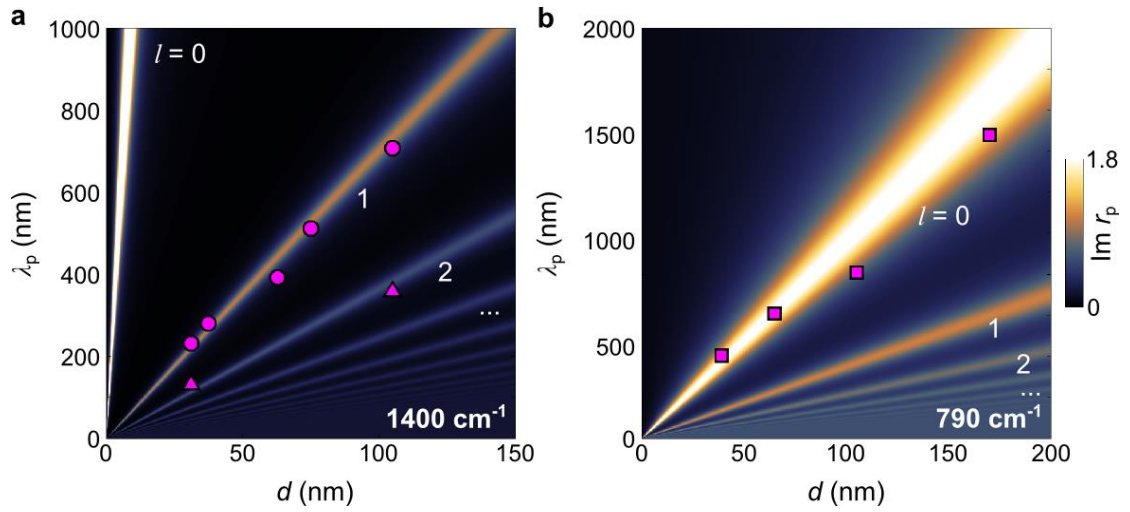


Figure 3.7: Thickness dependence of the guided wave dispersion. (a), The false color plot of the imaginary part of the reflectivity at frequency 1400 cm^{-1} inside the upper (Type II) stop-band of hBN. Experimental data for $l=1$ and 2 modes are shown by dots and triangles. (b), A similar plot for frequency 790 cm^{-1} , which is inside the lower (Type I) stop-band. Here only $l=0$ mode has been detected.

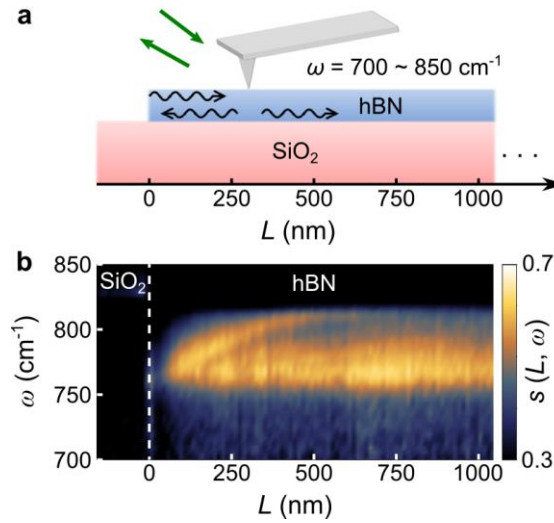


Figure 3.8: Nano-FTIR study of guided waves in the lower stop-band (Type I spectral region, $\omega = 746 - 819 \text{ cm}^{-1}$). Since no monochromatic lasers are available in this spectral region, the measurements in the lower stop-band were performed by means of the Fourier transform IR nano-spectroscopy (nano-FTIR) technique [55]. (a), Schematic of the experiment. A line scan starts from a region of unobscured SiO_2 substrate ($L < 0$) and extends in the region where the hBN crystal resides on SiO_2 ($L > 0$). The green arrows indicate incident and back-scattered broadband IR beam. The black arrows represent the polariton guided waves launched by the tip and reflected by the $L = 0$ edge. (b), We took near-field spectra at every pixel along the scanning line (a) and then obtained the 2D scattering amplitude map $s(L, \omega)$ for a 105-nm-thick hBN crystal on the SiO_2 substrate. The spectra are normalized to Au reference. The dashed line indicates the edge of the crystal. At the hBN side, this map shows the characteristic maxima (interference fringes) created by polariton resonances. The distance of the fringes from the edge increases with the IR frequency ω . This trend is exactly opposite to what we observe in the Type II hyperbolic spectral region, $1350 - 1550 \text{ cm}^{-1}$ (see Figs. 3.4 and 3.5 and ref. [55]). It implies that the group velocity of the guided waves in the lower stop-band is negative, in accord with its designation as the Type I hyperbolic region. The data points (squares in Fig. 3.4(b)) extracted from $\omega = \text{constant}$ in this panel, are in a good agreement with the calculated dispersion of $l = 0$ mode (solid line in Fig. 3.4).

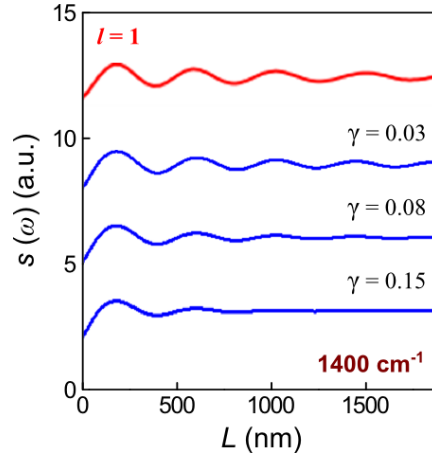


Figure 3.9: Estimates of the loss factor. To estimate the loss factor from the imaging data shown in from Fig. 3.5(g), we carried out simulations of the damped sinusoidal line traces with different trial loss factors γ following ref. [55]. From these simulations, we concluded that the loss factor for the $l = 1$ mode in Fig. 3.5(g) is roughly $\gamma \sim 0.03$. Red trace: contribution of the $l = 1$ guided wave to the measured scattering amplitude at $\omega = 1400 \text{ cm}^{-1}$ (same as the γ trace in Fig. 3.5(g)). Blue traces: results of the simulation done following ref. [55] for trial loss factors $\gamma = 0.03, 0.08,$ and 0.15 .

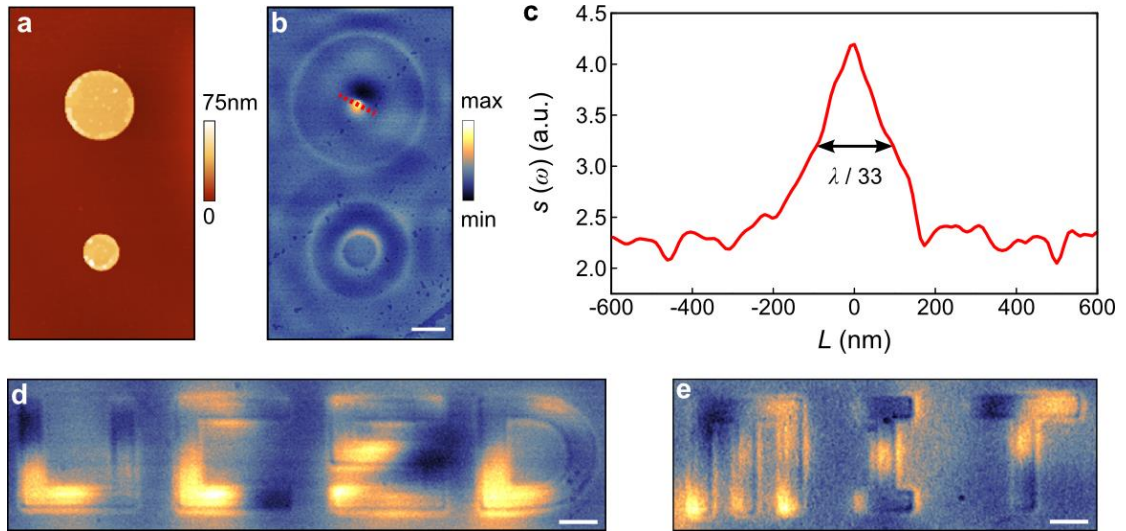


Figure 3.10: Supplementary s-SNOM images. We achieved small focal spots (FWHM: 185 ~ 210 nm) in all our devices with hBN thickness up to 1050nm. (a), The AFM image of Au disks of diameter 1 μm (top) and 2 μm (bottom) on SiO₂/Si substrate before the hBN transfer. (b), Near-field amplitude image obtained on the top surface of a 1050-nm-thick hBN slab after transferred on (a). IR frequency: $\omega = 1541 \text{ cm}^{-1}$. Remarkably, this device gives a $\lambda/33$ focal spot with a focal distance of $\lambda/6$ (1050 nm, hBN thickness). (c), Line profile of taken along the red dotted line in (b). The black double-arrow indicates the FWHM measured as the focal spot size. In addition to the Au disks, we have prepared and imaged samples with more complicated shapes, for example, in the form of nano-lettered logos of our research institutions (d) and (e) at $\omega = 1610 \text{ cm}^{-1}$. We also see an approximately 1:1 copy of the pattern underneath hBN, in agreement with the theoretical picture of the directional propagation of the polariton rays almost normal to the surface, Fig. 3.3(d) (bottom) of the main text. Interestingly, some parts of the image have higher intensity than others. The origin of these intensity variations may be studied in future experiments. Scale bar: 1 μm .

3.9 Bibliography

1. Pendry, J. B. Negative refraction makes a perfect lens. *Phys. Rev. Lett.* **85**, 3966-3969 (2000).
2. Fang, N., Lee, H., Sun, C. & Zhang, X., Sub-Diffraction-Limited Optical Imaging with a Silver Superlens. *Science* **308**, 534-537 (2005).
3. Taubner, T., Korobkin, D., Urzhumov, Y., Shvets, G. & Hillenbrand, R. Near-field microscopy through a SiC superlens. *Science* **313**, 1595 (2006).
4. Zhang, X. & Liu, Z. Superlenses to overcome the diffraction limit. *Nature Mater.* **7**, 435-441 (2008).
5. Smolyaninov, I. I., Hung, Y. J., Davis, C. C. Magnifying Superlens in the Visible Frequency Range. *Science* **315**, 1699-1701 (2007).
6. Kehr, S. C. et al. Near-field examination of perovskite-based superlenses and superlens-enhanced probe-object coupling. *Nature Commun.* **2**, 249 (2011).
7. Smith, D. R., Schurig, D., Rosenbluth, M., Schultz, S., Ramakrishna, S. A. & Pendry, J. B. Limitations on subdiffraction imaging with a negative refractive index slab. *Appl. Phys. Lett.* **82**, 1506-1508 (2003).
8. Poddubny, A., Iorsh, I., Belov, P. & Kivshar, Y. Hyperbolic metamaterials. *Nature Photon.* **7**, 948-957 (2013).
9. Guo, Y., Newman, W., Cortes, C. L. & Jacob, Z. Applications of hyperbolic metamaterial substrates. *Advances in OptoElectronics* **2012**, 452502 (2012).
10. Hoffman, A. J. et al. Negative refraction in semiconductor metamaterials. *Nature Mater.* **6**, 946-950 (2007).
11. Yao, J. et al. Optical negative refraction in bulk metamaterials of nanowires. *Science* **321**, 930 (2008).
12. Liu, Z., Lee, H., Xiong, Y., Sun, C. & Zhang, X. Far-field optical hyperlens magnifying sub-diffraction-limited objects. *Science* **315**, 1686 (2007).

13. Yang, X., Yao, J., Rho, J., Yin, X. & Zhang, X. Experimental realization of three-dimensional indefinite cavities at the nanoscale with anomalous scaling laws, *Nature Photon.* **6**, 450-454 (2012).
14. Argyropoulos, C., Estakhri, N. M., Monticone, F. & Alu, A. Negative refraction, gain and nonlinear effects in hyperbolic metamaterials. *Opt. Express* **21**, 15037-15047 (2013).
15. Biehs, S. A., Tschikin, M. & Ben-Abdallah, P. Hyperbolic metamaterials as an analog of a blackbody in the near field. *Phys. Rev. Lett.* **109**, 104301 (2012).
16. Noginov, M. A. et al. Controlling spontaneous emission with metamaterials. *Opt. Lett.* **35**, 1863-1865 (2010).
17. Guo, Y., Cortes, C. L., Molesky, S. & Jacob, Z. Broadband super-Planckian thermal emission from hyperbolic metamaterials. *Appl. Phys. Lett.* **101**, 131106 (2012).
18. Jacob, Z., Smolyaninov, I. I. & Narimanov, E. E. Broadband Purcell effect: Radiative decay engineering with metamaterials. *Appl. Phys. Lett.* **100**, 181105 (2012).
19. Smith, D. R., Schurig, D., Mock, J. J., Kolinko, P. & Rye, P. Partial focusing of radiation by a slab of indefinite media. *Appl. Phys. Lett.* **84**, 2244-2246 (2004).
20. Vinogradov, A. P., Dorofeenko, A. V. & Nechepurenko, I. A. Analysis of plasmonic Bloch waves and band structures of 1D plasmonic photonic crystals. *Metamaterials* **4**, 181-200 (2010).
21. Fisher, R. K. & Gould, R. W. Resonance cones in the field pattern of a short antenna in anisotropic plasma. *Phys. Rev. Lett.* **22**, 1093-1095 (1969).
22. Levine, B., Greene, G. J. & Gould, R. W. Focusing resonance cones. *Phys. Fluids* **21**, 1116 -1119 (1978).
23. Lindell, I. V., Tretyakov, S. A., Nikoskinen, K. I. & Ilvonen, S. BW media-media with negative parameters, capable of supporting backward waves. *Microw. Opt. Technol. Lett.* **31**, 129-133 (2001).
24. Smith, D. R. & Schurig, D. Electromagnetic Wave Propagation in Media with Indefinite Permittivity and Permeability Tensors. *Phys. Rev. Lett.* **90**, 077405 (2003).

25. Siddiqui, O. & Eleftheriades, G. V. Resonance-cone focusing in a compensating bilayer of continuous hyperbolic microstrip grids. *Appl. Phys. Lett.* **85**, 1292 (2004).
26. Ishii, S., Kildishev, A. V., Narimanov, E., Shalaev, V. M. & Drachev, V. P. Sub-wavelength interference pattern from volume plasmon polaritons in a hyperbolic medium, *Laser Photonics Rev.* **7**, 265-271 (2013).
27. Thongrattanasiri, S. & Podolskiy, V. A. Hypergratings: nanophotonics in planar anisotropic metamaterials. *Opt. Lett.* **34**, 890-892 (2009).
28. Ishii, S., Drachev, V. P. & Kildishev, A. V. Diffractive nanoslit lenses for subwavelength focusing. *Opt. Commun.* **285**, 3368-3372 (2012).
29. Rho, J., Ye, Z., Xiong, Y., Yin, X., Liu, Z., Choi, H., Bartal, G. & Zhang, X. Spherical hyperlens for two-dimensional sub-diffractive imaging at visible frequencies. *Nature Commun.* **1**, 143 (2010).
30. Jacob, Z., Alekseyev, L. V. & Narimanov, E. Optical Hyperlens: Far-field imaging beyond the diffraction limit. *Opt. Express* **14**, 8247-8256 (2006).
31. Salandrino, A. & Engheta, N., Far-field subdiffraction optical microscopy using metamaterial crystals: Theory and simulations, *Phys. Rev. B* **74**, 075103 (2006).
32. Lu, D. & Liu, Z. Hyperlenses and metalenses for far-field super-resolution imaging. *Nature Commun.* **3**, 1205 (2012).
33. Dai, S. et al. Tunable phonon polaritons in atomically thin van der waals crystal of boron nitride. *Science* **343**, 1125-1129 (2014).
34. Caldwell, J. D. et al. Sub-diffraction, Volume-confined Polaritons in the Natural Hyperbolic Material, Hexagonal Boron Nitride, *Nature Commun.* **5**, 5221 (2014).
35. Geim, A. K., & Grigorieva, I. V. Van der Waals heterostructures. *Nature* **499**, 419-425 (2013).
36. Fogler, M. M., Butov, L. V. & Novoselov, K. S., High-temperature super-fluidity with indirect excitons in van der Waals heterostructures, *Nature Commun.* **5**, 4555 (2014).
37. Xu, X. G. et al. One-dimensional surface phonon polaritons in boron nitride nanotubes. *Nature Commun.* **5**, 4782 (2014).

38. Tarkhanyan, R. & Uzunoglu, N., *Radiowaves and Polaritons in Anisotropic Media: Uniaxial Semiconductors* (Wiley, Hoboken, 2006).
39. Novotny, L. & Hecht, B. *Principles Of Nano-Optics* (Cambridge University Press, Cambridge, 2006).
40. Atkin, J. M., Berweger, S., Jones, A. C. & Raschke, M. B. Nano-optical imaging and spectroscopy of order, phases, and domains in complex solids. *Adv. Phys.* **61**, 745-842 (2012).
41. Chaves, J. *Introduction to Nonimaging Optics* (CRC Press, Boca Raton, FL, 2008).
42. Chen, J. et al. Optical nano-imaging of gate-tunable graphene plasmons. *Nature* **487**, 77-81 (2012).
43. Fei, Z. et al. Gate-tuning of graphene plasmons revealed by infrared nano-imaging. *Nature* **487**, 82-85 (2012).
44. Woessner, A. et al. Highly confined low-loss plasmons in graphene-boron nitride heterostructures. *Nature Mater.* **14**, 421-425 (2015).
45. Li, P. et al. Hyperbolic Phonon-polaritons in Boron Nitride for near-field optical imaging. *Nature Commun.* **6**, 7507 (2015).
46. Boltasseva, A., Atwater, H. Low-loss Plasmonic Metamaterials. *Science* **331**, 290-291 (2011).
47. Tassin, P., Koschny, T., Kafesaki, M. & Soukoulis, C. A comparison of graphene, superconductors and metals as conductors for metamaterials and plasmonics. *Nat. Photon.* **6**, 259-264 (2012).
48. Khurgin, J. B. & Boltasseva, A. Reflecting upon the losses in plasmonics and metamaterials. *MRS Bull.* **37**, 768-779 (2012).
49. Keilmann, F. & Amarie, S. Mid-infrared frequency comb spanning an octave based on an Er fiber laser and difference-frequency generation. *J. Infrared Millimeter Terahertz Waves* **33**, 479-484 (2012).

50. Watanabe, K., Taniguchi, T. & Kanda, H. Direct-bandgap properties and evidence for ultraviolet lasing of hexagonal boron nitride single crystal. *Nature Mater.* **3**, 404-409 (2004).
51. Chew, W. C. & Kong, J. A., Microstrip Capacitance for a Circular Disk Through Matched Asymptotic Expansions, *SIAM J. Appl. Math.* **42**, 302–317 (1982).
52. Fisher, R. K. & Gould, R. W. Resonance cones in the field pattern of a short antenna in anisotropic plasma. *Phys. Rev. Lett.* **22**, 1093-1095 (1969).
53. Huber, A., Ocelic, N., Kazantsev, D. & Hillenbrand, R. Near-field imaging of mid-infrared surface phonon polariton propagation. *Appl. Phys. Lett.* **87**, 081103 (2005).
54. Huber, A. J., Deutsch, B., Novotny, L. & Hillenbrand, R. Focusing of surface phonon polaritons. *Appl. Phys. Lett.* **87**, 081103 (2005).
55. Dai, S. *et al.* Tunable phonon polaritons in atomically thin van der Waals crystal of boron nitride. *Science* **343**, 1125-1129 (2014).
56. Alonso-González, P. *et al.* Controlling graphene plasmons with resonant metal antennas and spatial conductivity patterns. *Science* **344**, 1369 (2014).
57. Zhang, L. M. *et al.*, Near-field spectroscopy of silicon dioxide thin films. *Phys. Rev. B* **85**, 075419 (2012).
58. Cai, Y., Zhang, L., Zeng, Q., Cheng, L. & Xu, Y., Infrared reflectance spectrum of BN calculated from first principles. *Solid State Commun.* **141**, 262 (2007).

Chapter 4

Tunable hyperbolic metamaterial based on graphene/hexagonal boron nitride heterostructure

4.1 Abstract

Hexagonal boron nitride (h-BN) is a natural hyperbolic material [1], for which the dielectric constants are the same in the basal plane ($\epsilon^t \equiv \epsilon^x = \epsilon^y$) but have opposite signs ($\epsilon^t \epsilon^z < 0$) from that in the normal plane (ϵ^z) [1-4]. Due to this property, finite-thickness slabs of h-BN act as multimode waveguides for propagating hyperbolic phonon polaritons (HPhP, or HP²) [1,2,5] – collective modes originated from the coupling between photons and electric dipoles [6] in phonons. However, control of these HP² modes has remained challenging, mostly because their electrodynamic properties are dictated by the crystal lattice of h-BN [1,2,7]. Here we show by direct nano-infrared (nano-IR) imaging that these hyperbolic polaritons can be effectively modulated in a van der Waals (vdW)

heterostructure [8] composed of monolayer graphene on h-BN. Tunability originates from the hybridization of surface plasmon polaritons (SPP, or SP^2) in graphene [9-13] with HP^2 in h-BN [1,2], so that the eigenmodes of the graphene/h-BN heterostructure are hyperbolic plasmon-phonon polaritons (HP^3). Remarkably, the HP^3 in graphene/h-BN suffer little from ohmic losses; In fact, their propagation length is 1.5-2.0 times greater than that of HP^2 in h-BN. The HP^3 possesses the combined virtues of SP^2 in graphene and HP^2 in h-BN. Therefore, graphene/h-BN structures can be classified as electromagnetic metamaterials [14] since the resulting properties of these devices are not present in its constituent elements.

4.2 Introduction

Van der Waals heterostructures assembled from (one or few) monolayers of graphene, h-BN, MoS_2 and other atomic crystals in various combinations are emerging as a new paradigm to attain the desired electronic [8,15] and optical [16] properties. These heterostructures are also of interest in the context of polaritons that are ubiquitous in metals, insulators and semiconductors [6,16]. At least two different classes of propagating polaritons are firmly established in vdW systems: SP^2 in graphene [9-13] and HP^2 in h-BN [1,2]. In graphene/h-BN meta-structures, coherent oscillations of the electron density in graphene and the atomic vibrations in h-BN produce hybridized plasmon-phonon modes. Surface plasmon-phonon modes [17] and related energy transfer processes [18] have been investigated in structures comprised of graphene with monolayer h-BN or a BN nanotube. However, neither monolayers [17] nor nanotubes [18] of BN support hyperbolic response:

an exquisite attribute of three-dimensional specimens of this layered anisotropic material [1-4]. A remarkable feature of graphene/h-BN heterostructures uncovered in our experiments is that monolayer graphene impacts the hyperbolic response of h-BN slabs as thick as 99 nm, exceeding 300 atomic layers. We demonstrate that both the wavelength and intensity of hyperbolic polaritons can be controlled via electrostatic gating of the top graphene layer.

4.3 Experimental results

Direct experimental access to the tunable hyperbolic response in graphene/h-BN is provided by IR nano-spectroscopy and nano-imaging via a scattering-type scanning near-field optical microscope (s-SNOM) as shown in Fig. 4.1(a) (see also Methods). The same technique was utilized in a recent study [19] of h-BN/graphene/h-BN vdW heterostructures; however, the hyperbolic spectral regions were not probed therein. In Fig. 4.1(b) we show broad-band nano-IR spectra of the normalized (Methods) scattering amplitude $s(\omega)$ as a function of frequency $\omega = 1 / \lambda_{\text{IR}}$, λ_{IR} being the IR wavelength, for h-BN, SiO₂ substrate, and graphene/h-BN meta-structures. The spectra for SiO₂ (black) and h-BN (red) display resonances due to their mid-IR phonons [1,20]. The two hyperbolic regions of h-BN [1,2] are highlighted in Fig. 4.1(b). Type I region where $\varepsilon^z < 0$, $\varepsilon^t > 0$ extends over the frequency range $\omega = 746 - 819 \text{ cm}^{-1}$. Type II region where $\varepsilon^z > 0$, $\varepsilon^t < 0$ spans the range $\omega = 1370 - 1610 \text{ cm}^{-1}$. Both type I and II resonances of h-BN are modified in meta-structures incorporating monolayer graphene (the blue spectrum in Fig. 4.1(b)). The impact of graphene is particularly prominent in the type I region where the resonance mode is

significantly enhanced and blue-shifted by nearly $\sim 25 \text{ cm}^{-1}$ compared to the response of a standalone h-BN slab.

The peculiar electrodynamics of graphene/h-BN is vividly illustrated by the calculated frequency (ω) – momentum (q) dispersion relations of its polariton modes (Figs. 4.1(c)-(e), see Supplementary Information for details). Following Ref. [6], we visualize these dispersions using a false colour map of the imaginary part of the reflectivity r_p . It is instructive to first consider the polaritons of the two constituent elements (graphene and h-BN) separately. In Fig. 4.1(c) we plot the dispersion of SP² for a freestanding graphene layer for three selected values of the Fermi energy E_F . These parabolic curves are described by the equation [21] $q_p(\omega) = \frac{(\hbar\omega)^2}{2e^2E_F}$. The corresponding plasmon wavelength is

$$\lambda_p = \frac{2\pi}{q_p} = \frac{4\pi e^2 E_F}{(\hbar\omega)^2}. \quad (4.1)$$

Next, in Fig. 4.1(d) we plot the dispersion of HP²s in an h-BN slab of thickness $d = 58 \text{ nm}$ on SiO₂ (no graphene). In a stark contrast to isotropic crystals where longitudinal optical phonons occur at a single degenerate frequency ω_{LO} , in h-BN, multiple distinct branches of HP² exist [1,2,5]. These different branches correspond to quantized HP² waveguide modes [1,2,5] with a scalar potential oscillating across the slab and having different number of nodes [22]. Each waveguide mode disperses between ω_{TO} and ω_{LO} (Fig. 4.1(b)). Our theoretical results and discussion below are relevant for all these modes; the experimental results concern mainly the principal one, the nodeless waveguide mode of the lowest momentum. Finally, in Fig. 4.1(e) we display the dispersion of the new collective modes – HP³ – that arise from mixing of the SP² and HP² in the graphene/h-BN meta-structure. The

graphene Fermi energy $E_F = 0.37$ eV was estimated from the surface polariton wavelength in Fig. 4.3(d) (see also Ref. [19]). The modification of hyperbolic response by graphene is clearly manifested in the blueshift of the HP³ frequencies with respect to those of HP² (Figs. 4.1(d)-(e)). The shift of momenta (at a fixed frequency) is opposite in the two hyperbolic bands: negative in the Type II band and positive in the Type I band (Supplementary Information). This contrasting behavior stems from the fact that the polariton dispersion being negative and positive in the Type I and II region, respectively.

The change of the polariton wavelength induced by graphene is described by the formula (Supplementary Information):

$$\Delta\lambda(\%) = \frac{\lambda_{\text{HP}^3} - \lambda_{\text{HP}^2}}{\lambda_{\text{HP}^2}} \simeq \frac{\lambda_p}{\pi d} \frac{\varepsilon^z}{1 - \varepsilon^z \varepsilon^t} \quad (4.2)$$

In a typical situation where ε^z , ε^t are neither too large nor too small, this formula predicts that $\Delta\lambda(\%)$ is of the order of the ratio of the two length scales: the plasmon wavelength λ_p of graphene and the thickness d of h-BN. This clarifies why the influence of graphene remains substantial in h-BN as thick as $d = 300$ nm (value obtained from calculations in Supplementary Information): the length scale over which graphene can exert its influence on the electrodynamics of surrounding media is set by its plasmon wavelength. Importantly, the plasmon wavelength can be controlled over a wide range through an applied gate voltage. Thus, HP³s inherit the hyperbolic nature of HP²s while gaining an important added virtue: tunability with applied gate voltage. Outside the two HP³ regions, the plasmonic character of the dispersion is largely preserved (Fig. 4.1(e)). The polaritonic mode flattens out in the vicinity of ω_{TO} of either of the two hyperbolic bands: a consequence of mode

repulsion [23]. Similar interactions between plasmons and phonons have been studied in graphene on other substrates (e.g., SiO₂, SiC, ion gel et al.) and monolayer h-BN [9-13,17,20,23,24], where the hyperbolic response is not supported. Following the terminology established there, we refer to the collective modes existing outside the h-BN hyperbolic bands as surface plasmon-phonon polaritons (SP³) [17,19].

Infrared nano-imaging data (Figs. 4.2 and 4.3) visualizing the propagating polaritons in our meta-structures unambiguously support the above theoretical predictions. The basic principles of polariton imaging have been detailed elsewhere [1,5,10,11]. In short, when illuminated by the IR beam, the s-SNOM tip launches radially propagating polariton waves (Fig. 4.1(a)). The tip then registers the interference pattern between launched and edge-reflected polaritons, yielding oscillating fringes in the scattered near-field signal. The periodicity of the fringes is one-half of the polariton wavelength (denoted generically by λ , with suitable subscripts when needed).

In Fig. 4.2(a) we present nano-imaging data at a representative frequency $\omega = 1495 \text{ cm}^{-1}$ for a meta-structure that includes a slab of h-BN (thickness $d = 25 \text{ nm}$) partially covered by a heavily doped monolayer graphene. We observe polariton fringes in both covered (graphene/h-BN) and uncovered (h-BN) areas. In the uncovered h-BN region (the bottom half of Fig. 4.2(a)), the fringes originate from the Type II hyperbolic polaritons [1,5]. In the graphene/h-BN region (the upper part of the image in the middle of Fig. 4.2(a)) we observe fringes that are stronger and have a longer oscillation period. Prominent fringes can also be detected along the graphene edge (the dashed green line). Line profiles obtained normal to the h-BN edge (Fig. 4.2(b)) help to quantify the nearly 50% increase of both

amplitude and wavelength of the fringe oscillations due to the presence of doped graphene. This prominent modification is attributed to plasmon-phonon coupling and the formation of the type II HP³ band in our meta-structure (Figs. 4.1(e) and 4.2(c)).

We observe similar enhancement of polaritonic oscillations (Figs. 4.2(a)-(b)) at all ω within the Type II band. The blue dots in Fig. 4.2(c) display these data in the dispersion relation: ω plotted versus the polariton momentum q that can be read off the line profiles as $q = 2\pi / \lambda$. For comparison, we also measured the HP² dispersion for pristine h-BN (red triangles in Fig. 4.2(c)). Both data sets match the theoretical calculations (false colour and white lines, Supplementary Information) for the principle branch of hyperbolic polaritons. In addition to the principal mode, polaritons from higher order branches are also enhanced in graphene/h-BN (Supplementary Information). The largest experimentally observed $\Delta\lambda(\%) = 90\%$ in this data set is reached at $\omega = 1545 \text{ cm}^{-1}$. In comparison, the approximate equation (4.2) yields 98%, using $d = 25 \text{ nm}$, $\lambda_p = 180 \text{ nm}$ (equation (4.1)), $\epsilon^z = 2.77$, and $\epsilon^t = -1.98$. The agreement between the experiment, analytical theory, and numerical simulations attests to the validity of the plasmon-phonon coupling approach to account for the modified spectrum of hyperbolic modes. We performed measurements for a variety of samples, e.g., graphene on h-BN of different thicknesses, graphene obtained by exfoliation and chemical vapor deposition (CVD) techniques, all of which produced consistent results.

The tuning of polaritons in the Type II HP³ region via electrostatic gating (Methods) is presented in Figs. 4.3(a)-(b) at another representative frequency $\omega = 1395 \text{ cm}^{-1}$. When graphene is close to charge neutrality (Fig. 4.3(a)), the profile of propagating polariton in graphene/h-BN is nearly indistinguishable from that of uncovered h-BN. Once graphene is

doped by gating (Fig. 4.3(b)), both the intensity and wavelength of the polaritonic features were significantly increased. This systematic study of the gate-tunability is summarized in Fig. 4.3(c) (blue dots), where the wavelength consistently increases with the absolute value of gate voltage at fixed frequency $\omega = 1395 \text{ cm}^{-1}$.

Here we stress the distinction between the electrodynamics in HP³ and SP³ spectral regions (Fig. 4.1(e)). The latter are localized on the sample surface whereas the former propagate through the entire graphene/h-BN meta-structure (Fig. 4.3(d), inset) in the form of guided waves. We verified the waveguiding character by examining the thickness-dependence of HP³ wavelength using multiple h-BN slabs covered by a large sheet of CVD graphene. The Fermi energy for all the graphene/h-BN samples was about the same, $E_F = 0.37 \text{ eV}$. Both in experiment (blue dots) and simulations (green line), the dependence of the HP³ wavelength λ_{HP^3} on d is nearly linear with a finite intercept (Fig. 4.3 and Supplementary Information), where $\Delta\lambda(\%)$ ranges from 70% ($d = 25 \text{ nm}$) to 18% ($d = 99 \text{ nm}$). This law readily follows from two analytical results: $\Delta\lambda(\%) \sim d^{-1}$ (equation (4.2)) and $\lambda_{\text{HP}^2} \sim d$ (Ref. [1]). In contrast, the localized SP³ modes show essentially thickness-independent behavior of the polariton fringes outside the hyperbolic region (e.g., $\omega = 882$ and 1617 cm^{-1}). The fundamental difference between HP³ and SP³ is further illustrated by polariton field simulations (yellow traces in Fig. 4.3(d), inset). The field distribution of HP³ in graphene/h-BN is characteristic of a standing wave, whereas that of the SP³ is localized at the graphene/h-BN interface and decays evanescently in the interior of the h-BN.

4.4 Conclusion and Outlook

We conclude by pointing out that tunable hyperbolic response in graphene/h-BN devices does not introduce evident losses (Fig. 4.2(b)). The loss factor of HP^3 , defined as κ/q for the complex momentum $q + i\kappa$, can be as small as 0.06 but increases up to ~ 0.10 in the vicinity of the longitudinal phonon mode. In fact, the propagation length of HP^3 in graphene/h-BN is factor of 1.5–2.0 longer than HP^2 in h-BN (Fig. 4.2). Continuous and reversible in-situ tunability of hybrid polaritons in graphene/h-BN meta-structures demonstrated here (Fig. 4.3) is a significant advantage over other artificial and natural hyperbolic materials [1-4], and is appealing from both the perspective of fundamental physics as well as potential applications [3-5,25-29]. Thus, our work uncovers a practical approach for nano-photonic meta-structures with intertwined electronic, plasmonic, phononic, and/or exciton polaritonic properties [16]. Specifically, vdW polaritonic heterostructures with locally tunable properties fulfill the essential prerequisites for the implementation of transformation two-dimensional plasmonics [30,31]. The hybridization and graphene-induced tunability reported here are expected to be generic for other electromagnetic metamaterials [32] and vdW heterostructures [8,16]. A precondition for these effects is an overlap between various polaritonic dispersion branches. Finally, we remark that it is possible to make an analogy between altering the polariton dispersion by graphene and the Goos–Hänchen effect (GHE): a lateral shift of an optical beam upon reflection from an interface [33]. Theory of such a polaritonic GHE is reported elsewhere [34].

4.5 Methods

4.5.1 Experimental setup

The infrared (IR) nano-imaging and Fourier transform IR nano-spectroscopy (nano-FTIR) experiments introduced in the main text were performed using a scattering-type scanning near-field optical microscope (s-SNOM). Our s-SNOM is a commercial system (www.neaspec.com) based on a tapping-mode atomic force microscope (AFM). In the experiments, we use a commercial AFM tip (tip radius ~ 10 nm) with a PtIr₅ coating. The AFM tip is illuminated by monochromatic quantum cascade lasers (QCLs) (www.daylightsolutions.com), CO₂ lasers (www.accesslaser.com) and a broad-band laser source via difference frequency generation (DFG) (www.lasnix.com). Together, these lasers cover a frequency range of 700 – 2300 cm⁻¹ in the mid-IR. The s-SNOM nano-images were recorded by a pseudo-heterodyne interferometric detection module with an AFM tapping frequency 280 kHz and tapping amplitude around 70 nm. With this setup the s-SNOM is able to probe the optical signal from sub-surface objects up to a depth of ~ 250 nm. In order to subtract background signal, the s-SNOM output signal was demodulated at the 3rd harmonics of the tapping frequency. In this work, we report our near-field data in the form of the normalized scattering amplitude using gold as the reference: $s(\omega) = s_{\text{sample}}(\omega) / s_{\text{Au}}(\omega)$.

4.5.2 Sample fabrication

Hexagonal boron nitride (h-BN) crystals were mechanically exfoliated from bulk samples and deposited onto Si wafers capped with 300 nm thick SiO₂. Graphene was then placed onto the h-BN using a PMMA-transfer method. In this work, we use graphene from

either mechanical exfoliation or chemical vapor deposition (CVD) synthesis and get similar results from both techniques. The gold film used as the reference in our measurements was lithographically fabricated on the same substrate. Electrostatic back-gating was accomplished by applying the voltage between the Si wafer and graphene layer, with SiO₂ and h-BN as the gate dielectrics.

4.6 Supplementary Information

4.6.1 Response functions and eigenmode dispersion of graphene-boron nitride heterostructures

In our theoretical model, we treat graphene/h-BN/SiO₂ structure as an infinite stratified medium consisting of three regions: $z > 0$ (vacuum, $j = 0$), $-d < z < 0$ (h-BN, $j = 1$), and $z < -d$ (SiO₂, $j = 2$). We allow for possibility of a uniaxial anisotropy of each of the regions and denote by $\varepsilon_j^t = \varepsilon_j^t(\omega)$ and $\varepsilon_j^z = \varepsilon_j^z(\omega)$, respectively, their in-plane and the z -axis dielectric functions. (In reality, only the middle region is optically anisotropic.) The dielectric functions of h-BN are taken from [35] and those of SiO₂ from Ref. [20]. Graphene layer is treated as a two-dimensional layer with sheet conductivity $\sigma(q, \omega)$ given by (Ref. [36]):

$$\sigma = -i \frac{e^2}{4\hbar} \frac{\zeta}{\sqrt{v^2 q^2 - \zeta^2}} \left[1 + G\left(\frac{\hbar\zeta + 2E_F}{\hbar v q}\right) - G\left(\frac{\hbar\zeta - 2E_F}{\hbar v q}\right) \right] - \frac{2i e^2 \omega E_F}{\pi (\hbar v q)^2}, \quad (4.3)$$

$$G(\alpha) = -\frac{1}{\pi} \left(\alpha \sqrt{1 - \alpha^2} - \arccos \alpha \right), \quad \zeta = \omega + \frac{i}{\tau}.$$

Here E_F is the graphene Fermi energy, v is the Fermi velocity, and τ^{-1} is the phenomenological relaxation rate. Following the standard procedure, for the case of the P -polarization, the in-plane electric field in the system is written as $E_x(x, z) = e^{iqx}e_x(z)$, where the amplitude function $e_x(z)$ is the sum of two counter-propagating waves:

$$e_x(z) = A_j e^{-ik_j^z z} + B_j e^{ik_j^z z}, \quad k_j^z = \sqrt{\varepsilon_j^t \left(\frac{\omega^2}{c^2} - \frac{q^2}{\varepsilon_j^z} \right)}, \quad \Im k_j^z > 0. \quad (4.4)$$

The coefficients A_j and B_j can be expressed in terms of the reflection coefficients r_{ij} at the interfaces, defined by

$$\begin{aligned} r_{01} &= \frac{Q_1 - Q_0 + S}{Q_1 + Q_0 + S}, & r_{10} &= \frac{Q_0 - Q_1 + S}{Q_0 + Q_1 + S}, & r_{12} &= \frac{Q_2 - Q_1}{Q_2 + Q_1}, \\ Q_j &= \frac{\varepsilon_j^t}{k_j^z}, & S &= \frac{4\pi}{\omega} \sigma(q, \omega). \end{aligned} \quad (4.5)$$

For a particular choice of the overall normalization factor, these expressions are

$$\begin{aligned} A_0 &= -r_p^{-1} B_0, & B_0 &= -\frac{r_{01} + r_{12}(1 - r_{01} - r_{10})e^{2ik_1^z d}}{1 - r_{01}}, \\ A_1 &= 1, & B_1 &= -r_{12}e^{2ik_1^z d}, \\ A_2 &= (1 - r_{12})e^{i(k_1^z - k_2^z)d}, & B_2 &= 0. \end{aligned} \quad (4.6)$$

The total complex reflectivity r_p of the structure is given by

$$r_p = \frac{r_{01} + r_{12}(1 - r_{01} - r_{10})e^{2ik_1^z d}}{1 - r_{10}r_{12}e^{2ik_1^z d}}. \quad (4.7)$$

(The subscript “ P ” in r_p stands for the P -polarization. The remaining S -polarization is not important in the near-field limit, $q \gg \omega/c$, we study here.)

In an idealized non-dissipative system, $r_p(q, \omega)$ can have poles at real ω and q . At such poles the amplitude A_0 of the incident wave vanishes, so that the field distribution described by Eq. (4.6) is self-sustained, i.e., an eigenmode. As one can see from Eq. (4.7), the equation for the poles is:

$$1 - r_{10}r_{12}e^{2ik_1^z d} = 0. \quad (4.8)$$

If the frequency ω belongs to a hyperbolic region, this equation has infinite number of solutions q_l corresponding to different branches of hyperbolic plasmon-phonon polaritons (HP³). Here l is an integer that labels the branch. In the near-field limit $q \gg \omega/c$, which is realized in our experiment, we can use the approximation

$$\frac{k_j^z}{q} \simeq i \frac{\varepsilon_j(\omega)}{\varepsilon_j^z(\omega)}, \quad \varepsilon_j(\omega) \equiv \sqrt{\varepsilon_j^t(\omega)} \sqrt{\varepsilon_j^z(\omega)}, \quad (4.9)$$

to transform the equation q_l into the form similar to Eq. (1) of Ref. [1]:

$$q_l(\omega) = \frac{\pi}{[-\tan \theta(\omega)] d} [l - f(q_l, \omega)], \quad \tan \theta(\omega) = i \frac{\varepsilon_1(\omega)}{\varepsilon_1^z(\omega)}. \quad (4.10)$$

Note that the quantity $\tan \theta$ is real. It specifies the slope of the polariton propagation direction in h-BN with respect to the z-axis. In the type II hyperbolic band where most of our experimental data are taken, we have $\tan \theta < 0$ and $f(q_l, \omega) < 0$ (see below), and so the dispersion branches with positive momentum q_l are obtained choosing $l = 0, 1, 2, \dots$. Conversely, in the type I band $\tan \theta > 0$ and negative l should be chosen. Function $f(q, \omega)$ in Eq. (4.10) represent the phase shift (normalized to 2π) of the polariton internal reflections off the h-BN surfaces. Since there two such surfaces (top and bottom), it is the sum of two terms:

$$f(q_l, \omega) = -\frac{1}{\pi} \arctan \left[\frac{i\varepsilon_0(\omega)}{\varepsilon_1(\omega)} \left(1 - \frac{2q}{q_p(\omega)} \right) \right] - \frac{1}{\pi} \arctan \left[\frac{i\varepsilon_2(\omega)}{\varepsilon_1(\omega)} \right], \quad (4.11)$$

where

$$q_p(\omega) \equiv \frac{i\omega\varepsilon_0}{2\pi\sigma(q_p, \omega)} \simeq \frac{\varepsilon_0}{e^2} \frac{(\hbar\omega)^2}{2E_F} \quad (4.12)$$

has the physical meaning of the plasmon momentum in free-standing graphene. (More precisely, it is the plasmon momentum of graphene in a medium with dielectric constant ε_0 . Note also that the second equality in Eq. (4.12) is the same as Eq. (4.1) except therein we replaced ε_0 by unity, to lighten the notations.)

Upon examination of Eqs. (4.10) and (4.11), we conclude that the HP³ wavelength $\lambda_l = 2\pi/q_l$ must fall into the interval between λ_l^{ins} and λ_l^{met} :

$$\lambda_l^{\text{ins}}(\omega) = 2d \frac{[-\tan \theta(\omega)]}{l - f^{\text{ins}}(\omega)}, \quad \lambda_l^{\text{met}}(\omega) = 2d \frac{[-\tan \theta(\omega)]}{l - f^{\text{met}}(\omega)}, \quad (4.13)$$

where the phase shifts $f^{\text{ins}}(\omega)$ and $f^{\text{met}}(\omega)$ are defined by

$$f^{\text{ins}}(\omega) = -\frac{1}{\pi} \arctan \left[\frac{i\varepsilon_0(\omega)}{\varepsilon_1(\omega)} \right] - \frac{1}{\pi} \arctan \left[\frac{i\varepsilon_2(\omega)}{\varepsilon_1(\omega)} \right], \quad (4.14)$$

$$f^{\text{met}}(\omega) = \frac{1}{2} - \frac{1}{\pi} \arctan \left[\frac{i\varepsilon_2(\omega)}{\varepsilon_1(\omega)} \right]. \quad (4.15)$$

(In our system where $\varepsilon_2 > \varepsilon_0 = 1$ in the hyperbolic spectral regions both f^{ins} and f^{met} are negative.) The bound $\lambda_l^{\text{met}}(\omega)$ is reached if the graphene sheet is replaced by a perfect metal with infinite conductivity. The other bound $\lambda_l^{\text{ins}}(\omega)$ is obtained if the graphene sheet is treated as a perfect insulator with vanishing conductivity. Obviously, the latter is the same as the wavelength of hyperbolic phonon polaritons (HP²) modes in an h-BN crystal without graphene [1]. In practice, we deal with an intermediate case, and so to find q_l we

need to solve the transcendental equation Eq. (4.10). An approximate solution can be derived as follows. We note that most of our experimental data are taken at frequencies where $|\varepsilon_1(\omega)|$ given by Eq. (4.9) is only modestly large and also λ_l is comparable or larger than the plasmon wavelength $\lambda_p \equiv 2\pi/q_p$ (which is about 190 nm at $E_F = 0.37$ eV, see Fig. 4.1). In this regime, it is permissible to expand function $f(q, \omega)$ in Eq. (4.11) to the first order in q . After simple algebra, one can find an analytical expression for the fractional change of the polariton wavelength. Interestingly, it is l -independent and is given by

$$\frac{\lambda_l - \lambda_l^{\text{ins}}}{\lambda_l^{\text{ins}}} \simeq \frac{\lambda_p}{\pi d} \frac{\varepsilon_0 \varepsilon_1^z}{\varepsilon_0^2 - \varepsilon_1^z \varepsilon_1^t}, \quad \frac{\lambda_l}{\lambda_p} \gg \min\left\{\frac{\varepsilon_0}{|\varepsilon_1(\omega)|}, 2\right\}. \quad (4.16)$$

(This is the same as Eq. (4.2) except therein we replaced ε_0 by unity and dropped the subscripts of $\varepsilon_1^z, \varepsilon_1^t$, to lighten the notations once again.) Equation (4.16) accounts for the key experimental observations. First, it shows that at a fixed frequency, addition of graphene decreases the polariton wavelength in the type I spectral band and increases it in the type II one. This agrees with the experimental results presented in Fig. 4.2 and Fig. 4.5(d) below and also with the numerical results shown in Figs. 4.2(c), 4.4, and 4.5(c). Next, Eq. (4.16) clarifies which material parameters determine the magnitude of the observed wavelength variation. As expected, the fractional change in the wavelength decreases with h-BN thickness d . The range of d where it remains appreciable is proportional to the plasmon wavelength λ_p of graphene in vacuum and is approximately inversely proportional to the in-plane dielectric function of h-BN $\varepsilon_1^t(\omega)$. This explains why the influence of monolayer graphene on polaritons in rather thick h-BN crystals is still readily observable. For example, at $\omega = 1525 \text{ cm}^{-1}$ where $\varepsilon_1^t = -2.9$, $\varepsilon_1^z = 2.8$,

Eq. (4.14) predicts a $\Delta\lambda(\%) = 80\%$ wavelength change for $d = 25$ nm (Fig. 4.2(c)) and a $\Delta\lambda(\%) = 20\%$ change at $d = 100$ nm (Fig. 4.3(d)).

If the thickness is fixed, the fractional change in λ_l grows as ω approaches the top of the type II band, where $\varepsilon_1(\omega)$ tends to zero. This is again in agreement with the numerical results in Fig. 4.4. Note that in this frequency range one eventually enters the regime $|\varepsilon_1(\omega)| \ll \varepsilon_0$ in which the domain of validity of Eq. (4.16) is restricted to $\lambda_l > 2\lambda_p$. At $\lambda_l < 2\lambda_p$ (or equivalently, at $q > q_p/2$) the polariton wavelength λ_l should approach the perfect-metal bound $\lambda_l^{\text{met}}(\omega)$ [Eq. (4.13)]. The crossover to this limiting value is sharp, almost step-like if $|\varepsilon_1(\omega)| \ll \varepsilon_0$. If $|\varepsilon_1(\omega)| \sim \varepsilon_0$, this crossover is smooth.

For the absolute change of the wavelength, Eqs. (4.10), (4.13), and (4.16) yield

$$\lambda_l \simeq \lambda_l^{\text{ins}} - \frac{2}{\pi} \frac{i\varepsilon_0\varepsilon_1}{\varepsilon_0^2 - \varepsilon_1^z\varepsilon_1^t} \frac{\lambda_p}{l - f^{\text{ins}}}, \quad \frac{\lambda_l}{\lambda_p} \gg \min\left\{\frac{\varepsilon_0}{|\varepsilon_1(\omega)|}, 2\right\}. \quad (4.17)$$

This formula is consistent with the observed linear thickness dependence of the HP³ wavelength at constant frequency (Fig. 4.3(d)). Indeed, the first term on the right-hand side of Eq. (4.17) is linear in d , while the second term is thickness-independent. If $l \neq 0$, at very small d the inequality indicated in Eq. (4.17) can be violated, in which case the dependence on d should become sublinear and eventually flatten out. For the principal branch $l = 0$, a particularly formula for the polariton wavelength can be obtained for frequencies $\omega \simeq \omega_{\text{T0}}$ near the bottom of the hyperbolic bands. Using Eqs. (4.14) and (4.17), we find

$$\lambda_0 \simeq \frac{2}{\varepsilon_0 + \varepsilon_2} (\pi\varepsilon_1^t d + \varepsilon_0\lambda_p), \quad |\varepsilon_1(\omega)| \gg \varepsilon_0, \varepsilon_2. \quad (4.18)$$

This equation predicts the linear in thickness behavior of λ_0 down to $d = 0$. Note that ε_1^z does not enter Eq. (4.18); hence, the anisotropy of h-BN does not play much role in this

regime. Our experimental data for gated G-h-BN structures shown by the blue circles in Fig. 4.3(c) are in a qualitative agreement with Eq. (4.18).

The foregoing discussion neglected dissipation always present in real materials. Because of such dissipation $r_p(q, \omega)$ never diverges at any real ω and q . As long as the dissipation is weak, we can still define eigenmodes dispersions; however, it is convenient to get them not from the poles of $r_p(q, \omega)$ but from the locations of resonances (sharp maxima) of function $\Im r_p(q, \omega)$ at real ω . This function, which in fact is the measure of dissipation, is shown as a false color map in Figs. 4.1(d)-(e) and 4.2(c) and Figs. 4.4, 4.5(c) below. The bright lines delineate the dispersions of the modes and their widths represent the frequency linewidth of the resonances. The maps in Figs. 4.4(a)-(d) were computed for h-BN thickness of 50, 100, 150, and 300 nm, respectively. For comparison, the dispersion of HP²s of a bare h-BN substrate are shown by the white lines. In agreement with Eq. (4.16), the momenta of HP³s in graphene/h-BN meta-structures are shifted to smaller momenta (larger wavelengths) compared to HP²s. The effect remains strong for h-BN as thick as 300 nm (in general, as long as d is not much larger than λ_p). Outside the Type II hyperbolic region, surface plasmon-phonon polaritons (SP³s) exhibit little dependence on the meta-structure thickness, as discussed above.

To calculate the electric field profile of the eigenmodes in the presence of damping (insets of Fig. 4.3(d)), we used Eqs. (4.5) and (4.6) except we set coefficient A_0 to zero and set B_0 to $1 - r_{12}e^{2ik_1^z d}$, for continuity.

4.6.2 Tunable polaritons and plasmon-phonon coupling around the

Type I region

Tunable hyperbolic response and plasmon-phonon coupling is also observed in the Type I hyperbolic region. Single-wavelength nano-imaging experiments in the Type I region are severely restricted by the current availability of monochromatic IR lasers necessitating the need for using broadband mid-IR laser for the following measurements. Spectroscopic data ($\omega = 600$ to 1000 cm^{-1}) were obtained with our nanoscale Fourier transform infrared spectroscopy (nano-FTIR) setup and provide a complete experimental picture of the polaritonic response in this region (Fig. 4.5(b)). It is instructive to represent these broadband data in the form of a single spectroscopic line scan (Figs. 4.5(a)-(b)) following Ref. [1]. The line scan is plotted as a false color map of the scattering amplitude $s(\omega, L)$ which varies with infrared (IR) frequency (ω) and position (L) along the scanning direction. For bare h-BN ($L < 0$), the out-of-plane phonon generates strong signal near $\omega \sim 770 \text{ cm}^{-1}$. We can examine experimental results obtained as the tip scans across the graphene edge ($L = 0$) and continues into the interior of the graphene/h-BN ($L > 0$). The h-BN phonon resonance is strongly enhanced and blue shifted as a result of the presence of monolayer graphene for $L > 0$, consistent with the spectra displayed in Fig. 1b. These findings point to tunable polaritons similar to that in the Type II region (Figs. 4.2-4.3).

We stress that the phase and group velocity corresponding to the dispersion in the Type I region are antiparallel. This negative dispersion underlies subtle but important differences related to graphene-induced modification of phonon polaritons of h-BN. Specifically, the hybrid HP^3 modes in the Type I region reveal an increased q or reduced

wavelength λ in contrast with the opposite changes observed in the Type II region (Fig. 4.2).

Furthermore, we wish to point out that the hybrid polariton in Type I hyperbolic region splits the surface plasmon polariton (SP^2) (Fig. 4.1(c)) of free standing graphene into two SP^3 s ($\omega < 746 \text{ cm}^{-1}$ and $\omega > 819 \text{ cm}^{-1}$, Fig. 4.5(b)) in graphene/h-BN. The SP^3 fringes were observed close to the graphene edge (Fig. 4.5(b), $L > 0$). As discussed above, these SP^3 s are localized to the graphene so their dispersion has effectively no dependence on the h-BN thickness (Fig. 4.2(d)). At lower frequencies ($\omega = 600$ to 1000 cm^{-1}), both the HP^3 resonance (Fig. 4.5(b)) and SP^3 s (Fig. 4.5(b)) can be tuned via electrostatic back-gating. The HP^3 resonance (bright ribbon in Fig. 4.5(b)) peaks at 780 cm^{-1} (Fig. 2d) when graphene is close to charge neutrality. As the back-gate voltage ($V_{BG} - V_{CN}$) increases (in either polarity), the HP^3 resonance is blue shifted and until reaching the boundary of Type I region ($\sim 815 \text{ cm}^{-1}$), yet another effect originating from strong plasmon-phonon coupling. Propagation of the SP^3 can be imaged with the nano-imaging technique introduced in the main text. A representative IR image ($\omega = 882 \text{ cm}^{-1}$) of a tapered graphene/h-BN is shown as the inset of Fig. 4.5e. The SP^3 fringes run parallel to the graphene edges. The fringes closest to the edges (white dashed lines) are the strongest and are followed by weaker, increasingly damped fringes. Similar to graphene on other substrates [10-13,24], the wavelength of SP^3 in graphene/h-BN can be tuned by varying the back-gate voltage (Fig. 4.5(e)).

4.6.3 Higher order hyperbolic polaritons in graphene/h-BN meta-

structures

In this work, we provide theoretical analysis for graphene/h-BN polaritons from all hyperbolic branches. Yet the majority of experimental results are confined to the principal $l = 0$ branch for the following reason. Higher order ($l = 1, 2, 3 \dots$) polaritons are weaker and occur at much larger momenta. The increased momentum results in significantly smaller wavelengths λ as compared to the principal branch. Therefore, these polaritons are highly confined and can only be observed in its immediate vicinity of the sample edge, leading to a small oscillation (Fig. 4.6(b), $0 < L < 150$ nm, overlapped with the green background). In spite of this, hybridization for $l \neq 0$ polaritons was also observed in our experiments, where the small oscillation was enhanced by graphene (Figs. 4.6(a)-(b)). However, due to the resolution limit of our nano-IR apparatus and the unknown (possibly, complicated) structure of graphene-covered h-BN edges, quantitative results for $l \neq 0$ polaritons may need future experiments.

4.7 Acknowledgements

This work is supported by DOE-BES, Moore foundation, AFOSR, UCOP and ONR.

Chapter 4, in full, is a reprint of the material as it appears in S. Dai, Q. Ma, M. K. Liu, T. Andersen, Z. Fei, M. D. Goldflam, M. Wagner, K. Watanabe, T. Taniguchi, M. Thiemens, F. Keilmann, G. C. A. M. Janssen, S-E. Zhu, P. Jarillo-Herrero, M. M. Fogler & D. N. Basov. "Graphene on hexagonal boron nitride as a tunable hyperbolic metamaterial". *Nature Nanotech.* 10, 682-686 (2015). The dissertation author was the primary investigator and author of this paper.

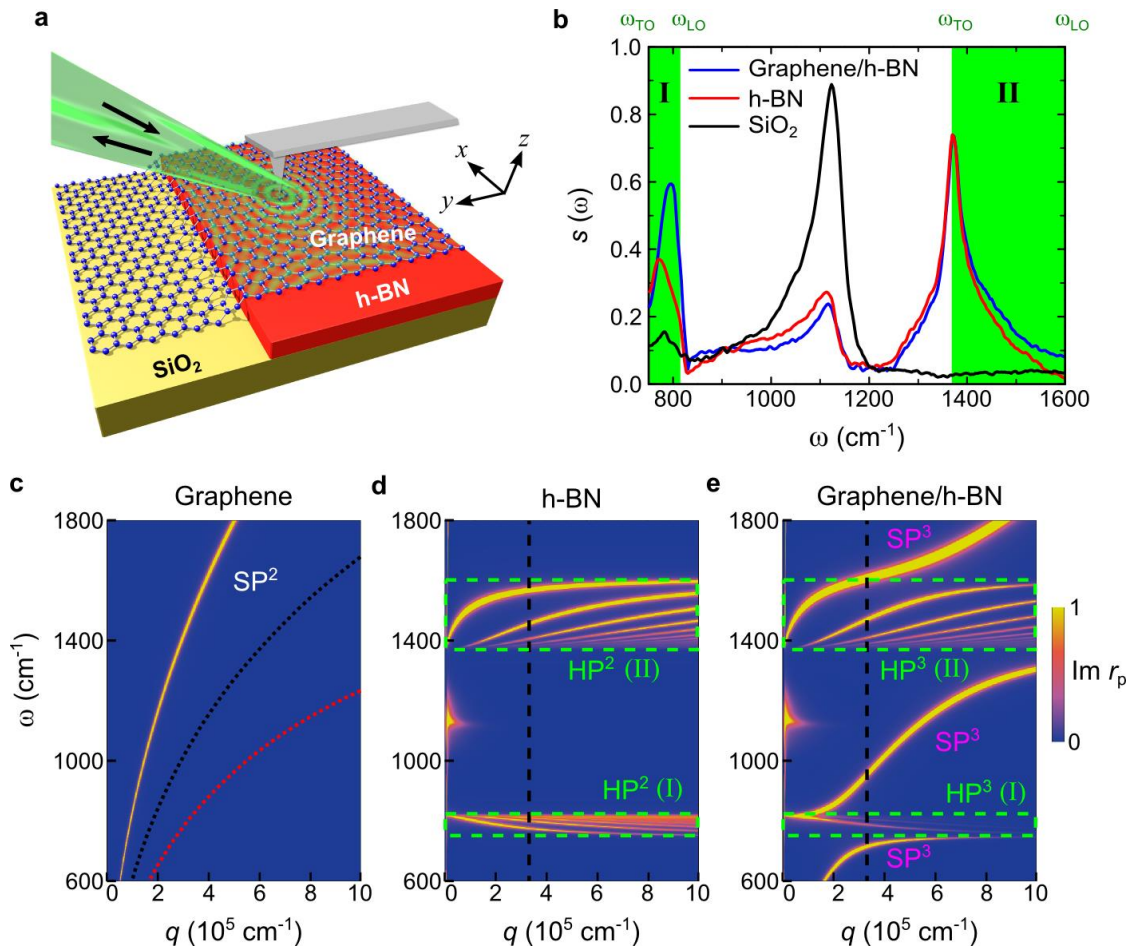


Figure 4.1: An Overview of hybridized hyperbolic response in graphene/h-BN meta-structure. (a), The experimental schematic showing the IR beams (the black arrows) incident on and back-scattered by an AFM tip. The incident beam is generated from monochromatic or broad-band laser sources (Methods). The back-scattered light is collected for extraction of the near-field signal. (b), Broad-band nano-IR spectra of the meta-structure with a representative thickness of h-BN: 58 nm. The blue, red and black curves represent the spectra for graphene/h-BN, h-BN, and SiO₂, respectively. The spectra are collected far away from the sample edges where the impact of edge-reflected polaritonic waves is negligible. (c), Calculated dispersion of the surface plasmon polariton (SP²) in freestanding graphene with Fermi energy $E_F = 0.37, 0.15, \text{ and } 0.08 \text{ eV}$. (d), Calculated dispersion of the hyperbolic phonon polariton (HP²) in h-BN of thickness 58 nm. The dispersion is visualized using the false colour map of the imaginary part of the reflection coefficient r_p (for the case of P -polarization, see Supplementary Information). The black dashed line is a rough estimate of the momentum at which the tip-sample coupling is the strongest [20]. The green dashed rectangles surround the regions of hyperbolic response. (e), Same as (d) for graphene/h-BN structure with $E_F = 0.37 \text{ eV}$. The false colour map reveals the dispersion of the hyperbolic plasmon-phonon polaritons (HP³) and the surface plasmon-phonon polaritons (SP³). Weak resonances around $\omega = 1130 \text{ cm}^{-1}$ in (d) and (e) originate from the SiO₂ substrate.

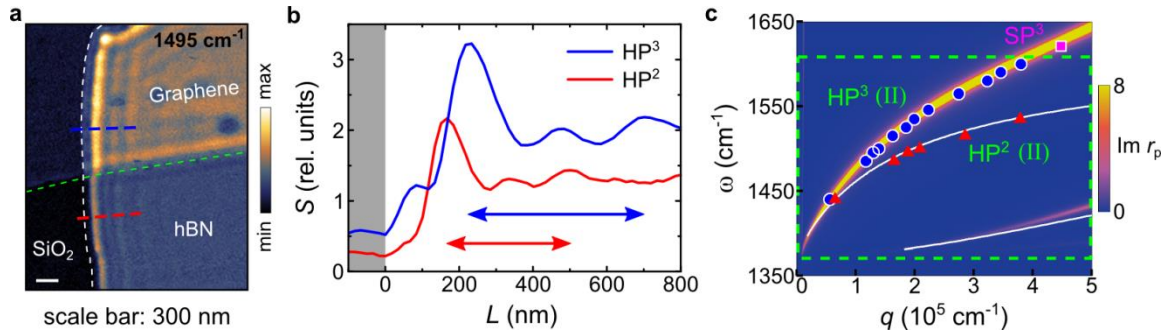


Figure 4.2: Modification of type II hyperbolic phonon polaritons in graphene/h-BN meta-structure. (a), Near-field amplitude image of the graphene/h-BN at frequency $\omega = 1495 \text{ cm}^{-1}$. With monolayer graphene, the intensity and wavelength of phonon polariton in pristine h-BN are increased. White and green dashed lines indicate the edge of h-BN and graphene, respectively. Scale bar: 300 nm, $d = 25 \text{ nm}$. (b), Line profiles taken along the dashed lines in (a). Double arrows indicate the polariton wavelength measured on graphene/h-BN (blue) and h-BN (red). (c), Experimental dispersion relation of type II HP^2 in h-BN (red triangles), HP^3 (blue dots) and SP^3 in graphene/h-BN (pink square) with the Fermi energy $E_F = 0.37 \text{ eV}$. The corresponding simulation results are also provided as the white lines and false colour map, respectively.

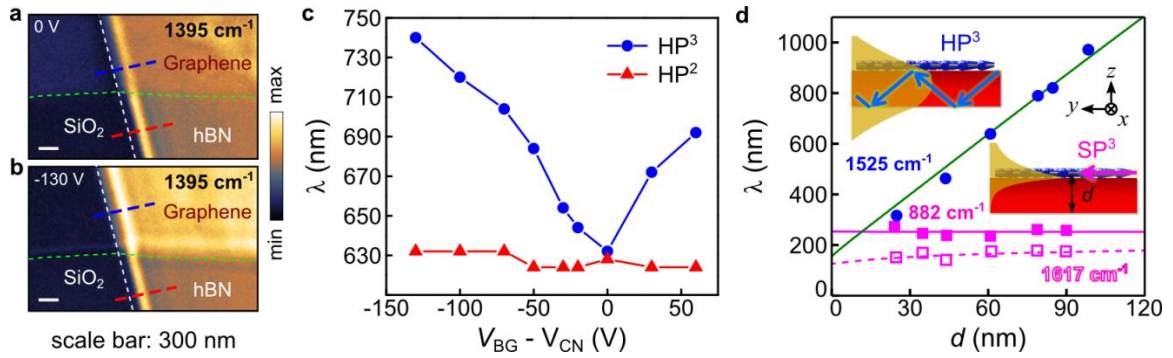


Figure 4.3: Tuning of the graphene/h-BN polariton wavelength by electrostatic gating and varying the meta-structure thickness. (a)-(b), Near-field images of graphene/h-BN and h-BN polaritons at back gate (BG) voltages relative to the charge neutral (CN) state $V_{\text{BG}} - V_{\text{CN}} = 0$ V (a) and -130 V (b). Scale bar: 300 nm. (c), Gate voltage dependence of the HP^3 wavelength in graphene/h-BN meta-structure (blue dashed line in Figs. 4.3(a)-(b)) and the apparent lack of thereof for HP^2 in h-BN (red dashed line in Figs. 4.3(a)-(b)) at $\omega = 1395$ cm^{-1} . Thickness of the h-BN in (a)-(c): $d = 4$ nm. (d), The dependence of HP^3 's wavelength on h-BN thickness at $\omega = 1525$ cm^{-1} (data and simulations are shown with the blue dots and green line, respectively). For the SP^3 , there is no systematic thickness-dependence (solid and hollow pink squares at $\omega = 882$ and 1617 cm^{-1} , respectively). The corresponding simulations are plotted as the solid and dashed lines). Inset, the propagation schematics for HP^3 (top) and SP^3 (bottom). Yellow shapes in each inset show the real part of the polariton field as a function of z obtained using equation (4.6).

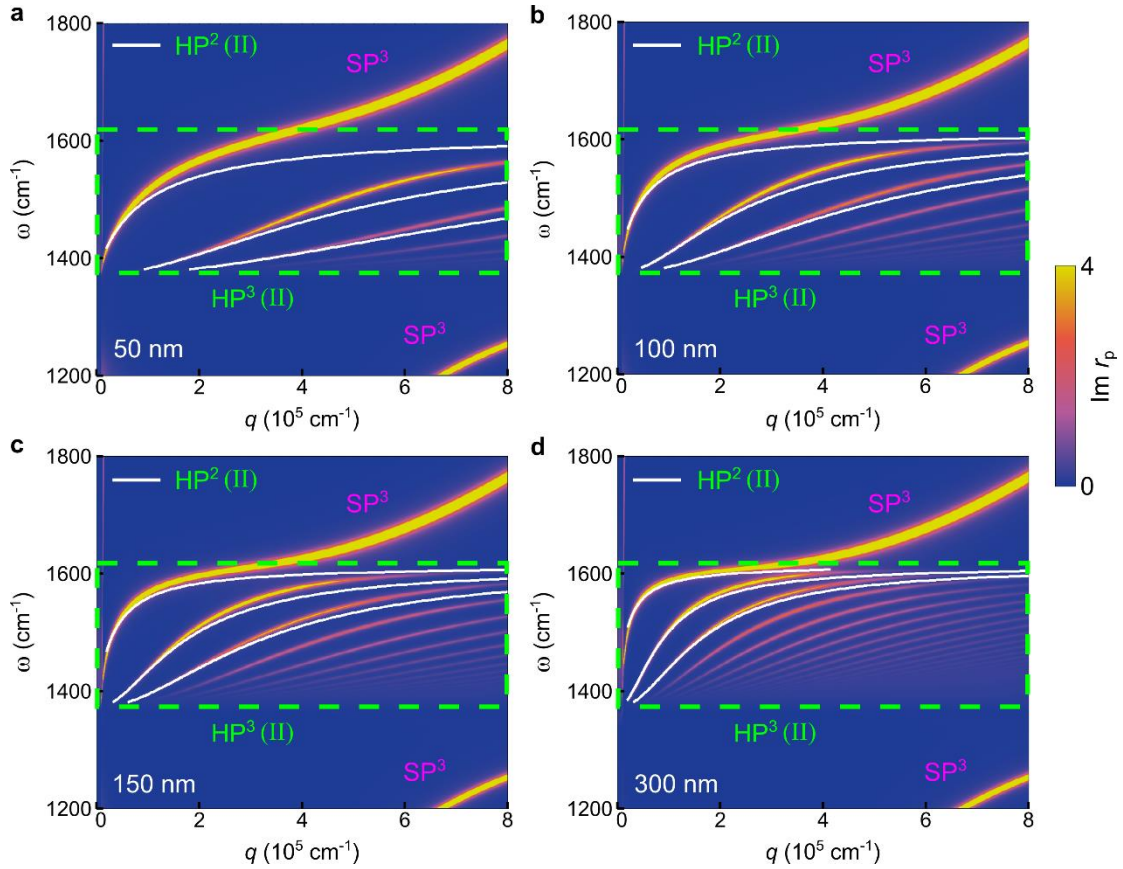


Figure 4.4: Frequency (ω) - momentum (q) dispersion of polaritons in graphene/h-BN meta-structure with different thicknesses. (a), Dispersion of hyperbolic phonon polaritons (HP^2_s) in h-BN (white lines), hyperbolic plasmon-phonon polaritons (HP^3_s) and surface plasmon-phonon polaritons (SP^3_s) in graphene/h-BN (false color). The green dashed line marks the spectral boundaries of the type II hyperbolic region. h-BN thickness is 50 nm, the graphene Fermi energy $E_F = 0.37$ eV. (b)-(d), Same as (a) for h-BN thickness 100, 150 and 300 nm, respectively.

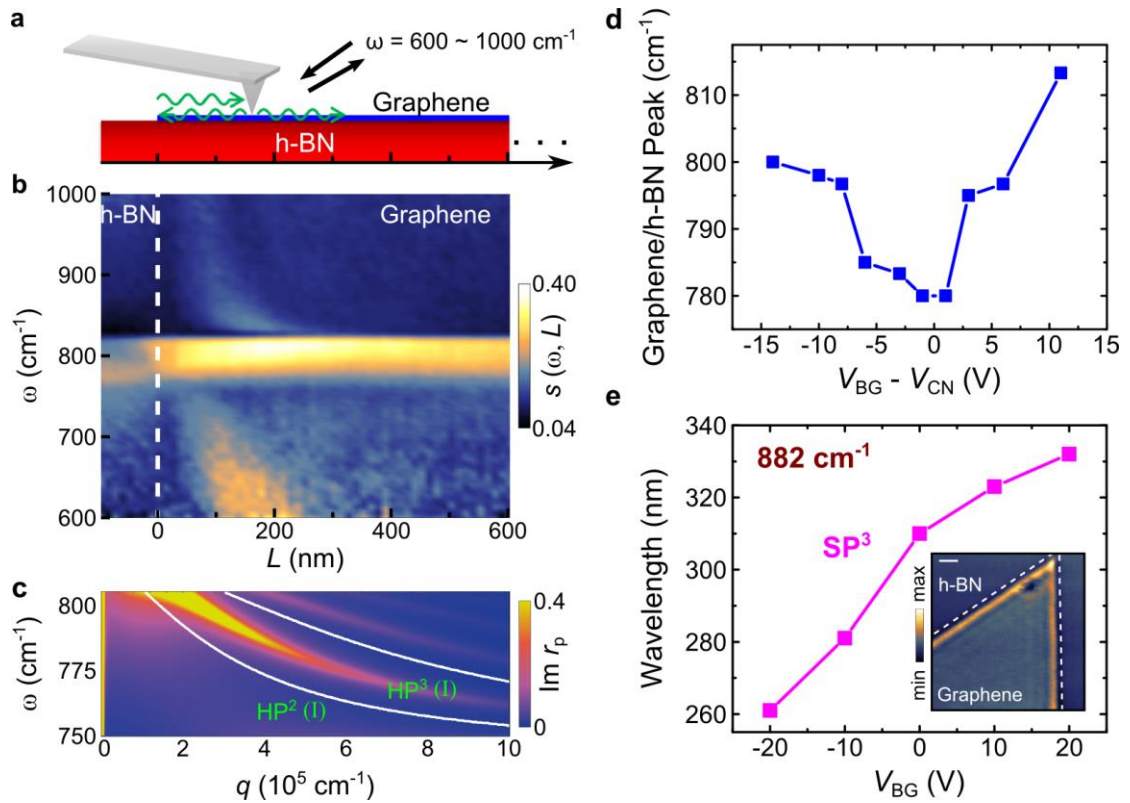


Figure 4.5: Tunable hyperbolic response and hybrid polaritons in the lower frequency region ($\omega = 600 - 1000 \text{ cm}^{-1}$). (a), Schematic of the nano-FTIR line scan experiment. Black arrows indicate incident and back-scattered IR beam. Green arrows describe the SP^3 s launched from the AFM tip and reflected by graphene edge at $L = 0$. (b), The polaritonic overview from 600 to 1000 cm^{-1} mapped by the nano-FTIR line scan. The scattering amplitude $s(L, \omega)$ is mapped with the false color. White dashed line marks the $L = 0$ graphene edge. (c), The polariton dispersion in the Type I region. The HP^2 and HP^3 are plotted as white lines and false color map. Thickness of h-BN: 50nm, the graphene Fermi energy $E_F = 0.37 \text{ eV}$. (d), The HP^3 resonance peak position (bright region in Fig. S3b) as a function of the back-gate voltage V_{BG} referenced to the graphene charge-neutrality voltage V_{CN} . (e), Back-gate voltage dependence of the SP^3 wavelength extracted from the near-field images measured at $\omega = 882 \text{ cm}^{-1}$ using a monochromatic laser source. Inset: a representative near-field image of the SP^3 . Scale bar: 200 nm.

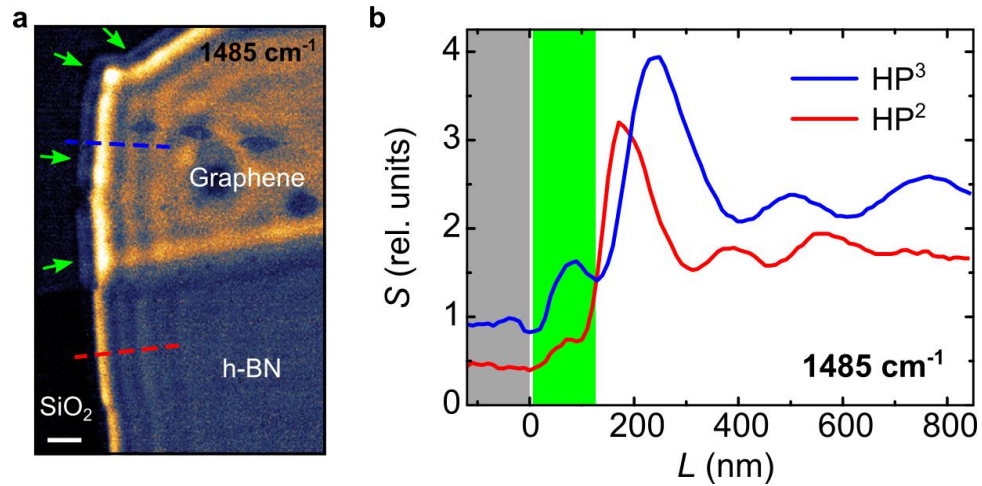


Figure 4.6: Supplementary s-SNOM data for hybridization of $l \neq 0$ hyperbolic polaritons. (a), Near-field amplitude image of the graphene/h-BN at frequency $\omega = 1485 \text{ cm}^{-1}$. A bright line (higher near-field signal, indicated by the blue arrows) formed very close to the sample edge for the part covered by graphene. Scale bar: 300 nm, $d = 25 \text{ nm}$. (b), Line profiles taken along the dashed lines in (a). The part with green background shows enhanced polaritonic features from $l \neq 0$ branches in graphene/h-BN (blue) compared with that in h-BN (red).

4.8 Bibliography

1. Dai, S. *et al.* Tunable Phonon Polaritons in Atomically Thin van der Waals Crystals of Boron Nitride. *Science* **343**, 1125-1129, (2014).
2. Caldwell, J. D. *et al.* Sub-diffractive volume-confined polaritons in the natural hyperbolic material hexagonal boron nitride. *Nat Commun* **5**, (2014).
3. Guo, Y., Newman, W., Cortes, C. L. & Jacob, Z. Applications of Hyperbolic Metamaterial Substrates. *Advances in OptoElectronics* **2012**, 9, (2012).
4. Poddubny, A., Iorsh, I., Belov, P. & Kivshar, Y. Hyperbolic metamaterials. *Nat Photon* **7**, 948-957, (2013).
5. Dai, S. *et al.* Subdiffractive focusing and guiding of polaritonic rays in a natural hyperbolic material. *Nat Commun* **6**, (2015).
6. Novotny, L. & Hecht., B. *Principles of Nano-Optics*. (Cambridge University Press, Cambridge, 2006).
7. Xu, X. G. *et al.* One-dimensional surface phonon polaritons in boron nitride nanotubes. *Nat Commun* **5**, (2014).
8. Geim, A. K. & Grigorieva, I. V. Van der Waals heterostructures. *Nature* **499**, 419-425, (2013).
9. Ju, L. *et al.* Graphene plasmonics for tunable terahertz metamaterials. *Nat Nano* **6**, 630-634, (2011).
10. Chen, J. *et al.* Optical nano-imaging of gate-tunable graphene plasmons. *Nature* **487**, 77-81, (2012).
11. Fei, Z. *et al.* Gate-tuning of graphene plasmons revealed by infrared nano-imaging. *Nature* **487**, 82-85, (2012).
12. Fang, Z. *et al.* Active Tunable Absorption Enhancement with Graphene Nanodisk Arrays. *Nano Letters* **14**, 299-304, (2014).
13. Gerber, J. A., Berweger, S., O'Callahan, B. T. & Raschke, M. B. Phase-Resolved Surface Plasmon Interferometry of Graphene. *Physical Review Letters* **113**, 055502, (2014).
14. Cai, W. & Shalaev, V. *Optical Metamaterials: Fundamentals and Applications*. (Springer, New York, 2010).

15. Fiori, G. *et al.* Electronics based on two-dimensional materials. *Nat Nano* **9**, 768-779, (2014).
16. Xia, F., Wang, H., Xiao, D., Dubey, M. & Ramasubramaniam, A. Two-dimensional material nanophotonics. *Nat Photon* **8**, 899-907, (2014).
17. Brar, V. W. *et al.* Hybrid Surface-Phonon-Plasmon Polariton Modes in Graphene/Monolayer h-BN Heterostructures. *Nano Letters* **14**, 3876-3880, (2014).
18. Xu, X. G. *et al.* Mid-infrared Polaritonic Coupling between Boron Nitride Nanotubes and Graphene. *ACS Nano* **8**, 11305-11312, (2014).
19. Woessner, A. *et al.* Highly confined low-loss plasmons in graphene–boron nitride heterostructures. *Nat Mater* **14**, 421-425, (2015).
20. Fei, Z. *et al.* Infrared Nanoscopy of Dirac Plasmons at the Graphene–SiO₂ Interface. *Nano Letters* **11**, 4701-4705, (2011).
21. Wunsch, B., Stauber, T., Sols, F. & Guinea, F. Dynamical polarization of graphene at finite doping. *New Journal of Physics* **8**, 318, (2006).
22. Kumar, A., Low, T., Fung, K. H., Avouris, P. & Fang, N. X. Tunable Light–Matter Interaction and the Role of Hyperbolicity in Graphene–hBN System. *Nano Letters* (2015).
23. Hwang, E. H., Sensarma, R. & Das Sarma, S. Plasmon-phonon coupling in graphene. *Physical Review B* **82**, 195406, (2010).
24. Yan, H. *et al.* Damping pathways of mid-infrared plasmons in graphene nanostructures. *Nat Photon* **7**, 394-399, (2013).
25. Liu, Z., Lee, H., Xiong, Y., Sun, C. & Zhang, X. Far-Field Optical Hyperlens Magnifying Sub-Diffraction-Limited Objects. *Science* **315**, 1686, (2007).
26. Li, P. *et al.* Hyperbolic phonon-polaritons in boron nitride for near-field optical imaging. *arXiv:1502.04093* (2015).
27. Hoffman, A. J. *et al.* Negative refraction in semiconductor metamaterials. *Nat Mater* **6**, 946-950, (2007).
28. Jacob, Z., Alekseyev, L. V. & Narimanov, E. Optical Hyperlens: Far-field imaging beyond the diffraction limit. *Opt. Express* **14**, 8247-8256, (2006).

29. Smith, D. R., Schurig, D., Mock, J. J., Kolinko, P. & Rye, P. Partial focusing of radiation by a slab of indefinite media. *Applied Physics Letters* **84**, 2244-2246, (2004).
30. Vakil, A. & Engheta, N. Transformation Optics Using Graphene. *Science* **332**, 1291-1294, (2011).
31. Kadic, M. *et al.* Transformation plasmonics. *Nanophotonics* **1**, 51, (2012).
32. Iorsh, I. V., Mukhin, I. S., Shadrivov, I. V., Belov, P. A. & Kivshar, Y. S. Hyperbolic metamaterials based on multilayer graphene structures. *Physical Review B* **87**, 075416, (2013).
33. Goos, F. & Hänchen, H. Ein neuer und fundamentaler Versuch zur Totalreflexion. *Annalen der Physik* **436**, 333-346, (1947).
34. Wu, J.-S., Basov, D. N. & Fogler, M. M. Topological insulator are tunable waveguides for hyperbolic polaritons. *Physical Review B* **92**, 205430, (2015).
35. Cai, Y., Zhang, L., Zeng, Q., Cheng, L. & Xu, Y., Infrared reflectance spectrum of BN calculated from first principles. *Solid State Commun.* **141**, 262 (2007).
36. Wunsch, B., Stauber, T., Sols, F. & Guinea, F. Dynamical polarization of graphene at finite doping. *New J. Phys.* **8**, 318 (2006).

Chapter 5

Emitter and emission efficiency of phonon polaritons in hexagonal boron nitride

5.1 Abstract

We investigated emission and propagation of polaritons in a two dimensional van der Waals material hexagonal boron nitride (hBN). Our specific emphasis in this work is on hyperbolic phonon polariton emission that we investigated by means of scattering-type scanning near-field optical microscopy. Real-space nano-images detail how the polaritons are launched in several common arrangements including: light scattering by the edges of the crystal, metallic nanostructures deposited on the surface of hBN crystals, as well as random defects and impurities. Notably, the scanned tip of the near-field microscope is itself an efficient polariton launcher. Our analysis reveals that the scanning tips are superior to other types of emitters we have investigated. Furthermore, the study of polariton

emission and emission efficiency may provide insights for development of polaritonic devices and for fundamental studies of collective modes in other van der Waals materials.

5.2 Introduction

Van der Waals (vdW) materials [1] have emerged as new media for the exploration of polaritons, the coupled collective oscillations of field and polarization charges [2-4]. Recently studied examples include *i*) plasmon-polaritons in conductors such as graphene [5-12], thin films of high- T_c superconductors [13] and surface states of topological insulators (TIs) [14], *ii*) phonon-polaritons in insulators such as hexagonal boron nitride (hBN) [15-22] and bismuth-based TIs [14,23], *iii*) hybrid plasmon-phonon-polariton modes in vdW heterostructures [14,24-27]. The optical permittivity of vdW materials can be extremely anisotropic, having the opposite signs along the in- and out-of-plane axes, the property known as the hyperbolic response [28-31]. Accordingly, collective modes found in these frequency ranges are referred to as the hyperbolic polaritons. Appealing characteristics of polaritons in vdW systems include high optical confinement [5,26,32], low damping [32] as well as exceptional mechanical, optical, and electrical tunability [3,7,8,21,24,25,32,33].

Coupling incident light to polaritons requires overcoming their momentum mismatch [2,3]. This is possible if the system under study lacks translational invariance, for example, if the sample is of small size [15,22], has a periodic patterning [5,9,11], or an intrinsic inhomogeneity. Alternatively, light-polariton conversion can be facilitated by extrinsic structures brought into the sample's proximity, such as metallic stripes or plates.

Such methods have been utilized for emission of plasmon polaritons in graphene [34]. Emission of phonon polaritons by metallic edges have been demonstrated in SiC [35] and more recently in a vdW insulator hBN [16]. Below we report on these and other types of phonon-polariton emitters in hBN and evaluate their relative efficiency. Our analysis offers guidance for the development of nano-optical systems with high-efficiency coupling to polaritonic waves.

5.3 Experimental results

5.3.1 Various polariton emitters

We focus on the mid-infrared (IR) spectral range $\omega = 1370 - 1610 \text{ cm}^{-1}$ where hBN is optically hyperbolic [28-31]. Here $\omega = 1 / \lambda_{\text{IR}}$ and λ_{IR} is the free-space IR wavelength. The polaritons existing in this domain are referred to as the hyperbolic phonon-polaritons (HP²s) [16,19,21,22,25]. Real-space imaging of polaritons has been carried out using the scattering-type scanning near-field optical microscopy (s-SNOM, methods) [7,8,10,16-21,25,32]. As shown schematically in Fig. 5.1(a), under the illumination of an IR laser, the polaritonic standing waves can form and they can be visualized by scanning the sample under the tip of the atomic force microscope (AFM) [7,8,21]. A representative s-SNOM image (Fig. 5.1(b)) displays an oscillating pattern (or fringes) parallel to the crystal edges in a tapered hBN micro-crystal. The line profile (s-SNOM amplitude $s(\omega)$ as a function of the position L along the blue line) associated with these fringes is plotted in Fig. 5.1(c). Close to the hBN edges (white dashed lines), the s-SNOM image exhibits the strongest fringe followed by several other peaks with gradually decreasing amplitude (Fig. 5.1(b)-

(c)). As established in previous studies [17,20,21], propagating HP²s waves are both emitted and detected by the s-SNOM tip acting as an optical antenna [36]. These fringe patterns originate from interferences between the tip-emitted (solid purple arrow) and hBN edge-reflected HP²s (dashed purple arrow). The measured fringe periodicity is equal to one-half of the polariton in-plane wavelength ($\lambda_p/2$) [16,17,20,21] for the principal HP² branch. Interestingly, further away from the hBN edges, the $\lambda_p/2$ fringes become damped yet fringes with a much longer period persist (Fig. 5.1(b)-(c)). These latter fringes show the period of $\sim \lambda_p$ clearly visible in the line profile (Fig. 5.1(c)) and its Fourier transform (FT) (Fig. 5.1(c) inset, bottom).

We attribute the origin of the period- λ_p fringes to polaritons emitted by the edges of hBN crystals marked with white dashed lines in Fig. 5.1(b). The edge emission is illustrated by the annotated numerical simulation shown in the inset of Fig. 5.1(a). The green arrows in this figure represent the monochromatic IR beam, which illuminates both the hBN crystal and the s-SNOM tip. This IR beam carries the momentum $k_{\text{IR}} = 2\pi / \lambda_{\text{IR}}$ arriving at the incidence angle ψ . At the hBN edge, the IR beam excites the HP² wave (cyan arrow) possessing the in-plane momentum of $k_p = 2\pi / \lambda_p$. This edge-launched wave propagates away from the edge and interferes with the incident IR beam (green arrows) forming a standing wave parallel to the edge. The measured s-SNOM signal is in the first approximation proportional to the local electric field underneath the tip apex [35]. This signal is produced by the field of the IR beam E_i and that of the edge-emitted polaritons E_p : $E_{\text{tip}} = E_i \cos \psi + E_p$. The period of the corresponding interference fringes is [35] $\delta = 2\pi / (k_p - k_{\text{IR}} \cos \psi)$. In the case of highly-confined HP²s in hBN [21,22], k_p is much larger than

k_{IR} , and so δ is close to $2\pi / k_p = \lambda_p$, in accord with our data (Figs. 5.1(b)-(c)) and numerical simulations (Fig. 5.1(a), inset). Clearly, when both edge-emitted and tip-emitted polaritons are present, the s-SNOM image may be rather complex. The observed pattern in Fig. 5.1(b) and 5.1(c) is the case in point.

The different amplitudes of the λ_p and $\lambda_p/2$ polariton fringes seen in Figs. 5.1(b) and 5.1(d) (especially in the interior of hBN) are due to their distinct propagation trajectories and travel distances (Fig. 5.1(a)). Indeed, edge-emitted polaritons (fringe periodicity λ_p) propagate as plane waves, whereas tip-emitted polaritons ($\lambda_p/2$) propagate as circular ones. The amplitude of a circular wave decreases with the travel distance even in the absence of damping, whereas that of the plane wave does not. Furthermore, the path lengths of polaritons forming these λ_p and $\lambda_p/2$ fringes are different. The edge-emitted polaritons (λ_p) only need to traverse the tip-edge distance L once to become registered in our apparatus. The tip-emitted/edge-reflected polaritons (period $\lambda_p/2$) have to do a round trip. Therefore, the combination of geometric spreading and two-fold travel distance account for the faster decrease of period- $\lambda_p/2$ oscillations in Figs. 5.1(b)-(c). In the interior of the hBN crystal (Fig. 5.1(b)), λ_p -periodic fringes emitted by the α edge (blue solid line in Fig. 1c) and β edge (red dashed line in Fig. 5.1(c)) exhibit different intensities. This difference is related to the shadowing of the sample by the AFM cantilever in our experiment. Once the hBN crystal is rotated by $\pi/2$, we observed identical λ_p fringe intensity (Fig. 5.1(d)) from α and β edges, see Supplementary Information for details.

In addition to the hBN crystal edge and s-SNOM tip, polaritons in hBN are also emitted by metallic nanostructures. The images in Figs. 5.2(a) and 5.2(c) have been

obtained from an hBN crystal with Au disks of height 188 nm and diameters 1-2 μm fabricated on its top surface. The s-SNOM data in Fig. 5.2(a) exhibit two groups of interference fringes. The fringes in the first group are parallel to the edge; those of the other group are concentric to the Au disk. To estimate the corresponding polariton wavelengths we examine the representative line traces (green and blue curves in Fig. 5.2(b)) extracted from the s-SNOM image in Fig. 5.2(a) by taking linear cuts along the lines of the same color. The green curve extracted from a line scan taken perpendicular to the hBN edge (Fig. 5.2(a)) again reveals a superposition of fringes with $\lambda_p/2$ and λ_p periodicities. One can separate these components via the FT analysis [19]. In addition to the tip-emitted ($\lambda_p/2$) and edge-emitted (λ_p) polariton fringes (Fig. 5.2(a)) parallel to the hBN edges, one can witness concentric circular fringes around the Au disks (Fig. 5.2(a) and 5.2(c)). The profile for the concentric fringes arising from the gold emitter (blue curve, Fig. 5.2(b)) exhibits oscillations with nearly the same period as the edge emitted ones (black curve). Thus, it is attributed to polaritons emitted by the disk edges (magenta dashed circles, Fig. 5.2(a)). To verify this assertion, we numerically simulated the s-SNOM image following an earlier study [35] (Fig. 5.3(d)); these simulations account for our experimental results.

5.3.2 Relative polariton emission efficiency

Let us discuss the efficiency – the ability to convert incident IR photons into propagating polaritons – of different polariton emitters. We can quantify this parameter by taking the ratio of either the power P_p or the intensity I_p of the polariton wave to the incident IR power P_0 per unit area. The intensity scales as a square $I_p = |S|^2/M$ of the

amplitude S measured by s-SNOM. The proportionality coefficient M is unknown but constant for a data set obtained for the same experimental conditions (IR frequency, illumination intensity, same tip, etc.). The ratio $l = I_p/P_0$, which has the units of length, defines the scattering length. This parameter is appropriate for an extended line-like emitter, such as an hBN edge. However, it is not suitable for a small, point-like emitter. As discussed above, such a point emitter generates waves whose intensity would decrease with distance r (measured from its center) even in the absence of damping. In the latter case, it is the total power $P_p = 2\pi r I_p(r)$ of the wave that remains constant. The proper measure of efficiency is therefore the ratio $A = P_p/P_0$, the scattering cross-section, which has the units of area. The formula for the s-SNOM amplitude, which applies to both types of emitters and includes the phase of the wave and also unavoidable damping can be written as

$$S(r) = \sqrt{P_0 M} G(r) e^{i(q_p r + \phi)}, \quad (5.1)$$

where q_p and ϕ are the complex momentum and a phase shift, respectively. The “geometric” factor is $G(r) = \sqrt{l}$ for a line-like emitter and $G(r) = \sqrt{A/2\pi r}$ for a point-like one. Note that a metallic disk of radius $r_{disk} \gg \lambda_p$ is a type of emitter that can be considered a line-like near its edge, at $r - r_{disk} \ll r_{disk}$, and a point-like at $r \gg r_{disk}$. Accordingly, having determined its cross-section, one can also calculate the scattering length of the disk edge via $l_{disk} = A/2\pi r_{disk}$. For polaritons launched by the tip located a distance x from the edge, one should substitute $2x$, the separation between the tip and its image [7,8,21] upon reflection, for r in Eq. (5.1).

We have determined A and l by fitting the s-SNOM traces in Fig. 5.2(b) to Eq. (5.1). The fits are shown by the black dashed curves. Note that all of them have the same polariton damping factor $\gamma = \text{Im } q_p / \text{Re } q_p = 0.055$ as in our previous studies [19,21]. For the sake of comparing *relative* efficiency, we choose μm to be the unit of length, omit the common factor $\sqrt{P_0 M}$ in Eq. (5.1), and normalize $S(r)$ in suitable arbitrary units. From this defined fitting procedure, we have obtained $A = 61$ for the s-SNOM tip, $l = 0.56$ for the hBN edge, $A = 14$ and $l = 1.4$ for the $1.5\mu\text{m}$ -radius Au disk (Table 5.1). We conclude that in terms of the polariton emission efficiency, the tip is superior to the disk treated as a point-like emitter; while as a line-like emitter disk is more efficient than the edge. We attribute the higher emission efficiency of the metallic objects (the tip and the disk) to their ability to concentrate electric field [36]. The hBN edge lacks this ability, which explains its comparatively low photon to polariton conversion efficiency. The higher emission efficiency of the tip compared to the disk indicates the former has a stronger coupling to high- q_p polaritons [7,8,15-17,21]. Note that one possible way to calibrate the scattering parameters A and l in absolute units is by comparison to some standard emitters for which reliable theoretical calculations are possible. The hBN edge could be a candidate for such a standard emitter provided a better understanding of the field singularities at the sharp corners is developed, see Fig. 5.1(a) (inset) and Methods. This can be a subject of future work.

Impurities and defects on the sample surface (introduced unintentionally during sample fabrication, methods) can play the role of polariton emitters as well. As shown in Fig. 5.3(a), surface impurities (marked with magenta asterisks) act as point-like emitters

that emit circular polariton waves, whereas a surface protrusion (green arrow) act as a line-like emitter. The latter one emit plane waves that do not spread much as they travel. As a result, the amplitude of these waves decays slowly and remains discernible in almost the entire field of view in Fig. 5.3.

5.4 Conclusion and Outlook

In summary, the imaging data compiled in Figs. 5.1-5.3 demonstrate a variety of polariton emitters in hBN of different emission efficiency. Although essentially any topographic feature can act as an emitter, their efficiency is inferior to that of a large metalized tip. Note that the emitters studied in this work may also be employed for scattering polaritons into optical photons detectable by conventional means. The methodology presented in this work may be readily extended to collective modes [2-4] in other vdW materials including graphene [34], transition metal dichalcogenides, black phosphorus, and topological insulators. Our results along with the recent work on grating polaritonic couplers [37] present the initial steps towards developing high-efficiency polariton emitters and detectors for diverse nanophotonics applications.

5.5 Methods

5.5.1 Experimental setup

The nano-imaging experiments described in the main text were performed at UCSD using a commercial s-SNOM (www.neaspec.com). The s-SNOM is based on a tapping-

mode AFM illuminated by monochromatic Quantum Cascade Lasers (QCLs) (www.daylightsolutions.com). These lasers cover a frequency range of 900 – 2300 cm^{-1} in the mid-IR. The nanoscale near-field images were registered by a pseudo-heterodyne interferometric detection module with a AFM tapping frequency and amplitude around 280 kHz and 70 nm respectively. In order to obtain the background-free images, the s-SNOM output signal used in this work is the scattering amplitude $s(\omega)$ demodulated at the 3rd harmonics of the tapping frequency.

5.5.2 Sample fabrication

Our hBN crystals were exfoliated from bulk samples synthesized with high-pressure techniques and then transferred onto Si wafers with a 300-nm-thick SiO_2 layer. The Au patterns were fabricated on the hBN crystals by electron beam lithography.

5.5.3 Simulation of edge-emitted hyperbolic phonon polariton fringes

The numerical simulations shown in Fig. 5.1(a) (inset) were done within the quasi-static approximation. In this approach the amplitude of the scalar potential $\Phi(x, z)$ in the system is assumed to satisfy the anisotropic Laplace equation: $\partial_x(\epsilon^x \partial_x \Phi) + \partial_z(\epsilon^z \partial_z \Phi) = 0$, where the principal values (ϵ^x, ϵ^z) of the permittivity tensor are functions of frequency ω . To produce the graphic shown in the inset of Fig. 5.1(a) we used the following parameters: (1, 1) for vacuum; $(-0.5620 + 0.0678i, 2.7782 + 0.0006i)$ for hBN, and $(1.4646 + 0.0104i, 1.4646 + 0.0104i)$ for SiO_2 substrate, which are representative of frequency $\omega = 1587 \text{ cm}^{-1}$.

The 300-nm tall and 2050-nm wide simulation domain surrounded a 100-nm thick hBN slab. At the outer boundary of the domain the $\Phi = -x$ was imposed to model a uniform unit external field in the x -direction. This boundary-value problem was solved using MATLAB PDE Toolbox (MATLAB, Inc., Natick, MA; Release 2012b). Shown in Fig. 1a (inset) are the results for the absolute value of the electric field $|E| = [(\partial_x \Phi)^2 + (\partial_z \Phi)^2]^{1/2}$. As one can see, near the corners of the hBN slab, the calculated field distribution exhibits a structure of internal criss-crossing rays, which produce “hot lines” on the surface of the slab. Further away from the edge, the calculated field distribution morphs into a gradually decaying sinusoidal wave. The internal polariton rays and the “hot lines” they produce have the same interpretation as the “hot rings” predicted in simulations and subsequently observed on sidewalls of hBN nanocones [15] and on the top surfaces of hBN slabs deposited on metallic disks [19]. Such high-intensity lines are the beats produced by coherent superpositions of multiple guided waves. As detailed in our previous work [15,19,21], the guided waves of a slab are discrete eigenmodes characterized by the in-plane momenta $k_l = (\pi l + \chi) \tan \theta / d$, where $l = 0, 1, 2, \dots$ is the mode number, $\chi \sim 1$ is the boundary condition dependent phase shift, and d is the slab thickness. Accordingly, the beats pattern has the periodicity $2d \tan \theta \sim \lambda_p / 4$ while the parameter $\tan \theta = i \sqrt{\epsilon^z} / \sqrt{\epsilon^x}$ has the meaning of the slope of the polariton rays with respect to the z -axis. Unfortunately, the region where the beats exist is very narrow and we could not probe it with our experimental resolution. On the other hand, the sinusoidal standing waves we have imaged can be identified with the principal $l = 0$ guided waves of wavelength $\lambda_p \equiv 2\pi / k_0$.

5.6 Supplementary Information

5.6.1 Orientation-dependent nano-imaging data

The behavior of λ_p -periodic fringes (Fig. 5.1(b)) near two different edges (α and β) of the tapered hBN crystal supports their attribution to polaritons emitted from the hBN edges. Indeed, these two facets of the hBN crystal are subject to different illumination conditions. As shown in Fig. 5.1(a), IR illumination of the β edge is partially blocked by the atomic force microscope (AFM) cantilever (Fig. 5.1(a)), whereas the α edge is unobscured. These unequal conditions result in different amplitudes for the edge-emitted polaritons, apparent from the scattering-type scanning near-field optical microscopy (s-SNOM) image (Fig. 5.1(b)) and the corresponding line profiles (Fig. 5.1(c)). In the interior of hBN (Fig. 5.1(b)), polaritons emitted by the α edge (blue solid line) are prominent while those from the β edge (red dashed line) are much weaker (see also the line traces in the inset of Fig. 5.1(c), top). We have repeated this experiment with the hBN crystal rotated laterally by $\pi/2$, in which case the two edges experience similar IR illumination conditions (Fig. 5.1(d), IR beam and s-SNOM tip are the same as Figs. 5.1(a)-(b)). In this latter geometry (Fig. 5.1(d)), the λ_p fringes emitted by α and β edges exhibit nearly equal amplitude in the interior of hBN. The s-SNOM imaging data obtained from an hBN disk (Fig. 5.4) provides further evidence for the impact of AFM cantilever shadowing on polariton amplitudes. The λ_p -periodic fringes propagating from the top-right part of the disk appear weaker compared with those elsewhere due to the lower incident field in the AFM cantilever shadow.

5.6.2 Polariton fringe periods in hBN and in graphene

It is instructive to compare the phenomenology of the hyperbolic phonon polariton (HP²) guided waves we have observed in hBN with that of surface plasmon polaritons (SP²s) waves in graphene. The first generation of s-SNOM experiments were carried out with modest-quality graphene [7,8]. The imaging data obtained by these experiments were consistent with the notion of the tip-launched $\lambda_p/2$ -period fringes, with λ_p being the SP² wavelength. More recent studies of high-quality encapsulated graphene [32,38] have revealed fringes with the double-peak structure, implying a coexistence of $\lambda_p/2$ -periodic oscillations with λ_p -period ones. Unlike the λ_p -period polariton fringes observed for hBN, those observed in graphene exhibit virtually no dependence on the in-plane polarization of the incident field [32,38]. This latter finding indicates that the direct conversion of light into SP² at the graphene edge is not very important. In Ref. [38], Supplementary material, it was suggested that these longer-period fringes arise instead due to the long-range Coulomb interaction between the tip and the excess charge density induced near the edge by the tip-launched plasmon wave. Let us briefly review this argument, which was recently rediscovered in Ref. [39]. Let x be the coordinate along the normal to the edge passing through the tip (such as the blue line in Fig. 5.1(b)) with the origin at the edge at $x = 0$. Far enough from the edge (s-SNOM tip position: $x = L$) the reflected wave can be described by this method of images, as a point source at $x = -L$ sending out a circular wave:

$$s(x) \propto \frac{1}{\sqrt{x+L}} e^{ik_p(x+L)+i\varphi}. \quad (5.2)$$

Here $\varphi \sim 1$ is the reflection phase shift which depends on the boundary conditions. At the tip position $x=L$, the phase of the reflected wave contains the term $2k_p L$, and so the superposition of the tip-launched (purple solid arrow) and edge-reflected (purple dashed arrow) waves yields the interference fringes of period $\lambda_p/2$. Whereas Eq. (5.3) describes the propagating part of the reflected wave, there should also be an evanescent part with the large- x asymptotic behavior [38]

$$s(x) \propto \frac{1}{x^a} e^{ik_p L}, \quad (5.3)$$

where $a > 0$ is some exponent [38]. Qualitatively, one can think of the evanescent wave as composed of non-resonant polariton modes of momenta $k \sim 1/x \ll k_p$. Note that the phase advance of $k_p L$ is present in both Eqs. (5.2) and (5.3) because the incident wave has to travel the distance L from the tip before it reaches the edge. However, there is no additional phase accumulation for the “return trip” as the evanescent wave does not oscillate. Hence, the resultant fringes have the period of λ_p , just like the polaritons directly scattered by the edge in the absence of any tip. In principle, this alternative mechanism should apply to any polariton wave governed by Coulomb interaction, including the HP²s in hBN.

One way to discriminate between the two mechanisms of λ_p -fringes is to check the dependence of the fringe amplitude on the incident IR beam polarization. The long-range edge-tip interaction should be insensitive to in-plane component of the polarization whereas the edge-launched wave should vanish if this component is parallel to the edge. As we discussed in Section 1, in our experiment the beam-sample orientation dependence of fringes is significant. This suggests that in our hBN samples, unlike in graphene, edge-

emission mechanism dominates over the long-range edge-tip interaction one. The reason for this different behavior warrants further investigation.

5.7 Acknowledgements

This work is supported by ONR, AFOSR and Moore foundation.

Chapter 5, in full, is a reprint of the material as it appears in S. Dai, Q. Ma, Y. Yang, J. Rosenfeld, M. D. Goldflam, A. McLeod, Z. Sun, T. I. Andersen, Z. Fei, M. K. Liu, Y. Shao, K. Watanabe, T. Taniguchi, M. Thiemens, F. Keilmann, P. Jarillo-Herrero, M. M. Fogler & D. N. Basov. “Relative efficiency of polariton emission in two-dimensional materials”. *arXiv*. 1704.05618. The dissertation author was the primary investigator and author of this paper.

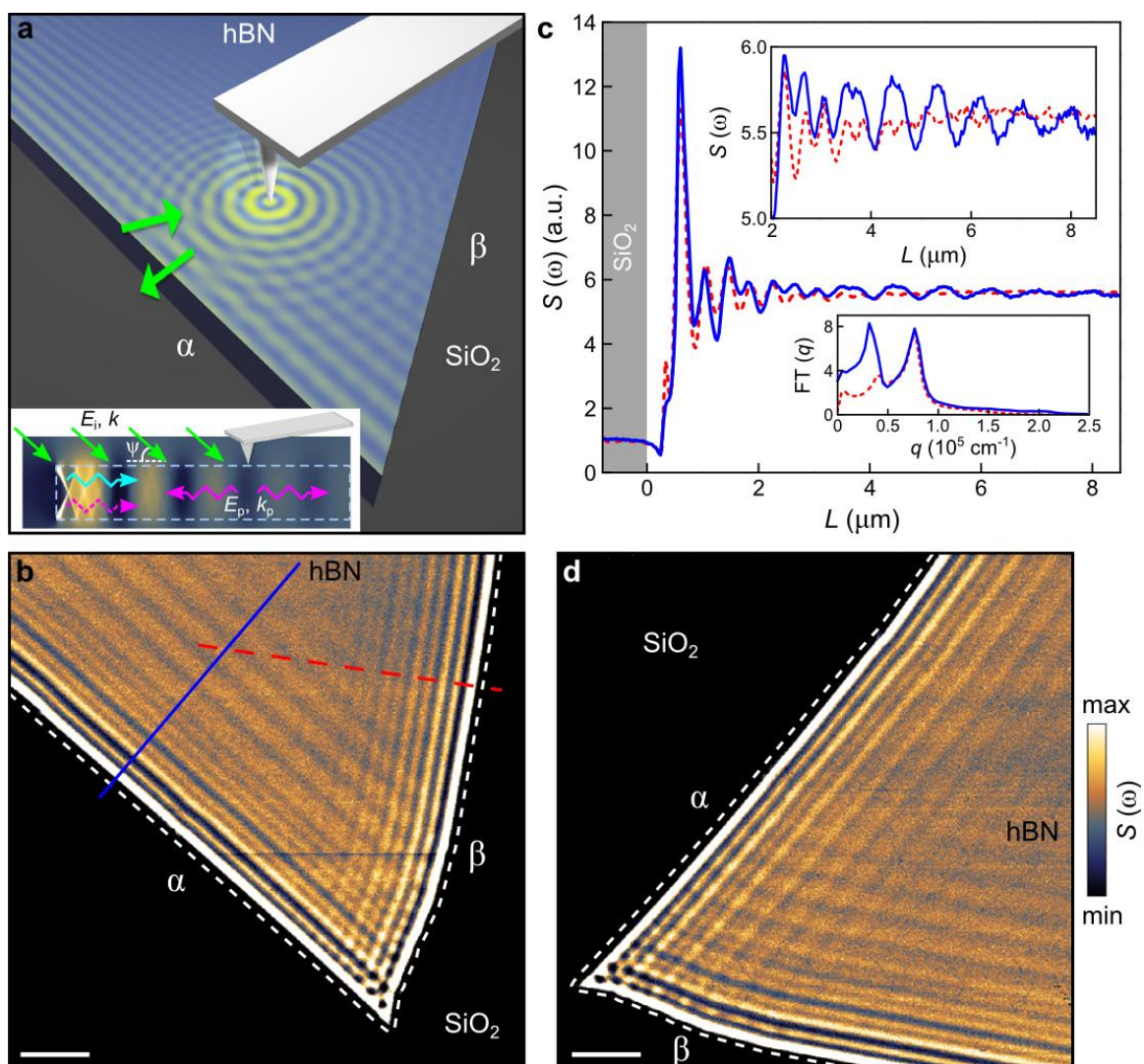


Figure 5.1: Polaritons emitted by the s-SNOM tip and hBN edges. (a), The experimental schematic. The s-SNOM tip and a tapered hBN crystal are illuminated by the weakly focused IR beam from a Quantum Cascade Laser (QCL). We collect the back-scattered near-field signal (green arrow). Inset, the cross-section of the tip-emitted (magenta arrows) and edge-emitted (cyan arrow) polaritons registered by the tip. Color map, the simulation of the edge-emitted polariton fringes (see Methods). (b), The near-field amplitude image of the hBN crystal in (a). (c), Polariton line profiles taken perpendicular to the α edge (blue solid line) and β edge (red dashed line) in (b). Inset: top, detailed view of the line profiles when $L > 2\mu\text{m}$. Bottom, the Fourier Transform spectra of the line profiles. (d), Near-field amplitude image of the same hBN crystal after a clockwise rotation of $\pi/2$ from (b). White dashed lines track the hBN edges. The hBN thickness: 117 nm. IR frequency: $\omega = 1530\text{cm}^{-1}$. Scale bar: $2\mu\text{m}$.

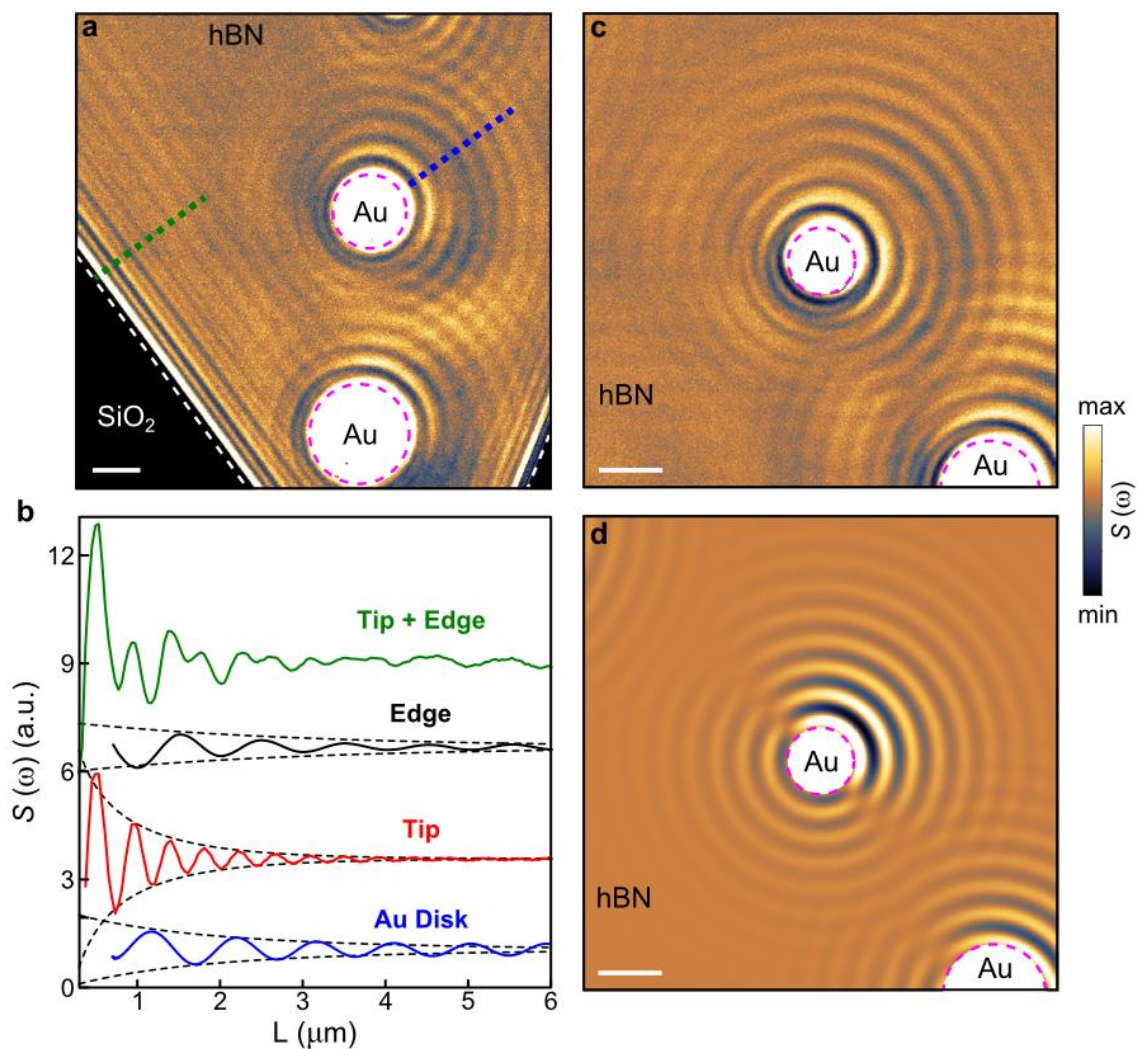


Figure 5.2: Polariton emission efficiency. (a), Near-field amplitude image of the hBN crystal with artificially fabricated Au disks on top. (b), Profiles of polariton fringes as a function of the distance L from the edge of an emitter. The green and blue curves are extracted by averaging a series of linear cuts near the dotted lines in (a). The black and red curves are obtained by the FT analysis of the green curve. The dashed curves are the fits to Eq. (5.1). (c), Near-field amplitude image of Au disks in the interior of the hBN crystal. (d), The simulation of s-SNOM image in (c). White and magenta dashed lines track the edges of the hBN and Au disks. The hBN thickness: 117 nm. IR frequency: $\omega = 1530\text{cm}^{-1}$. Scale bar: $2\mu\text{m}$.

Table 5.1: Relative scattering cross-sections and/or scattering lengths for three types of emitters studied.

Scattering parameter	s-SNOM tip	hBN edge	Au disk $r_{\text{disk}} = 1.5\mu\text{m}$
l		0.56	1.4
A	61		14

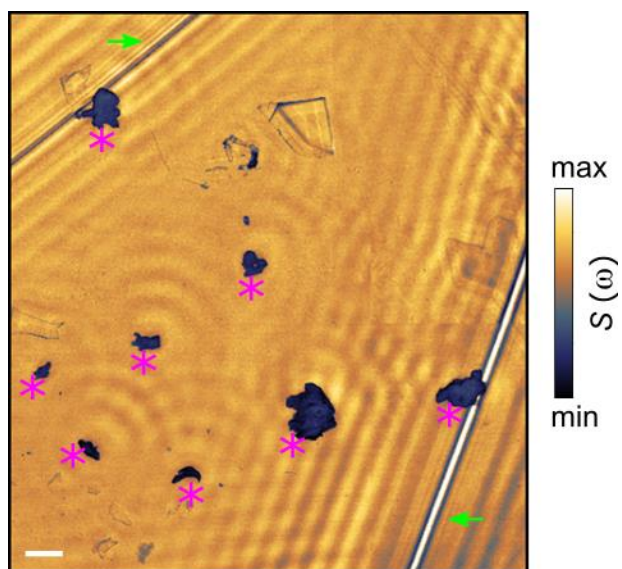


Figure 5.3: Near-field amplitude image of the hBN crystal with impurities (marked with magenta asterisks) and protrusion (green arrow) defect on the surface. The hBN thickness: 253 nm. IR frequency: $\omega = 1550\text{cm}^{-1}$. Scale bar: $2\mu\text{m}$.

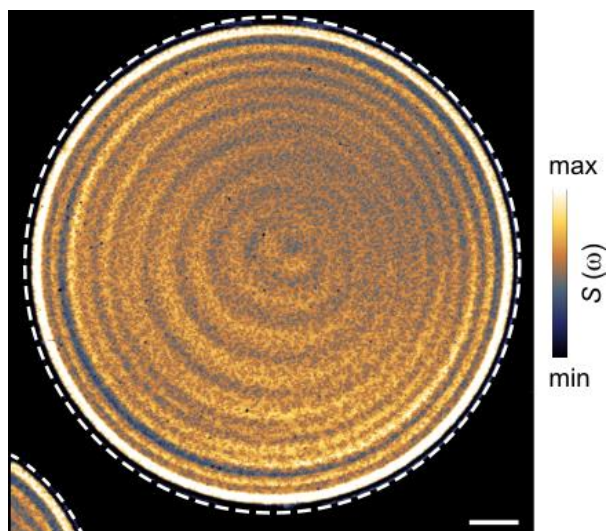


Figure 5.4: Polaritons in hBN disks. Near-field amplitude image of the artificially etched hBN disk. The white dashed line tracks the edge of the hBN crystal. The hBN thickness: 151 nm. Infrared frequency: $\omega = 1519 \text{ cm}^{-1}$. Scale bar: 2 μm .

5.8 Bibliography

1. Geim, A. K.; Grigorieva, I. V. *Nature* **2013**, 499, (7459), 419-425.
2. Low, T.; Chaves, A.; Caldwell, J. D.; Kumar, A.; Fang, N. X.; Avouris, P.; Heinz, T. F.; Guinea, F.; Martin-Moreno, L.; Koppens, F. *Nat Mater* **2017**, 16, (2), 182-194.
3. Basov, D. N.; Fogler, M. M.; García de Abajo, F. J. *Science* **2016**, 354, (6309).
4. Xia, F.; Wang, H.; Xiao, D.; Dubey, M.; Ramasubramaniam, A. *Nat Photon* **2014**, 8, (12), 899-907.
5. Yan, H.; Low, T.; Zhu, W.; Wu, Y.; Freitag, M.; Li, X.; Guinea, F.; Avouris, P.; Xia, F. *Nat Photon* **2013**, 7, (5), 394-399.
6. Fang, Z.; Thongrattanasiri, S.; Schlather, A.; Liu, Z.; Ma, L.; Wang, Y.; Ajayan, P. M.; Nordlander, P.; Halas, N. J.; García de Abajo, F. J. *ACS Nano* **2013**, 7, (3), 2388-2395.
7. Fei, Z.; Rodin, A. S.; Andreev, G. O.; Bao, W.; McLeod, A. S.; Wagner, M.; Zhang, L. M.; Zhao, Z.; Thiemens, M.; Dominguez, G.; Fogler, M. M.; Neto, A. H. C.; Lau, C. N.; Keilmann, F.; Basov, D. N. *Nature* **2012**, 487, (7405), 82-85.
8. Chen, J.; Badioli, M.; Alonso-Gonzalez, P.; Thongrattanasiri, S.; Huth, F.; Osmond, J.; Spasenovic, M.; Centeno, A.; Pesquera, A.; Godignon, P.; Zurutuza Elorza, A.; Camara, N.; de Abajo, F. J. G.; Hillenbrand, R.; Koppens, F. H. L. *Nature* **2012**, 487, (7405), 77-81.
9. Ju, L.; Geng, B.; Horng, J.; Girit, C.; Martin, M.; Hao, Z.; Bechtel, H. A.; Liang, X.; Zettl, A.; Shen, Y. R.; Wang, F. *Nat Nano* **2011**, 6, (10), 630-634.
10. Gerber, J. A.; Berweger, S.; O'Callahan, B. T.; Raschke, M. B. *Physical Review Letters* **2014**, 113, (5), 055502.
11. Brar, V. W.; Jang, M. S.; Sherrott, M.; Lopez, J. J.; Atwater, H. A. *Nano Letters* **2013**, 13, (6), 2541-2547.
12. Yang, X.; Zhai, F.; Hu, H.; Hu, D.; Liu, R.; Zhang, S.; Sun, M.; Sun, Z.; Chen, J.; Dai, Q. *Advanced Materials* **2016**, 28, (15), 2931-2938.
13. Stinson, H. T.; Wu, J. S.; Jiang, B. Y.; Fei, Z.; Rodin, A. S.; Chapler, B. C.; McLeod, A. S.; Castro Neto, A.; Lee, Y. S.; Fogler, M. M.; Basov, D. N. *Physical Review B* **2014**, 90, (1), 014502.

14. Wu, J.-S.; Basov, D. N.; Fogler, M. M. *Physical Review B* **2015**, 92, (20), 205430.
15. Giles, A. J.; Dai, S.; Glembocki, O. J.; Kretinin, A. V.; Sun, Z.; Ellis, C. T.; Tischler, J. G.; Taniguchi, T.; Watanabe, K.; Fogler, M. M.; Novoselov, K. S.; Basov, D. N.; Caldwell, J. D. *Nano Letters* **2016**, 16, (6), 3858-3865.
16. Yoxall, E.; Schnell, M.; Nikitin, A. Y.; Txoperena, O.; Woessner, A.; Lundeberg, M. B.; Casanova, F.; Hueso, L. E.; Koppens, F. H. L.; Hillenbrand, R. *Nat Photon* **2015**, 9, (10), 674-678.
17. Shi, Z.; Bechtel, H. A.; Berweger, S.; Sun, Y.; Zeng, B.; Jin, C.; Chang, H.; Martin, M. C.; Raschke, M. B.; Wang, F. *ACS Photonics* **2015**, 2, (7), 790-796.
18. Li, P.; Lewin, M.; Kretinin, A. V.; Caldwell, J. D.; Novoselov, K. S.; Taniguchi, T.; Watanabe, K.; Gaussmann, F.; Taubner, T. *Nat Commun* **2015**, 6.
19. Dai, S.; Ma, Q.; Andersen, T.; McLeod, A. S.; Fei, Z.; Liu, M. K.; Wagner, M.; Watanabe, K.; Taniguchi, T.; Thiemens, M.; Keilmann, F.; Jarillo-Herrero, P.; Fogler, M. M.; Basov, D. N. *Nat Commun* **2015**, 6.
20. Xu, X. G.; Ghamsari, B. G.; Jiang, J.-H.; Gilburd, L.; Andreev, G. O.; Zhi, C.; Bando, Y.; Golberg, D.; Berini, P.; Walker, G. C. *Nat Commun* **2014**, 5.
21. Dai, S.; Fei, Z.; Ma, Q.; Rodin, A. S.; Wagner, M.; McLeod, A. S.; Liu, M. K.; Gannett, W.; Regan, W.; Watanabe, K.; Taniguchi, T.; Thiemens, M.; Dominguez, G.; Neto, A. H. C.; Zettl, A.; Keilmann, F.; Jarillo-Herrero, P.; Fogler, M. M.; Basov, D. N. *Science* **2014**, 343, (6175), 1125-1129.
22. Caldwell, J. D.; Kretinin, A. V.; Chen, Y.; Giannini, V.; Fogler, M. M.; Francescato, Y.; Ellis, C. T.; Tischler, J. G.; Woods, C. R.; Giles, A. J.; Hong, M.; Watanabe, K.; Taniguchi, T.; Maier, S. A.; Novoselov, K. S. *Nat Commun* **2014**, 5.
23. Talebi, N.; Ozsoy-Keskinbora, C.; Benia, H. M.; Kern, K.; Koch, C. T.; van Aken, P. A. *ACS Nano* **2016**, 10, (7), 6988-6994.
24. Kumar, A.; Low, T.; Fung, K. H.; Avouris, P.; Fang, N. X. *Nano Letters* **2015**.
25. Dai, S.; MaQ; Liu, M. K.; AndersenT; FeiZ; Goldflam, M. D.; WagnerM; WatanabeK; TaniguchiT; ThiemensM; KeilmannF; Janssen, G. C. A. M.; Zhu, S. E.; Jarillo Herrero, P.; Fogler, M. M.; Basov, D. N. *Nat Nano* **2015**, 10, (8), 682-686.
26. Brar, V. W.; Jang, M. S.; Sherrott, M.; Kim, S.; Lopez, J. J.; Kim, L. B.; Choi, M.; Atwater, H. *Nano Letters* **2014**, 14, (7), 3876-3880.

27. Huber, M. A.; Mooshammer, F.; Plankl, M.; Viti, L.; Sandner, F.; Kastner, L. Z.; Frank, T.; Fabian, J.; Vitiello, M. S.; Cocker, T. L.; Huber, R. *Nat Nano* **2017**, 12, (3), 207-211.
28. Gomez-Diaz, J. S.; Alù, A. *ACS Photonics* **2016**, 3, (12), 2211-2224.
29. Poddubny, A.; Iorsh, I.; Belov, P.; Kivshar, Y. *Nat Photon* **2013**, 7, (12), 948-957.
30. Liu, Z.; Lee, H.; Xiong, Y.; Sun, C.; Zhang, X. *Science* **2007**, 315, (5819), 1686.
31. Jacob, Z.; Alekseyev, L. V.; Narimanov, E. *Optics Express* **2006**, 14, (18), 8247-8256.
32. Woessner, A.; Lundeberg, M. B.; Gao, Y.; Principi, A.; Alonso-González, P.; Carrega, M.; Watanabe, K.; Taniguchi, T.; Vignale, G.; Polini, M.; Hone, J.; Hillenbrand, R.; Koppens, F. H. L. *Nat Mater* **2015**, 14, (4), 421-425.
33. Brar, V. W.; Sherrott, M. C.; Jang, M. S.; Kim, S.; Kim, L.; Choi, M.; Sweatlock, L. A.; Atwater, H. A. *Nat Commun* **2015**, 6.
34. Alonso-González, P.; Nikitin, A. Y.; Golmar, F.; Centeno, A.; Pesquera, A.; Vélez, S.; Chen, J.; Navickaite, G.; Koppens, F.; Zurutuza, A.; Casanova, F.; Hueso, L. E.; Hillenbrand, R. *Science* **2014**, 344, (6190), 1369-1373.
35. Huber, A.; Ocelic, N.; Kazantsev, D.; Hillenbrand, R. *Applied Physics Letters* **2005**, 87, (8), 081103.
36. Atkin, J. M.; Berweger, S.; Jones, A. C.; Raschke, M. B. *Advances in Physics* **2012**, 61, (6), 745-842.
37. Kim, S.; Jang, M. S.; Brar, V. W.; Tolstova, Y.; Mauser, K. W.; Atwater, H. A. *Nature Communications* **2016**, 7, 12323.
38. Ni, G.X. et al. Ultrafast optical switching of infrared plasmon polaritons in high-mobility graphene. *Nature Photon* **10**, 244 (2016).
39. J.-H. Kang, S. Wang, Z. Shi, W. Zhao, E. Yablonovitch, and F. Wang, *Nano Lett* **17**, 1768 (2017).